materials and leads
materials. In cases
ked planes, there is
ng along relatively
7.2.4 [20–22]. It is
rming vicinal inter-
o solid–vapor inter-

icoherent and inco-
ystals that differ in
ter. Consider only
nes and assume that
exercise by first as-
rcise letting one or
vhere copper atoms
cupy the faces.

13

STRUCTURE AND ENERGY OF HOMOPHASE INTERFACES

In our discussion of homophase interfaces, we first examine the structure and properties of grain boundaries, which are the most common planar (two-dimensional) defects in materials. We then look at special planar boundaries, such as twin interfaces and stacking faults.

13.1. GRAIN BOUNDARY ENERGY

As in the previous parts, we begin our discussion of grain boundaries by first examining some typical values of the grain boundary energy. Average grain boundary energies can be determined by annealing metal or alloy wires at high temperature in vacuum and measuring the dihedral angle that forms where a grain boundary intersects the surface, as illustrated in Figure 13.1. This method is called the thermal-grooving technique [24], and the dihedral angle can be measured by optical interferometry or by scanning electron microscopy (SEM). In a manner similar to the contact angle in Figure 7.1, the balance of the interfacial energies at the triple point in Figure 13.1 yields the equation

$$\gamma_{gb} = 2\gamma^{SV} \cos(\theta^{SV}/2), \qquad (13.1)$$

where γ_{gb} is the grain boundary energy, γ^{SV} is the surface energy for the solid–vapor case and θ^{SV} is the dihedral angle defining the groove. Measurement of θ^{SV} allows the ratio of γ_{gb}/γ^{SV} to be determined, and, if γ^{SV} is known, then the magnitude of γ_{gb} can also be found.

Table 13.1 lists the interfacial energy ratio γ_{gb}/γ^{SV} for several f.c.c. metals. It can be seen that the ratio γ_{gb}/γ^{SV} varies from approximately 0.25–0.35 for the f.c.c. metals. A more extensive review by Murr [24] shows that this is typical for many metals and alloys. We used these ratios and the data for the surface energies of the

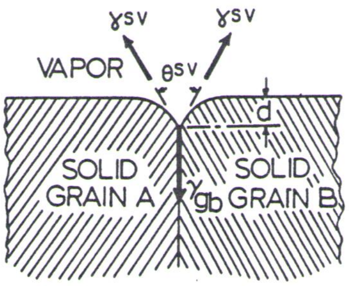

Figure 13.1. Thermal groove profile for grain boundary–surface equilibrium involving evaporation–condensation. The groove depth is *d*. From [24].

corresponding solid–vapor interfaces to calculate the grain boundary energies according to Eq. (13.1); these are also shown in Table 13.1. If we examine the trend among silver, gold and copper, the three f.c.c. metals that we often used in Part II, we see that silver and gold have very similar grain boundary energies, whereas the grain boundary energy of copper is significantly higher. This is not too different from our ranking of the solid surface energies, although the value for gold is a little low. However, if the grain boundaries were truly average and there were no surface contamination effects, the grain boundary energies should scale with the solid surface energies shown in Table 3.3, provided the grooves formed by the same thermal grooving mechanism. The fact that they do not indicates that such data should be interpreted with caution. We see in subsequent sections that grain boundary energies are highly dependent on orientation.

The temperature coefficients of the grain boundary energy have been measured for only a small number of metals and alloys, and these are also shown for the f.c.c. metals in Table 13.1. Examples of the grain boundary energy versus temperature for nickel and stainless steel are shown in Figure 13.2. The temperature coefficients for grain boundaries are negative and appear proportionally smaller than those for solid surface energies, as given in Eq. (3.15).

Table 13.1. Average grain boundary energies for various f.c.c. metals

Metal	γ_{gb}/γ^{SV} (mJ/m^2)	Temperature (°C)	γ_{gb} (mJ/m^2)	$d\gamma_{gb}/dT$ (mJ/m^2·°C)
Al	0.23	450	324	−0.12
Cu	0.34	950	625	−0.10
Ni	0.38	1060	866	−0.20
Ag	0.25	950	375	−0.10
Au	0.27	1000	378	−0.10
Pt	0.29	1300	660	−0.18

Source: From [24].

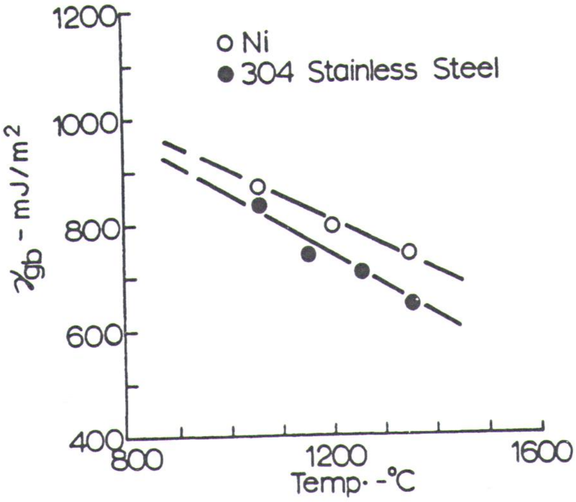

Figure 13.2. Variation of grain boundary energy γ_{gb} for nickel and stainless steel with temperature below the melting point. From [24].

13.2. GRAIN BOUNDARY STRUCTURE

A number of different analytical models have been proposed to describe the structure and properties of grain boundaries. The models vary both in their approach and degree of sophistication. Several of the more important ones are discussed in the following sections. The discussion progresses in approximate order of historical development, beginning with the early interpretation of low-angle grain boundaries in terms of dislocation networks by Read and Shockley [25,26] and closing with recent comprehensive atomistic simulations by Wolf and Merkle [2,7]. Most of the analytical treatments that have been developed for grain (homophase) boundaries can be similarly applied to interphase (heterophase) interfaces. To emphasize the generality of the methods and to avoid duplication in Chapter 14 on heterophase interfaces, extension of the treatments from homophase to heterophase interfaces is included with the discussion of each model in this chapter on homophase interfaces.

13.2.1. Dislocation Models

Symmetrical Tilt Grain Boundary One of the simplest types of grain boundaries to visualize is a symmetrical tilt boundary, where two grains on either side of the boundary are related by symmetrical rotations about an axis lying in the boundary plane. Figure 13.3 illustrates such a boundary in a simple cubic structure, where the boundary was formed by joining two crystals having surfaces rotated from a cube plane by $\pm\theta/2$ about a <100> axis. When the two surfaces are joined, the ledges on them become edge dislocations of Burgers vector **b**, where the magnitude of the

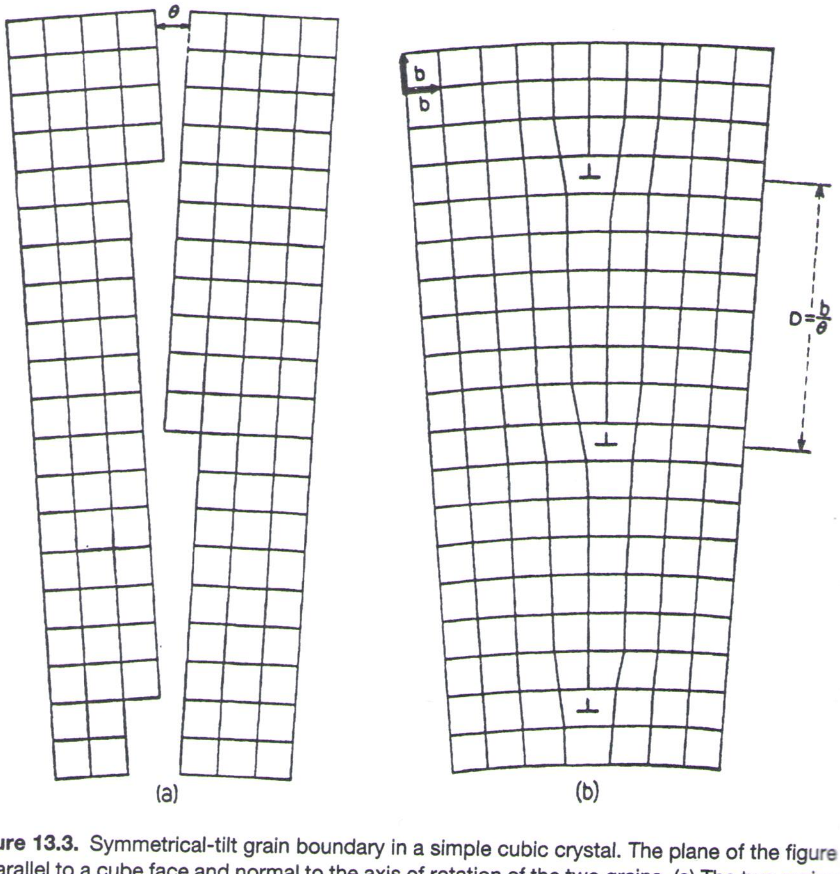

(a) (b)

Figure 13.3. Symmetrical-tilt grain boundary in a simple cubic crystal. The plane of the figure is parallel to a cube face and normal to the axis of rotation of the two grains. (a) The two grains are rotated by an angle θ and (b) joined to form a bicrystal (grain boundary). From [25].

Burgers vector $b = |\mathbf{b}|$ is equal to the ledge height h_l. A similar tilt boundary for an atomistic model with {111} surfaces and a <110> tilt axis was previously shown in Figure 12.2b. Joining the crystals in Figure 13.3b requires only elastic strain except where planes of atoms terminate at the boundary in an edge dislocation, indicated by the symbol ⊥. Here the atoms have fewer nearest neighbors than in the bulk.

From the geometry in Figure 13.3b, the number of edge dislocations per unit length in the grain boundary is given by

$$\frac{1}{D} = \frac{2\sin(\theta/2)}{b} \tag{13.2a}$$

or when θ is small by

$$\frac{1}{D} \cong \theta/b, \tag{13.2b}$$

---

where D is the dist
constitutes a wall o
energy of such an
Poisson's ratio ν. A
tion has an elastic st
ing between the disl
a function of θ to f
then given by the pr
the density of the dis
for the energy per u

where

and r_0 represents the
ary energy γ_{gb} has u

The term A_0 in
dislocation per unit a
tic energy of the bou
tion, and it leads to a
dislocations. The sec
dislocations overlap
only be applied to bo
that the cores of the
low-angle tilt bounda
energetically favorab
θ_2 to combine to for
entiation of Eq. (13.3

A plot of Eq. (
θ = 0 is very sharp w
at θ = 0. This is bec
ledge is pressed into
energy of a tilt bound
strain field of each
when they are widely
at solid–vapor interfa
the surface energy of
becomes less steep a
and eventually the slo
location concept of a
boundary has many c

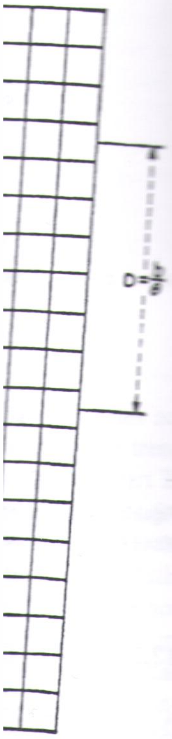

plane of the figure
. (a) The two grains
From [25].

boundary for an
riously shown in
tic strain except
ion, indicated by
he bulk.
cations per unit

(13.2a)

(13.2b)

---

where D is the distance between the grain boundary dislocations. This boundary constitutes a wall of dislocations and Read and Shockley [26] have calculated the energy of such an array, situated in an infinite medium of shear modulus μ and Poisson's ratio ν. An important consideration in their analysis is that each dislocation has an elastic strain energy per unit length $E_\perp$ that varies according to the spacing between the dislocations D. Thus, the elastic strain energy must be integrated as a function of θ to find its angular dependence. The grain boundary energy γ_{gb} is then given by the product of the energy per unit length of the dislocations $E_\perp$ times the density of the dislocations as $\gamma_{gb} = E_\perp(1/D) = E_\perp(\theta/b)$. The resulting expression for the energy per unit area of the grain boundary γ_{gb} is given by

$$\gamma_{gb} = E_0\theta(A_0 - \ln\theta), \tag{13.3a}$$

where

$$E_0 = \frac{\mu b}{4\pi(1-\nu)} \quad \text{and} \quad A_0 = 1 + \ln\left(\frac{b}{2\pi r_0}\right) \tag{13.3b}$$

and r_0 represents the core energy of a single boundary dislocation. The grain boundary energy γ_{gb} has units of energy per unit area (mJ/m^2).

The term A_0 in parentheses in Eq. (13.3) depends on the total core energy of the dislocation per unit area of the boundary, whereas the $\ln\theta$ term accounts for the elastic energy of the boundary. The first term represents a constant energy per dislocation, and it leads to an increase in the energy that is proportional to the density of the dislocations. The second term decreases as θ increases because the stress fields of the dislocations overlap and cancel one another as D decreases. Hence, this equation can only be applied to boundaries having a small angle of tilt ($\theta \sim 10$–15 degrees) such that the cores of the dislocations do not overlap. Such boundaries are referred to as low-angle tilt boundaries. Also note that the Read–Shockley equation shows that it is energetically favorable for two low-angle tilt boundaries with misorientations θ_1 and θ_2 to combine to form a single tilt boundary with angle $(\theta_1 + \theta_2)$. In addition, differentiation of Eq. (13.3a) predicts that γ_{gb} has a maximum at $\theta = \exp(A_0 - 1)$.

A plot of Eq. (13.3a) is shown in Figure 13.4, where it is seen that the cusp at $\theta = 0$ is very sharp when the boundary disappears; that is, $d\gamma_{gb}/d\theta$ becomes infinite at $\theta = 0$. This is because a long-range stress field is established when an isolated ledge is pressed into another crystal to make a grain boundary dislocation. Thus, the energy of a tilt boundary rises steeply as its angle increases from zero because the strain field of each dislocation spreads out to very large distances in the crystal when they are widely separated. This contrasts with the much shallower cusps found at solid–vapor interfaces, where the energy is localized at the ledges and reverts to the surface energy of the singular surface when $\theta = 0$. In the tilt boundary, the slope becomes less steep as the stress fields approach one another and begin to cancel, and eventually the slope becomes almost constant at high tilt angles. Using this dislocation concept of a low-angle symmetrical tilt grain boundary, we see that the boundary has many characteristics that are similar to vicinal solid–vapor interfaces,

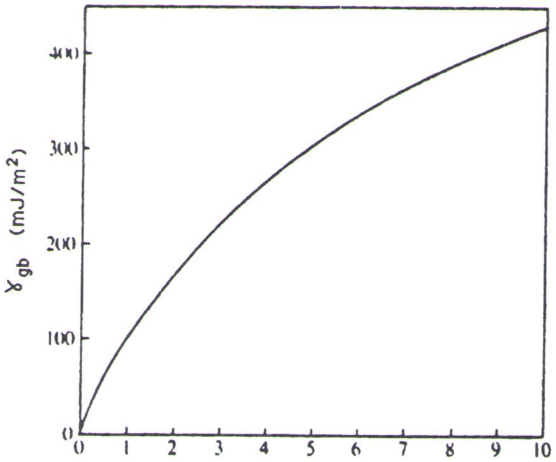

Figure 13.4. Energy of a tilt grain boundary as a function of tilt angle θ with $E_0 = 1450$ mJ/m^2 (appropriate for copper) and $A_0 = 0$. Reprinted from [31] by permission of Addison-Wesley Longman Publishing Company, Inc.

such as a low energy cusp at low tilt angles, but that the nature of the elastic strains are an additional important part of this solid–solid interface.

Although the dislocation model was developed for low-angle grain boundaries where the dislocation cores are well-defined and surrounded by regions of relatively well-bonded crystal, it can be extended on a purely geometrical basis to high-angle boundaries. If the angular tilt is continued beyond the low-angle regime, the energy is expected to increase only slightly as the density of dislocation cores increases and shallow cusps are expected to occur at particular angles of tilt where the dislocations are uniformly spaced. According to the formula for a simple cubic lattice, this occurs when $\cot(\theta/2) = 2n$, where n is an integer. For example, when $\cot(\theta/2) = 14$, there is one dislocation on every seventh cube plane, or when $\cot(\theta/2) = 2$ (or $\theta = 53°$) the structure is particularly simple and forms a twin plane, as shown in Figure 13.5. In this case, the twin plane is (210), and the atoms in the twin boundary lie on the lattices of both grains. The density of atoms on the boundary plane is high, and the resulting grain boundary energy is low. This type of boundary is sometimes referred to as a special high-angle grain boundary.

A uniform dislocation spacing in a high-angle grain boundary such as in Figure 13.5 only results when the dislocation spacing is an integral number of lattice planes terminating at the boundary as illustrated in Figure 13.6a. When the misorientation changes in a symmetrical high-angle tilt grain boundary, the dislocation spacing ideally varies from uniform to nonuniform, as shown schematically in Figure 13.6. A nonuniform grain boundary can be described as consisting of a uniform dislocation array and a superimposed nonuniform array. For example, the nonuniform 60° symmetrical-tilt boundary in Figure 13.6b can be described as a 53° tilt

Figure 13.5. High-angle
to the plane of the figure
both grains. From [27].

boundary (Fig. 13.6a)
the boundary once aga
illustrated in Figure 13
aries has been calculate
perimposed dislocation
tilt in Figure 13.7 corre

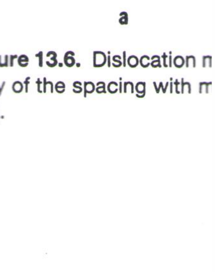

Figure 13.6. Dislocation
nity of the spacing with
[24].

ith E_0 = 1450 mJ/m^2
of Addison-Wesley

the elastic strains

ngle grain bound-
l by regions of rel-
ometrical basis to
low-angle regime,
dislocation cores
ngles of tilt where
for a simple cubic
xample, when cot
r when cot (θ/2) =
n plane, as shown
in the twin bound-
boundary plane is
boundary is some-

ry such as in Fig-
number of lattice
When the misori-
y, the dislocation
ematically in Fig-
sting of a uniform
mple, the nonuni-
ribed as a 53° tilt

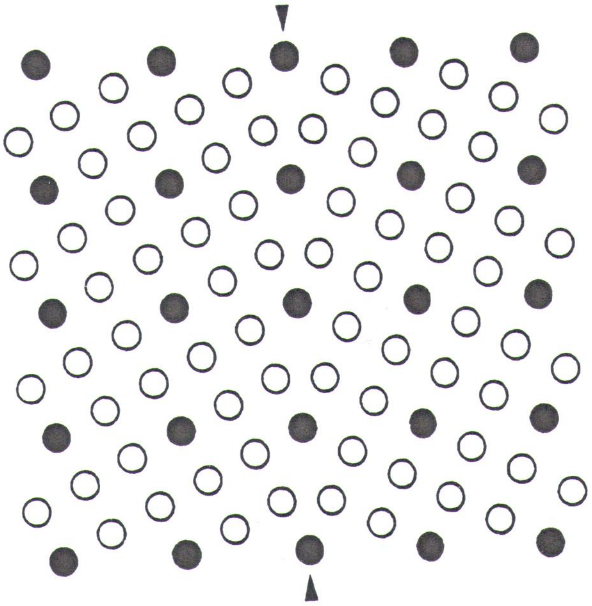

Figure 13.5. High-angle tilt boundary of good fit. The (210) twin boundary (arrows) is normal to the plane of the figure and the dark circles represent atoms that lie on points of lattices of both grains. From [27].

boundary (Fig. 13.6a) with a superimposed 7° tilt boundary. With further tilt to 62°, the boundary once again becomes uniform but with a higher dislocation density, as illustrated in Figure 13.6c. The variation in energy of such symmetrical tilt boundaries has been calculated assuming that the energy consists of the sum of the two superimposed dislocation arrays and is shown in Figure 13.7. Note the cusp at a 53° tilt in Figure 13.7 corresponding to the (210) boundary in Figure 13.5.

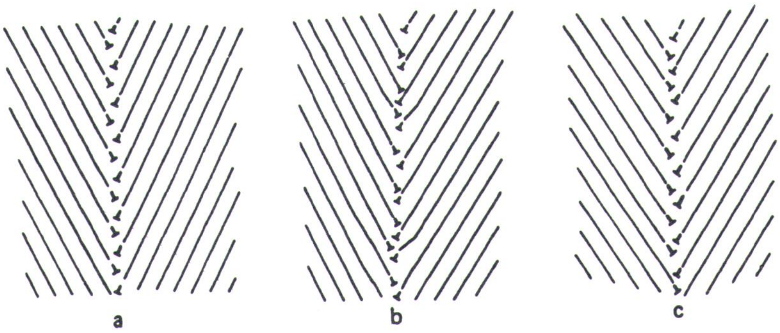

Figure 13.6. Dislocation models of symmetrical tilt boundaries showing the variation in uniformity of the spacing with misorientation angle: (a) 53°, (b) 60° and (c) 62° misorientation. From [24].

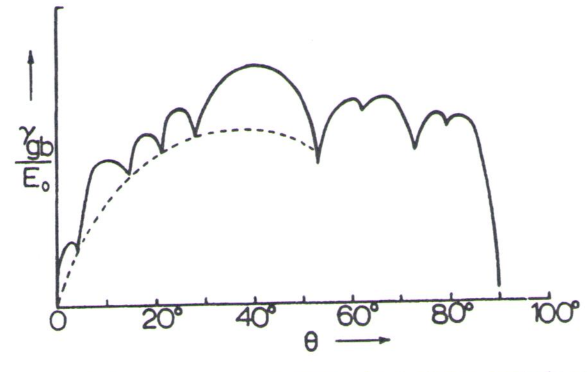

Figure 13.7. Relative grain boundary energy versus misorientation angle for symmetrical tilt boundaries which vary in uniformity of dislocation arrays. Cusps correspond to uniform arrays. From [24,28].

Both atomistic calculation and experimental data suggest that the cusps shown in Figure 13.7 exist. For example, Figures 13.8a and b compare calculated and experimental data for the grain boundary energies of symmetrical <100> and <110> grain boundaries in f.c.c. aluminum. The calculations were performed using a Morse potential for aluminum, similar to the 6–12 Lennard–Jones potential that we have used frequently in this book. The atomistic calculations are similar to but more realistic than the pure dislocation model described above, because they allow for atomic relaxations and translations along the boundary that are not included in the dislocation model. The experimental and calculated curves in Figure 13.8 are in generally good agreement, although the small cusps associated with the <100> tilt boundary in Figure 13.8a are not evident experimentally in Figure 13.8b due to their relatively small magnitude compared to the scatter in the data. In contrast, the large cusps at about 70° and 129° in Figures 13.8c and d are clearly evident, and these are associated with low-energy {111} and {113} twin boundaries which are possible with rotation about the <110> axis. The {111} twin boundary was shown previously in Figure 12.1. Note that the magnitudes of the calculated grain boundary energies in Figure 13.8 are about twice the measured values given in Table 13.1.

We look at atomistic calculations of grain boundary structures in depth in a subsequent section, but it is worth noting that plots like Figures 13.7 and 13.8 resemble the γ^{SV} plots seen previously in Chapters 3 and 4. A slightly different type of plot could also be obtained by maintaining a constant angle of tilt between two crystals and varying the grain boundary plane. This would be very much analogous to the γ^{SV} plots for solid–vapor interfaces in Section 3.4. Certain orientations of the plane will have particularly low energies, and these will likely become facet planes of enclosed crystals. An example of this is illustrated below in our discussion of the asymmetrical tilt boundary.

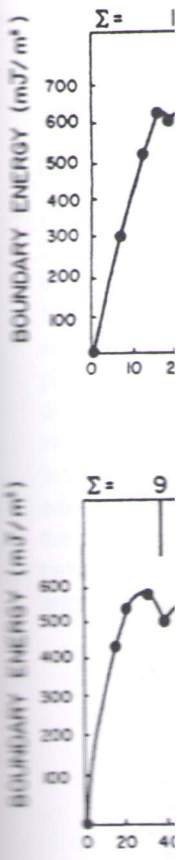

Figure 13.8. (
misorientation
Reprinted fro
Netherlands.

Asymmetri
turned out of
angle Φ, as i
the boundary
makes an ang
with the [10
Φ = 0 or 90
extra planes
shown that t

ngle for symmetrical tilt
spond to uniform arrays.

ggest that the cusps
compare calculated
nmetrical <100> and
were performed us-
nard–Jones potential
lations are similar to
above, because they
dary that are not in-
ated curves in Figure
s associated with the
ntally in Figure 13.8b
r in the data. In con-
and d are clearly ev-
13} twin boundaries
111} twin boundary
des of the calculated
easured values given

uctures in depth in a
res 13.7 and 13.8 re-
ghtly different type of
ilt between two crys-
y much analogous to
n orientations of the
become facet planes
our discussion of the

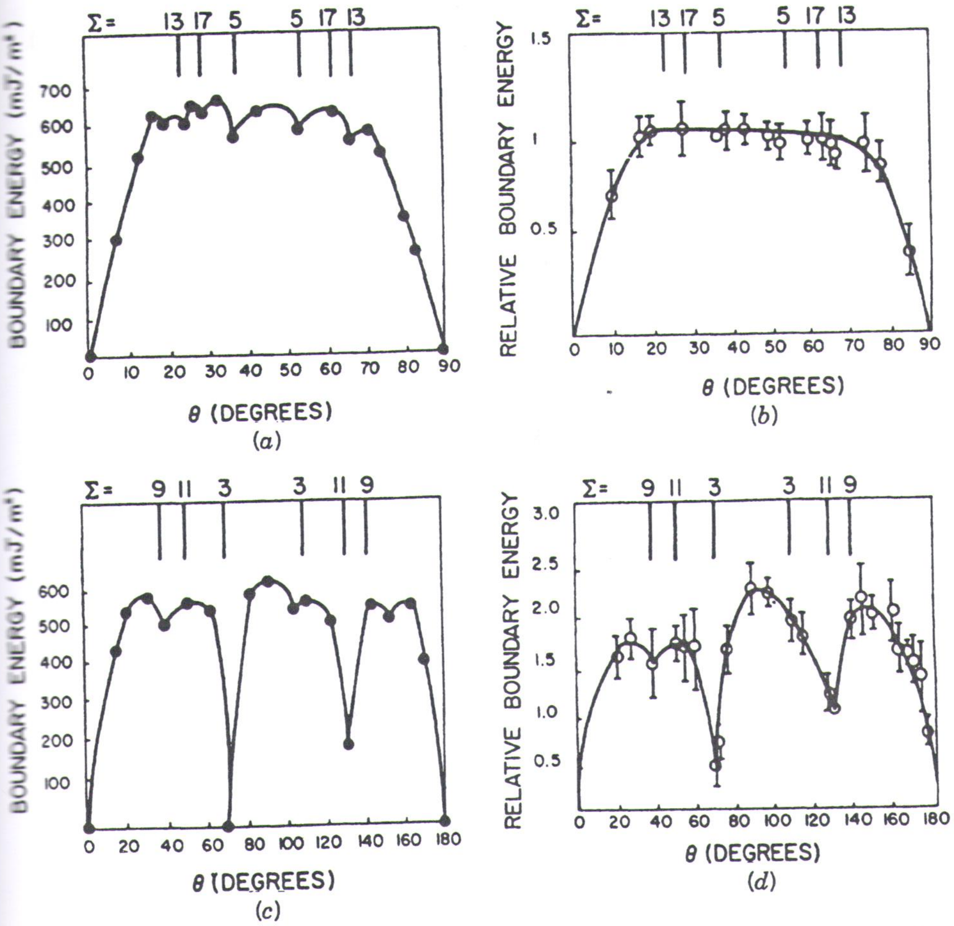

Figure 13.8. (a,c) Calculated and (b,d) experimental grain boundary energies as a function of misorientation angle for (a,b) <100> and (c,d) <110> symmetrical tilt boundaries in aluminum. Reprinted from [29,30] with kind permission from Elsevier Science-NL, Amsterdam, The Netherlands.

Asymmetrical Tilt Grain Boundary The tilt boundary in Figure 13.3b can be turned out of its symmetrical orientation by rotating it about the tilt axis through an angle Φ, as illustrated in Figure 13.9. In this case, the angle Φ is the angle between the boundary plane and the mean <100> direction of the two grains. The boundary makes an angle of $\Phi + \theta/2$ with the [100] direction in one grain and angle of $\Phi - \theta/2$ with the [100] direction in the other grain. Figure 13.3 is thus a special case where $\Phi = 0$ or 90°. When the boundary becomes asymmetrical, edge dislocations with extra planes that are normal to those of the original set are introduced, and it can be shown that their spacing [25] is given by

$$D_2 = \frac{b_2}{\theta \sin \Phi}, \tag{13.4a}$$

whereas the spacing of the original set is reduced to

$$D_1 = \frac{b_1}{\theta \cos \Phi}. \tag{13.4b}$$

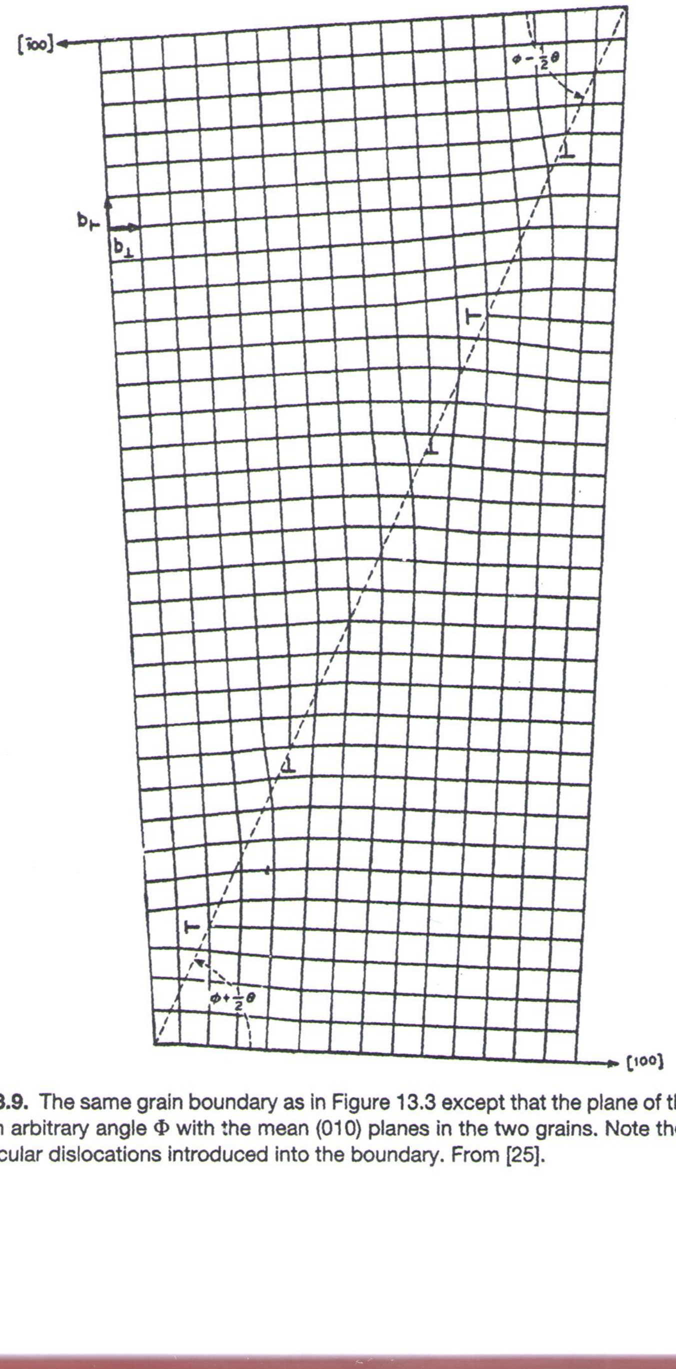

Figure 13.9. The same grain boundary as in Figure 13.3 except that the plane of the boundary makes an arbitrary angle Φ with the mean (010) planes in the two grains. Note the new set of perpendicular dislocations introduced into the boundary. From [25].

The new dislocations inc
from zero because they ar
gy of this boundary has th
ditional dependence on Φ

Twist Grain Boundary
is produced by rotating th
the plane of the boundary
to the <100> axis about
boundary. It consists of a
screw dislocations are visi
placement parallel to the
drawn parallel to a [100]
twist boundary, such as Fi
intersects per unit length,
edge dislocations in a tilt
the magnitude of the Burg
twist boundary increases
ergy of a tilt boundary inc

Figure 13.10. A pure (relaxed
ary is in the plane of the figu
normal to the boundary. The
ary in one grain and the solid
terface have been relaxed to
gions of poor matching (*B*), w

(13.4a)

(13.4b)

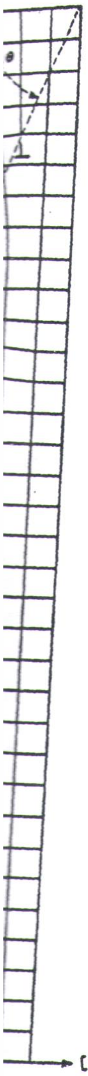

the plane of the boundary
rains. Note the new set of

The new dislocations increase the energy of the boundary sharply as Φ increases from zero because they are far apart. Shockley and Read [26] showed that the energy of this boundary has the same form as the symmetrical tilt boundary with an additional dependence on Φ and that a sharp cusp exists when $\Phi = 0$.

Twist Grain Boundary A more drastic change in the grain boundary structure is produced by rotating the tilt boundary in Figure 13.3 through 90° about an axis in the plane of the boundary and normal to the tilt axis. The boundary is then normal to the <100> axis about which the two grains are rotated, and it is called a twist boundary. It consists of a grid of screw dislocations, as shown in Figure 13.10. The screw dislocations are visible as regions of poor matching where there is a shear displacement parallel to the lines of distortion. It can be shown [31] that if a vector is drawn parallel to a [100] direction in the mean lattice between the two grains in a twist boundary, such as Figure 13.10, the number of [010] screw dislocations that it intersects per unit length, is given by the same formula as that for the number of edge dislocations in a tilt boundary in Eq. (13.2), or $1/D = (2 \sin \theta/2)/b$, where b is the magnitude of the Burgers vector of the screw dislocation. Thus, the energy of a twist boundary increases with the angle of twist in the same general way as the energy of a tilt boundary increases with the angle of tilt.

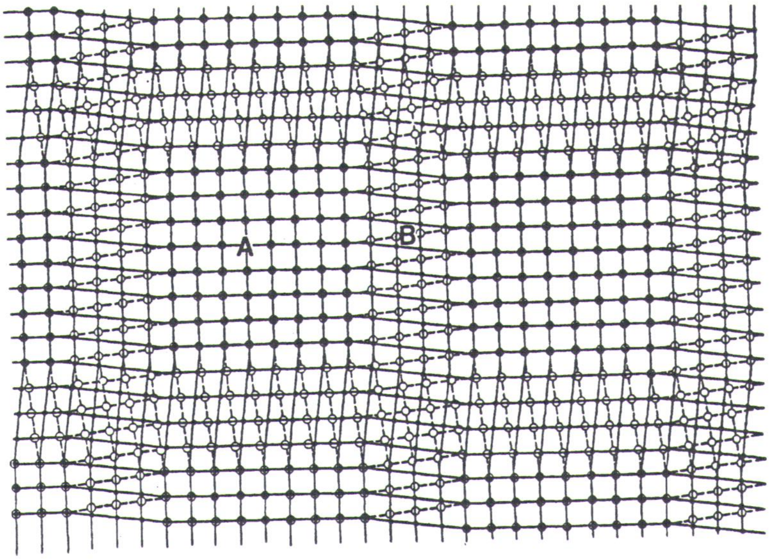

Figure 13.10. A pure (relaxed) twist boundary between two simple cubic crystals. The boundary is in the plane of the figure and the two grains have a small rotation about the cube axis normal to the boundary. The open circles represent atoms just above the plane of the boundary in one grain and the solid circles atoms just below in the opposite grain. Atoms at the interface have been relaxed to produce regions of good atomic matching (*A*) separated by regions of poor matching (*B*), which are the screw dislocations. From [25].

As for tilt boundaries, the energy of a twist boundary should be cusped at angles of twist at which the atoms fit well together in the boundary, although atomistic calculation has shown that these cusps are generally much shallower. For example, the 53° rotation about <100> that produced a cusp in the energy of the cubic tilt boundary, also produces a twist boundary normal to <100> on which the atoms fit uniformly. This is shown in Figure 3.11, where the net of lattice points common to both grains in Figure 3.11 and the similar net of coincident points lying on the corresponding tilt boundary in Figure 13.5, are indicated in each figure. Thus, both boundaries lie on a plane of the coincident atom sites in the two crystals.

Unlike the edge dislocation networks shown in Figures 12.2 and 13.3, it is not possible to reveal the atomic structure of screw dislocation networks by HRTEM, because their Burgers vector lies parallel to the line direction of the dislocations. That is, there is no displacement of the atomic columns perpendicular to the viewing direction when the boundary is edge-on. However, these dislocations can be observed by diffraction contrast imaging techniques in the TEM [32,33] (as can edge or mixed dislocations). Figure 13.12a shows a bright-field TEM image of the dislocation structure in a (001) pure twist low-angle boundary in gold [33,34]. The interface is oriented normal to the viewing direction, and the dislocations are visible as

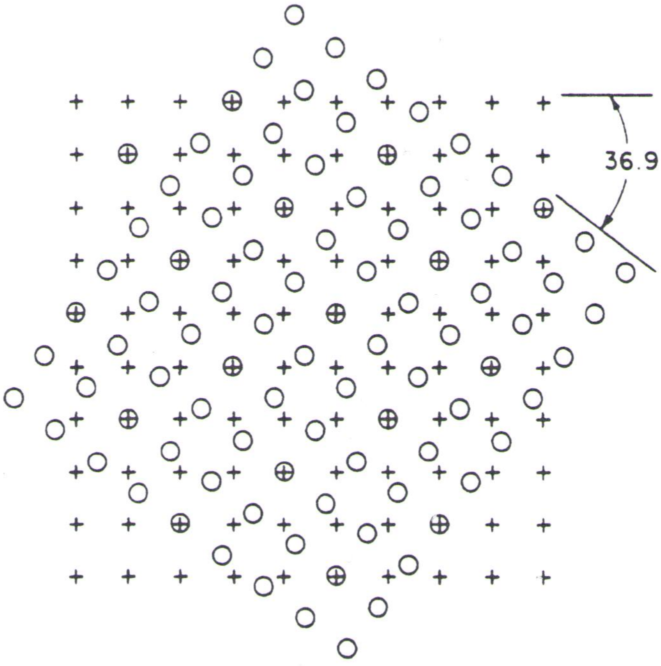

Figure 13.11. Twist boundary of good fit in a simple cubic lattice. The boundary is parallel to the plane of the figure. One lattice is indicated by circles and the other by crosses so that the coincident positions are easily visible. From [27].

be cusped at an-
though atomistic
'er. For example,
of the cubic tilt
ich the atoms fit
oints common to
lying on the cor-
gure. Thus, both
stals.
ind 13.3, it is not
rks by HRTEM,
the dislocations.
ular to the view-
ations can be ob-
33] (as can edge
age of the dislo-
3,34]. The inter-
ns are visible as

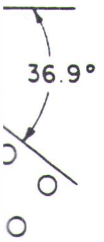

ndary is parallel to
crosses so that the

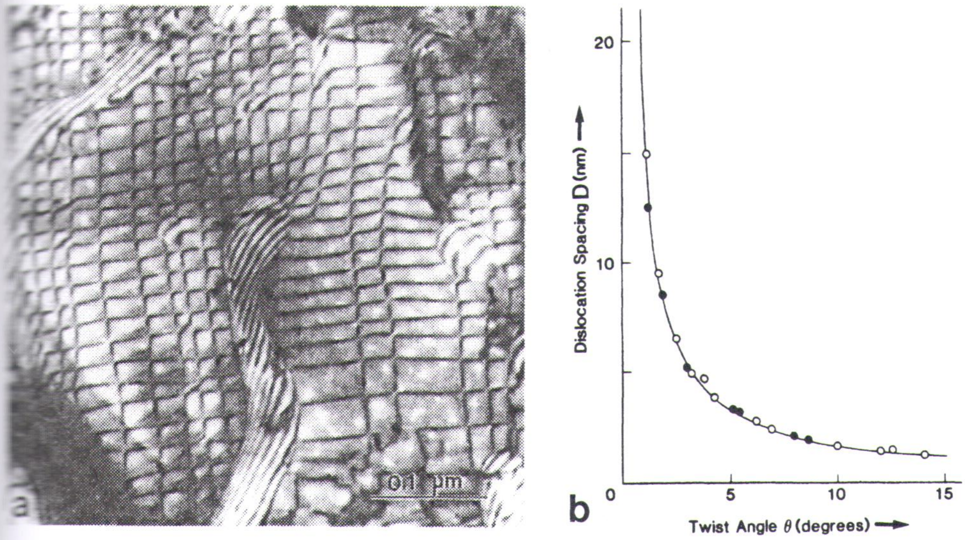

Figure 13.12. (a) Bright field TEM image of a cross-grid of screw dislocations in a pure twist boundary ($\theta = 1°$) in gold. From [34] copyright Taylor & Francis Ltd. (b) Comparison of experimental and calculated spacings of dislocations for (001) twist boundaries in gold. From [33]. The filled circles are the results of Schober and Balluffi [34] and the open circles are from the results of Tan et al. [35].

dark lines in the interface. The boundary consists of an orthogonal array of screw dislocations in agreement with the model shown in Figure 13.10. In their investigation, Schober and Balluffi [34] examined a series of such twist boundaries with misorientations of 1 to 9 degrees and used contrast analyses to establish that the two sets of dislocations in the boundary had Burgers vectors $\mathbf{b} = 1/2[110]$ and $1/2[1\bar{1}0]$. Their results showed that the screw dislocation spacing in the grain boundary varied with θ as expected from the simple relation $D = b/\theta$, as illustrated in Figure 13.12b. The same type of data were also generated for low-angle tilt boundaries and found to agree with the predictions of Eq. (13.2).

Degrees of Freedom of a General Grain Boundary The symmetrical tilt boundary in Figure 13.3 is a special type of boundary, which can be specified by the axis of tilt and the single angle θ. A general grain boundary has five degrees of freedom (DOF), or five quantities that are required to define it. These are often referred to as the five macroscopic degrees of freedom of a general grain boundary. Three values are required to specify the rotation that brings the lattice of one grain parallel to the other and two more values are required to specify the orientation of the boundary plane with respect to one of the grains. These features are illustrated in Figure 13.13. In this figure, we imagine that we cut a crystal along two arbitrary planes, take out the wedge-shaped material in between the two cuts, and bring the two grains together with a twist. The resulting boundary has five degrees of free-

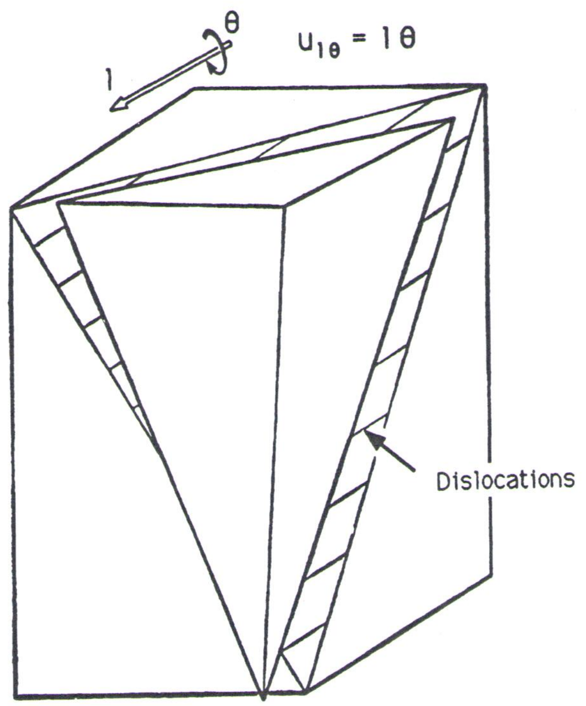

Figure 13.13. Formation of a general grain boundary with five degrees of freedom. In this figure, the misorientation is specified by a rotation θ about a common axis **l** in both grains. In a pure tilt boundary, **l** lies in the plane of the boundary and leads to a set of parallel edge dislocations, indicated by lines on the exposed crystal surface. The vector **l** is normal to the boundary plane in a pure twist boundary. From [25].

dom. If **l** is taken as a unit vector parallel to the axis of relative rotation of the two grains, the rotation between the two grains can be represented by the vector

$$\mathbf{u}_{l\theta} = \mathbf{l}\theta, \tag{13.5}$$

which has three independent components or DOF. The orientation of the boundary may then be specified by a unit vector **n** normal to the boundary plane, which requires two additional DOF. A pure twist boundary is thus defined as one where **l** is parallel to **n** and for a pure tilt boundary **l** is perpendicular **n**. The quantity **l**θ is often called the axis-angle pair for the grain boundary.

There are various ways of expressing the crystallography of a grain boundary using the five degrees of freedom [2]. One method, which is similar to Figure 13.13 but emphasizes the importance of the interface plane relative to the two grains is illustrated in Figure 13.14. In this figure, we create a general grain boundary by a twist rotation θ about the common grain-boundary plane normal **n**, which is parallel

---

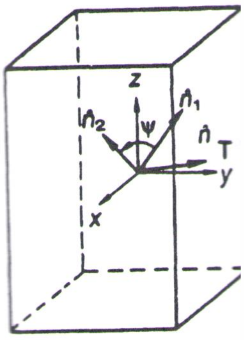

(a)

Figure 13.14. Illustra
interface using the in
(x,y,z) coordinate syst
parallel to $\mathbf{n}_2$, and (c)
by the angle θ. From [

to the surface norm
The degrees of free

or in cubic crystal
planes instead of th

The twist compone
governed by θ and
governed by the co

and

where $\mathbf{n}_T$ is a unit
tilt angle, as illustra
face-plane scheme

cations

of freedom. In this fig-
dis l in both grains. In a
t of parallel edge dislo-
is normal to the bound-

e rotation of the two
y the vector

(13.5)

tion of the boundary
ary plane, which re-
ned as one where l is
The quantity lθ is of-

of a grain boundary
nilar to Figure 13.13
the two grains is il-
grain boundary by a
l **n**, which is parallel

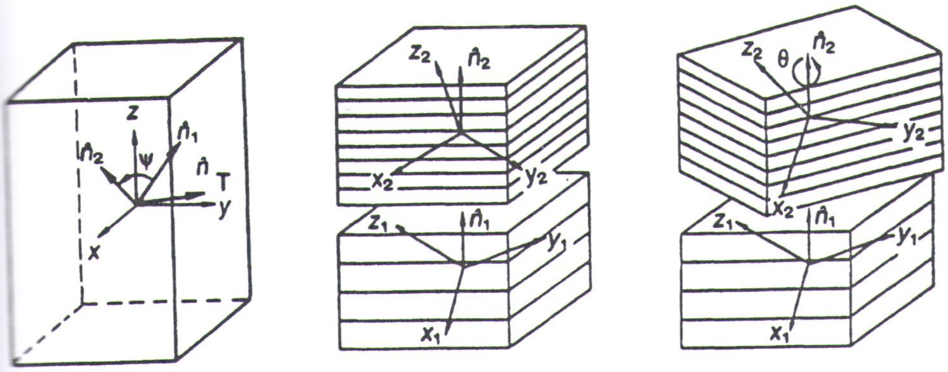

(a) (b) (c)

Figure 13.14. Illustration of the five macroscopic degrees of freedom of an arbitrary bicrystal interface using the interface-plane scheme. (a) The orientations of $\mathbf{n}_1$, $\mathbf{n}_2$ and $\mathbf{n}_T$ in a fixed (x,y,z) coordinate system, (b) a tilt rotation of the two crystal coordinate systems so that $\mathbf{n}_1$ is parallel to $\mathbf{n}_2$, and (c) introduction of the twist component by rotating the top crystal about $\mathbf{n}$ by the angle θ. From [2].

to the surface normals, $\mathbf{n}_1$ and $\mathbf{n}_2$, of the two grains that form the grain boundary. The degrees of freedom (DOF) of the grain boundary can then be specified as

$$\text{DOF} = \{\mathbf{n}_1, \mathbf{n}_2, \theta\} \tag{13.6a}$$

or in cubic crystals, where it is possible to use the Miller indices of the crystal planes instead of their normals, Eq. (13.6a) is conveniently expressed as

$$\text{DOF} = \{(hkl)_1, (hkl)_2, \theta\}. \tag{13.6b}$$

The twist component $(\mathbf{n}_1, \theta)$ of a general grain boundary described by Eq. (13.6a) is governed by θ and the grain boundary normal $\mathbf{n}$, whereas its tilt component $(\mathbf{n}_T, \psi)$, governed by the condition that $\mathbf{n}_T$ is perpendicular to $\mathbf{n}_1, \mathbf{n}_2$, is given by

$$\mathbf{n}_T = \frac{[\mathbf{n}_1 \times \mathbf{n}_2]}{\sin\psi} \tag{13.7a}$$

and

$$\sin\psi = |\mathbf{n}_1 \times \mathbf{n}_2|, \tag{13.7b}$$

where $\mathbf{n}_T$ is a unit vector defining the orientation of the tilt axis and ψ denotes the tilt angle, as illustrated in Figure 13.14. Using this method, referred to as the interface-plane scheme [2], $\psi = 0$ for a pure twist boundary with twist angle θ, and $\theta = 0$

for a pure tilt boundary with tilt angle ψ. A general grain boundary thus has values for both θ and ψ.

The interface-plane scheme developed for grain boundaries is similar to the notation that is often used to describe the interface plane or orientation relationship between two different phases at a heterophase interface. In the case of two different phases α and β, the interface is often specified by a set of parallel (hkl) planes and $[uvw]$ directions in the two phases as

$$(hkl)_\alpha \| (hkl)_\beta;\ [uvw]_\alpha \| [uvw]_\beta, \tag{13.8}$$

where the symbol $\|$ is used to indicate the parallel relationship and the $[uvw]$ directions are contained in the parallel (hkl) planes [36]. Specifying a set of parallel directions within the (hkl) planes is similar to specifying a rotation angle θ, as in Eq. (13.6a). It is often found that heterophase interfaces do not lie along the parallel set of planes in the two phases given by Eq. (13.8). In this case, it is common to specify the orientation relationship between the two phases according to Eq. (13.8) and then to denote the interface plane as an (hkl) plane in either (or both) of the phases. For the situation of precipitates in a matrix, the matrix plane is often chosen. An example of such notation is shown by the $(474)_\gamma$ interface in Figure 12.7, and additional examples are discussed in Section 14.6.1.

In addition to the five macroscopic degrees of freedom, there are three independent translational (or so-called microscopic) degrees of freedom for a grain boundary involving translations $\mathbf{T} = (T_x, T_y, T_z)$ parallel (x, y) and perpendicular (z) to the interface plane. Computer simulations and HRTEM have shown that such translations occur frequently at grain boundaries. From a thermodynamic viewpoint the z component of $\mathbf{T}$ perpendicular to the interface is important, because it accounts for any volume expansion in the interface. Such an excess free volume at the interface is expected to be closely related to its excess free energy and to give rise to stresses near the interface that are similar to the well-known surface stress discussed with regard to surfaces in Part II. This so-called excess free volume per unit area of the interface [2] is defined by

$$\Delta V_i = (\partial V/\partial A)_{T,P,N_i}, \tag{13.9}$$

where the volume expansion is given in units of the lattice parameter. We see in a later section on atomistic modeling of grain boundaries that this volume expansion is an important parameter related to the grain boundary energy.

Frank's Formula for the Dislocation Content of a Boundary The dislocation content of a general grain boundary can be determined according to the theory of Frank [37]. The same procedure can be applied to heterophase interfaces where there is a change in crystal structure across the interface [1,38]. This theory is illustrated for a grain boundary geometrically in Figure 13.15. In Figure 13.15a, a reference lattice has been cut along AA' by a plane with a normal specified by the

Figure 13.15. Ill
planar grain bou
– by an angle θ
through the poin

ndary thus has values

aries is similar to the
ientation relationship
case of two different
allel (*hkl*) planes and

(13.8)

and the [*uvw*] direc-
g a set of parallel di-
ion angle θ, as in Eq.
along the parallel set
is common to specify
o Eq. (13.8) and then
th) of the phases. For
en chosen. An exam-
12.7, and additional

there are three inde-
freedom for a grain
and perpendicular (*z*)
ave shown that such
odynamic viewpoint
rtant, because it ac-
ss free volume at the
gy and to give rise to
face stress discussed
lume per unit area of

(13.9)

rameter. We see in a
is volume expansion

undary The dislo-
ccording to the theo-
terophase interfaces
[1,38]. This theory is
In Figure 13.15a, a
mal specified by the

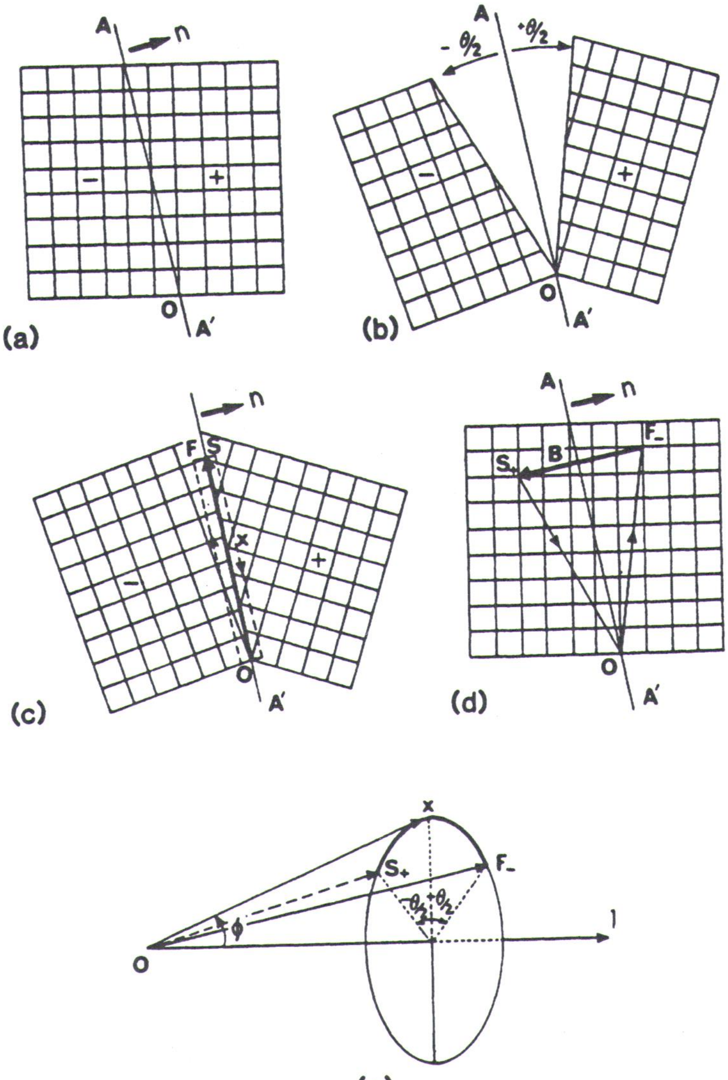

Figure 13.15. Illustration of the derivation of the net Burgers vector **B** crossing a vector **x** in a planar grain boundary *AA′* with unit normal **n**, where lattice + is rotated with respect to lattice − by an angle θ in a right-handed sense about an axis **l** directed into the plane of the page through the point *O*. From [33].

unit vector **n**, so as to divide the lattice into two crystals represented by + and –. In Figure 13.15b, crystal + is rotated by an angle $+\theta/2$ and crystal – by an angle of $-\theta/2$ in a right-handed sense about an axis defined by a unit vector **l** passing through the lattice point *O* and directed into the page. In Figure 13.15c, these two misoriented lattices are extended until they join at the original cut, forming a grain boundary. A vector **x**, which can have any direction in this boundary plane, is then chosen to extend from the origin *O* over several unit cells, as illustrated in Figure 13.15c. The net Burgers vector of the dislocations in the grain boundary which intersects **x** can be determined by comparing a Burgers circuit containing the vector **x** in the bicrystal with an equivalent circuit in the reference lattice. This is done using the finish-to-start, right-hand (FS/RH) convention [25,39] with the closure failure being made in the good crystal. The circuit in the bicrystal (Fig. 13.15c) is a closed circuit made in a right-handed sense around an axis parallel to $(\mathbf{x} \times \mathbf{n})$, where **n** is defined as pointing from crystal – into crystal +. This circuit is also made in a right-handed sense with respect to the rotation axis **l**. The circuit starts at *S*, the end-point of the vector **x** extends through crystal + to the origin *O* and then returns through crystal – to the point *F*, which is coincident with *S*. In the reference lattice redrawn in Figure 13.15d, the first part of the circuit *SO* in the crystal + is represented by S_+O and the second part of the circuit, *OF* in crystal –, is represented by OF_-. There is clearly a closure failure $F_-S_+ = \mathbf{B}$ in the reference lattice, and this defines the net Burgers vector of those dislocations contained in the boundary that are intersected by the vector **x**. In general, the vector **x** makes an angle Φ with **l** as shown in Figure 13.15e, so the resulting vector **B** has a magnitude given by

$$|\mathbf{B}| = |\mathbf{x}| 2 \sin(\theta/2) \sin \Phi \tag{13.10}$$

with a direction along $(\mathbf{x} \times \mathbf{l})$. Furthermore, because

$$|\mathbf{x} \times \mathbf{l}| = |\mathbf{x}| \sin \Phi, \tag{13.11}$$

then

$$\mathbf{B} = (\mathbf{x} \times \mathbf{l}) 2 \sin(\theta/2), \tag{13.12a}$$

which, for small θ, yields

$$\mathbf{B} = (\mathbf{x} \times \mathbf{l})\theta. \tag{13.12b}$$

Equation (13.12b) is the general formula derived by Frank for the net Burgers vector of the dislocations required geometrically to accommodate the misorientation at a general grain boundary. The quantity **B** is the sum of the Burgers vectors of all the dislocations intersected by **x** or

$$\mathbf{B} = \sum_i n_i \mathbf{b}_i, \tag{13.13}$$

---

where n_i is the number
Burgers vector **B** of
boundary dislocations
rections parallel to uni
Eq. (13.12) can be wri

where the values of n_i
is a vector in the plane
tions in the *i*th array,
thus defined as

Several points
they apply only to bou
field (i.e., the elastic
Secondly, the equatio
boundary or their patt
ble dislocation structu
lowest energy. Thirdly
rectly proportional to
equally spaced and pa
tions with different B
of dislocations with th
formula can be applie
dislocations arrangem
tion, and so on, if the
where [25,33] and are

13.2.2. O-Lattice

The Read and Shockl
aries discussed in Se
stand both physically
mentally correct for
model becomes unph
structure and energy
different approaches
capability and accura
sive atomistic simula
high-angle grain bou
The purpose o

ented by + and –. In
by an angle of $-\theta/2$
passing through the
ese two misoriented
a grain boundary. A
s then chosen to ex-
gure 13.15c. The net
intersects **x** can be
or **x** in the bicrystal
using the finish-to-
ilure being made in
osed circuit made in
is defined as point-
right-handed sense
l-point of the vector
ugh crystal – to the
redrawn in Figure
nted by S_+O and the
. There is clearly a
nes the net Burgers
intersected by the
as shown in Figure

(13.10)

(13.11)

(13.12a)

(13.12b)

he net Burgers vec-
ne misorientation at
rs vectors of all the

(13.13)

---

where n_i is the number of dislocations of Burgers vectors $\mathbf{b}_i$ cut by $\mathbf{x}$. When the net Burgers vector $\mathbf{B}$ of Eq. (13.12) arises from three independent arrays of grain boundary dislocations with noncoplanar Burgers vectors $\mathbf{b}_1$, $\mathbf{b}_2$ and $\mathbf{b}_3$, with line directions parallel to unit vectors $\boldsymbol{\xi}_1$, $\boldsymbol{\xi}_2$ and $\boldsymbol{\xi}_3$ and with spacings D_1, D_2 and D_3, then Eq. (13.12) can be written as

$$n_1\mathbf{b}_1 + n_2\mathbf{b}_2 + n_3\mathbf{b}_3 = 2\sin(\theta/2)(\mathbf{x} \times \mathbf{l}), \qquad (13.14)$$

where the values of n_i with their appropriate signs are given by $n_i = \mathbf{N}_i \cdot \mathbf{x}$, where $\mathbf{N}_i$ is a vector in the plane of the boundary normal to the line directions of the dislocations in the ith array, with a magnitude equal to the reciprocal of their spacing. It is thus defined as

$$\mathbf{N}_i = \frac{\mathbf{n} \times \boldsymbol{\xi}_i}{D_i}. \qquad (13.15)$$

Several points should be made regarding Eqs. (13.12) and (13.14). Firstly, they apply only to boundaries that are essentially flat and have no long-range stress field (i.e., the elastic distortion is restricted to the region close to the dislocations). Secondly, the equations do not uniquely determine the dislocations present at the boundary or their pattern for a given crystal and boundary. Thus, a variety of possible dislocation structures could exist and the most probable one is the one with the lowest energy. Thirdly, the density of a given set of dislocations in a boundary is directly proportional to θ for small θ. Fourthly, each set of dislocations is straight, equally spaced and parallel even for a boundary containing several sets of dislocations with different Burgers vectors. Lastly, a general boundary requires three sets of dislocations with three non-coplanar Burgers vectors at the boundary, and Frank's formula can be applied to analyze all possible cases, either to determine the possible dislocations arrangements if $\mathbf{n}$, $\mathbf{l}$ and θ are known, or conversely, to find the orientation, and so on, if the dislocation content is specified. These cases are analyzed elsewhere [25,33] and are not discussed further here.

13.2.2. O-Lattice Formulation

The Read and Shockley dislocation model for low-angle tilt and twist grain boundaries discussed in Section 13.2.1 is appealing because it is relatively easy to understand both physically and analytically and because it has been shown to be experimentally correct for low-angle grain boundaries. Unfortunately, the dislocation model becomes unphysical for high tilt angles, and an alternative description for the structure and energy of high-angle grain boundaries is required. Although several different approaches to this problem have been tried, none has the sort of predictive capability and accuracy that is usually desired. In fact, it is only recently that extensive atomistic simulations have provided sufficient data to explain the properties of high-angle grain boundaries in a simple physical manner [2,7].

The purpose of this book is to explain the structure and properties of interfaces using relatively simple analytical treatments that are based on a nearest-neighbor atomistic model of the interfaces whenever possible. In keeping with this theme, we defer discussion of the atomistic calculations of grain boundary structure and energies until we have considered two methods for quantifying interfacial structure that have gained popularity and that relate to the previous dislocation description of interfacial structure. These are the so-called O-lattice and coincident site lattice/displacement shift complete (CSL/DSC) descriptions of grain and interphase boundary structure. Both treatments are geometrical models based on the matching of hard-sphere atoms across an interface and they complement the previous hard-sphere models used to understand solid–vapor and solid–liquid interfaces in Parts II and III. These theories build on the Read and Shockley dislocation model and Frank's equation for the dislocation content of a grain boundary; we examine them in some detail prior to the atomistic simulations. The O-lattice and CSL/DSC theories are developed for grain boundaries for simplicity, but examples are provided to demonstrate that they can be applied directly to heterophase interfaces.

Bollmann developed a technique for analyzing the structure of grain and interphase interfaces that is quite general and has a number of useful properties [40–43]. His method is based on the concept of the O-lattice, which describes the matching and mismatching of oriented lattices at an interface. We develop this theory by reference to Frank's formula for the Burgers vector content of a general grain boundary in Figure 13.15 and show that in fact, Bollmann's O-lattice equation is mathematically similar to Frank's formula in Eq. (13.12).

If we refer to Figure 13.15d, the net Burgers vector $\mathbf{B}$ of the dislocations in the boundary that are intersected by the vector $\mathbf{x}$ is given by

$$\mathbf{B} = F_- S_+ = OS_+ - OF_-.$$

If $\mathbf{R}_+$ is defined as the rotation tensor $(\mathbf{l}, +\theta/2)$ which transforms the reference lattice into +, and $\mathbf{R}_-$ as the rotation tensor $(\mathbf{l}, -\theta/2)$ which transforms the reference lattice into lattice –, then

$$OS_+ = \mathbf{R}_+^{-1}\mathbf{x} \quad \text{and} \quad OF_- = \mathbf{R}_-^{-1}\mathbf{x},$$

so that

$$\mathbf{B} = (\mathbf{R}_+^{-1} - \mathbf{R}_-^{-1})\mathbf{x}. \tag{13.16}$$

In Eq. (13.16), $\mathbf{B}$ and $\mathbf{x}$ are expressed with respect to the reference lattices in Figures 13.15a and d. However, if one of the lattices is chosen as the reference lattice, say crystal +, and $\mathbf{B}$ and $\mathbf{x}$ are expressed in this lattice, then Eq. (13.16) becomes

$$\mathbf{B} = (\mathbf{I} - \mathbf{R}^{-1})\mathbf{x}, \tag{13.17}$$

where $\mathbf{R}$ is the rotation tensor that transforms lattice + into lattice –, and $\mathbf{I}$ is the identity matrix.

The advantage of expressing the relationship between the two crystals by Eq. (13.17) is that it can be readily generalized to apply to heterophase interfaces by replacing the rotation tensor **R** with a general deformation tensor **A**, which transforms the lattice of crystal + into the lattice of crystal –, and involves a strain as well as a rotation [1,38,44]. Thus, with respect to crystal +, the net Burgers vector of those dislocations contained in the heterophase interface that are intersected by a vector **x** is given by

$$\mathbf{B} = (\mathbf{I} - \mathbf{A}^{-1})\mathbf{x}. \tag{13.18}$$

The properties of Eq. (13.18) are similar to those for the grain boundary described in Eqs. (13.12) and (13.14) in that for a general heterophase interface, **B** must be the resultant Burgers vector of at least three independent arrays of interfacial dislocations with non-coplanar Burgers vectors. Thus, we can write an equation similar to Eq. (13.14) but for the case of two different crystal lattices,

$$n_1\mathbf{b}_1 + n_2\mathbf{b}_2 + n_3\mathbf{b}_3 = (\mathbf{I} - \mathbf{A}^{-1})\mathbf{x}, \tag{13.19}$$

where in this case **n** is the unit vector normal to the heterophase interface and is directed from crystal – into crystal +. The similarity between Eqs. (13.19) and (13.14) indicates that the arrays of dislocations in heterophase interfaces can be considered in the same way as for grain boundaries.

We are now able to derive the basic equation of O-lattice theory after having expressed Eq. (13.18) in a way that is applicable to any type of interface through a matrix **A**, which relates the two crystal lattices. If two misoriented crystal lattices, specified here as 1 and 2 to indicate that they may be different lattice types, are allowed to interpenetrate, there will be a periodic set of points in space (not generally lattice points of either lattice), where, for each point, the internal coordinates in a cell of lattice 1 are identical with the internal coordinates in a cell of lattice 2. This set of points defines Bollmann's O-lattice [40]. In terms of a general deformation tensor **A**, which transforms lattice 1 into lattice 2, a point defined by a vector $\mathbf{x}^{(2)}$ in lattice 2 is generated from a point defined by a vector $\mathbf{x}^{(1)}$ in lattice 1 according to

$$\mathbf{x}^{(2)} = \mathbf{A}\mathbf{x}^{(1)}. \tag{13.20}$$

A point on the O-lattice is therefore defined by a vector $\mathbf{x}^{(O)}$ when $\mathbf{x}^{(2)}$ differs from $\mathbf{x}^{(1)}$ by a translation vector $\mathbf{b}^{(L)}$ of lattice 1, that is, when

$$\mathbf{x}^{(2)} = \mathbf{x}^{(O)} = \mathbf{x}^{(1)} + \mathbf{b}^{(L)} = \mathbf{A}\mathbf{x}^{(1)}. \tag{13.21}$$

From this set of equations, we have

$$\mathbf{b}^{(L)} = (\mathbf{I} - \mathbf{A}^{-1})\mathbf{x}^{(O)}, \tag{13.22}$$

which is the basic equation of O-lattice theory [40]. This equation gives the O-lattice vectors in terms of the vectors of crystal lattice 1. In this equation, $\mathbf{b}^{(L)}$ corresponds to **B** in Eqs. (13.12) or (13.18) and $\mathbf{x}^{(O)}$ corresponds to **x**. Thus, the vectors $\mathbf{x}^{(O)}$ cross dislocations with Burgers vectors summing to $\mathbf{b}^{(L)}$, referred to lattice 1.

As an example, we will derive the O-lattice solution for two simple cubic crystal lattices that are rotated about the [001] axis referring to the coordinate system of lattice 1, as illustrated in Figure 13.16. This example follows the work of Smith and Pond [42]. The transformation tensor **A** is a rotation **R**, which can be written

$$\mathbf{A} = \mathbf{R} = \begin{bmatrix} \cos\theta & -\sin\theta & 0 \\ \sin\theta & \cos\theta & 0 \\ 0 & 0 & 1 \end{bmatrix},$$

so that

$$\mathbf{A}^{-1} = \begin{bmatrix} \cos\theta & \sin\theta & 0 \\ -\sin\theta & \cos\theta & 0 \\ 0 & 0 & 1 \end{bmatrix}$$

and

$$(\mathbf{I} - \mathbf{A}^{-1}) = \begin{bmatrix} 1-\cos\theta & -\sin\theta & 0 \\ \sin\theta & 1-\cos\theta & 0 \\ 0 & 0 & 0 \end{bmatrix}.$$

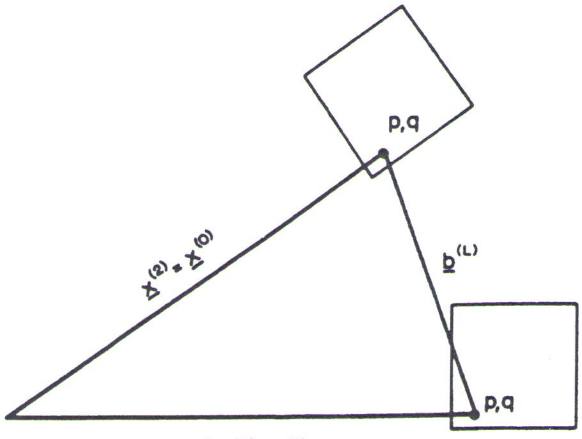

Figure 13.16. Diagram showing the difference vector $\mathbf{b}^{(L)}$ between $\mathbf{x}^{(1)}$ and $\mathbf{x}^{(2)}$ for a simple cubic unit cell having an O-point with internal coordinates (*p*,*q*). From [42].

Substituting $(\mathbf{I} - \mathbf{A}^{-1})$ i

where x_1, x_2 and x_3 an
pression can be written

where $b_3 = 0$ and x_3 ca
uncancelled componen
grain boundary x_3. The
$\mathbf{x}_1^{(O)}$ and $\mathbf{x}_2^{(O)}$, which h
the plane perpendicular
found by assuming a Bu
simultaneously as

so

$\mathbf{x}_{1,2}^{(O)} =$

and the primitive vector

Note that $\mathbf{x}_1^{(O)}$ an
small, Eqs. (13.24) redu
(13.12); that is, the dislo
by θ. Also notice that th
are rational, for example,
viously in Figure 13.5 w
$\mathbf{x}_1^{(O)}$ and $\mathbf{x}_2^{(O)}$ (i.e., it is
thus a crystal lattice site.

Substituting $(\mathbf{I} - \mathbf{A}^{-1})$ into Eq. (13.22) gives

$$\begin{bmatrix} 1-\cos\theta & -\sin\theta & 0 \\ \sin\theta & 1-\cos\theta & 0 \\ 0 & 0 & 0 \end{bmatrix} \begin{bmatrix} x_1 \\ x_2 \\ x_3 \end{bmatrix} = \begin{bmatrix} b_1 \\ b_2 \\ b_3 \end{bmatrix},$$

where x_1, x_2 and x_3 and b_1, b_2 and b_3 are the components of $\mathbf{x}^{(O)}$ and $\mathbf{b}^{(L)}$. This expression can be written explicitly as three linear equations:

$$(1-\cos\theta)x_1 - (\sin\theta)x_2 + 0x_3 = b_1 \tag{13.23a}$$

$$(\sin\theta)x_1 + (1-\cos\theta)x_2 + 0x_3 = b_2 \tag{13.23b}$$

$$0x_1 + 0x_2 + 0x_3 = b_3, \tag{13.23c}$$

where $b_3 = 0$ and x_3 can have any value. Equation (13.23c) means that there are no uncancelled components of the Burgers vector parallel to the rotation axis of the grain boundary x_3. Therefore, the O-lattice consists of lines going through points $\mathbf{x}_1^{(O)}$ and $\mathbf{x}_2^{(O)}$, which have discrete values. The primitive vectors of the O-lattice in the plane perpendicular to the rotation axis (i.e., for a pure twist boundary) can be found by assuming a Burgers vector of unity and solving Eqs. (13.23a) and (13.23b) simultaneously as

$$\begin{bmatrix} 1-\cos\theta & -\sin\theta \\ \sin\theta & 1-\cos\theta \end{bmatrix} \begin{bmatrix} x_1 \\ x_2 \end{bmatrix} = \begin{bmatrix} b_1 \\ b_2 \end{bmatrix},$$

so

$$\mathbf{x}_{1,2}^{(O)} = \begin{bmatrix} x_1 \\ x_2 \end{bmatrix} = \begin{bmatrix} 1/2 & 1/2\cot(\theta/2) & 1 \\ -1/2\cot(\theta/2) & 1/2 & 0 \end{bmatrix},$$

and the primitive vectors are

$$\mathbf{x}_1^{(O)} = 1/2, -1/2\cot(\theta/2) \tag{13.24a}$$

$$\mathbf{x}_2^{(O)} = 1/2\cot(\theta/2), 1/2. \tag{13.24b}$$

Note that $\mathbf{x}_1^{(O)}$ and $\mathbf{x}_2^{(O)}$ are continuous functions of θ and that, when θ is small, Eqs. (13.24) reduce to the result given by Frank's formula in Eqs. (13.2) and (13.12); that is, the dislocation spacing D is given by b (unity in this case) divided by θ. Also notice that there are particular values where the $\cot(\theta/2)$ in Eqs. (13.24) are rational, for example, when $\cot(\theta/2) =$ integer. This situation was illustrated previously in Figure 13.5 where $\cot(\theta/2) = 14$. Whenever the $\cot(\theta/2) = 2n$ for both $\mathbf{x}_1^{(O)}$ and $\mathbf{x}_2^{(O)}$ (i.e., it is even for both), the O-point has integral coordinates and is thus a crystal lattice site. When either or both of the O-points are odd, the O-point is either in the center of an edge or in the center of a crystal cell. This illustrates the general result that points of the O-lattice need not coincide with crystal lattice sites.

In the derivation of Eq. (13.22), it was assumed that the points defined by the vectors $\mathbf{x}^{(O)}$ have identical internal coordinates in both lattices 1 and 2, and the $\mathbf{b}^{(L)}$ vectors are all lattice translation vectors. Physically, this means that the interface under consideration is comprised of perfect crystal dislocations. In the section that follows, we see that other dislocations with Burgers vectors that are less than a full lattice translation are possible at an interface. This does not mean that the O-lattice theory is incorrect but rather, that the choice of Burgers vectors at an interface is ambiguous and some additional criteria must be considered to determine the most favorable Burgers vectors at the interface. This is a weakness of the O-lattice theory in terms of its predictive capabilities. Another shortcoming is that the theory can be used to analyze an interface if $\mathbf{A}$ and $\mathbf{n}$ and/or the dislocation Burgers vectors $\mathbf{b}^{(L)}$ are known, but it cannot be used to predict $\mathbf{n}$ or $\mathbf{b}^{(L)}$ without knowing $\mathbf{A}$ and using some other criteria.

The physical interpretation of the O-lattice in terms of grain boundaries is that the O-points in Eq. (13.22) are points of geometric registry (minimum strain) between crystal lattices 1 and 2. Between each of these O-points, there is an accumulating disregistry that reaches the value $\mathbf{b}^{(L)}$ at a neighboring O-point. Thus, it is imagined that the misfit between any set of O-points is concentrated onto planes between the O-points just as the misfit between two identical but slightly rotated lattices relaxes into a low-angle boundary network of dislocations, as in Figure 13.10. In the example above, where the axis of rotation was parallel to [001] in the two lattices, the O-lattice construction yields O-lines parallel to the rotation axis with two orthogonal planes of dislocations bisecting the space between the O-lines as illustrated in Figure 13.17. Note that a plane taken perpendicular to the O-lines in this figure would look exactly like Figure 13.10. In the case of a general grain or interphase boundary, the set of planes on which misfit is condensed defines a three-dimensional cell structure with each cell enclosing an O-point. Consequently, wherever the interface plane cuts a cell wall there is a dislocation with Burgers vector $\mathbf{b}^{(L)}$.

Although this section is primarily concerned with the structure of grain boundaries and therefore a rotation $\mathbf{R}$ between two crystals, it is convenient to illustrate the use of the O-lattice theory for a different kind of transformation tensor $\mathbf{A}$, in which there is a simple dilatation $\Delta\alpha$ between two simple cubic crystal lattices. This also serves to emphasize the generality of the O-lattice formulation to other types of transformations. We see a second example of the O-lattice applied to a rotation between two crystals in the next section. The dot patterns included as Appendix D can be used to duplicate these and other examples.

Figure 13.18a shows schematically, a (001) projection of the O-lattice between two simple cubic lattices with the same orientation but different lattice parameters, where crystals 1 and 2 are represented by dots and crosses, respectively, and the O-points are circled. The two lattices are related by a simple dilatation $\Delta\alpha$ and inspection shows that the O-lattice itself is a simple cubic lattice. The $\mathbf{b}^{(L)}$ vectors lie between the O-points, that are indicated by circles in the figures. The dislocation spacing in the O-lattice is given as $(1 + \Delta\alpha)/\Delta\alpha$, which is equivalent to the inverse

---

Figure 13.17. Schemat
with the O-lattice of twc

of the misfit δ in Eq.
tice vectors perpendi
around the O-lattice
is chosen so that it p
mize the amount of g
above the interface p
face plane downward
points are regions of
ation of the interfac
crossed). This illustr
ically using the basic

13.2.3. Coinciden

The previous O-latt
nique for analyzing p
space when their or

l. This illustrates the
h crystal lattice sites.
points defined by the
1 and 2, and the $\mathbf{b}^{(L)}$
ns that the interface
s. In the section that
at are less than a full
ean that the O-lattice
ors at an interface is
determine the most
f the O-lattice theory
hat the theory can be
Burgers vectors $\mathbf{b}^{(L)}$
nowing **A** and using

grain boundaries is
ry (minimum strain)
nts, there is an accu-
g O-point. Thus, it is
rated onto planes be-
t slightly rotated lat-
s, as in Figure 13.10.
[001] in the two lat-
otation axis with two
the O-lines as illus-
to the O-lines in this
eneral grain or inter-
d defines a three-di-
onsequently, wherev-
Burgers vector $\mathbf{b}^{(L)}$.
e structure of grain
s convenient to illus-
sformation tensor **A**,
cubic crystal lattices.
formulation to other
tice applied to a rota-
ncluded as Appendix

of the O-lattice be-
different lattice para-
ses, respectively, and
ole dilatation Δa and
tice. The $\mathbf{b}^{(L)}$ vectors
ures. The dislocation
ivalent to the inverse

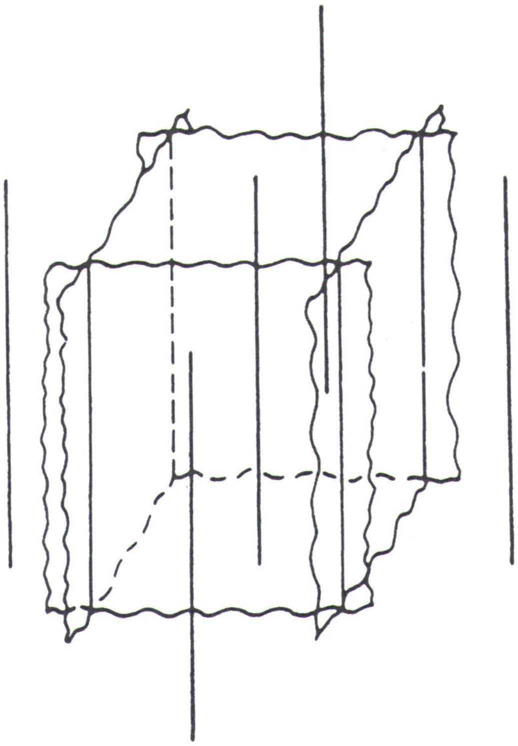

Figure 13.17. Schematic representation of the O-lines and dislocation cell walls associated with the O-lattice of two simple cubic lattices rotated about a common [001] axis. From [42].

of the misfit δ in Eq. (13.18). Figure 13.18b shows the planes that bisect the O-lattice vectors perpendicular to the plane of the figure. These form square cell walls around the O-lattice points in three dimensions. In Figure 13.18c an interface path is chosen so that it passes through as many O-points as possible in order to maximize the amount of good matching in the interface. When crystal 1 is removed from above the interface plane in Figure 13.18c and crystal 2 is removed from the interface plane downward, the interface in Figure 13.18d results. In this interface, the O-points are regions of good matching and these are separated by regions where relaxation of the interface into dislocations has occurred (where the cell walls were crossed). This illustrates the O-lattice construction, which can be performed analytically using the basic O-lattice equation (Eq. 13.22).

13.2.3. Coincident Site and Displacement Shift Complete Lattices

The previous O-lattice theory provides us with a convenient mathematical technique for analyzing possible dislocation structures between two arbitrary lattices in space when their orientation relationship is known. It is a useful technique, but it

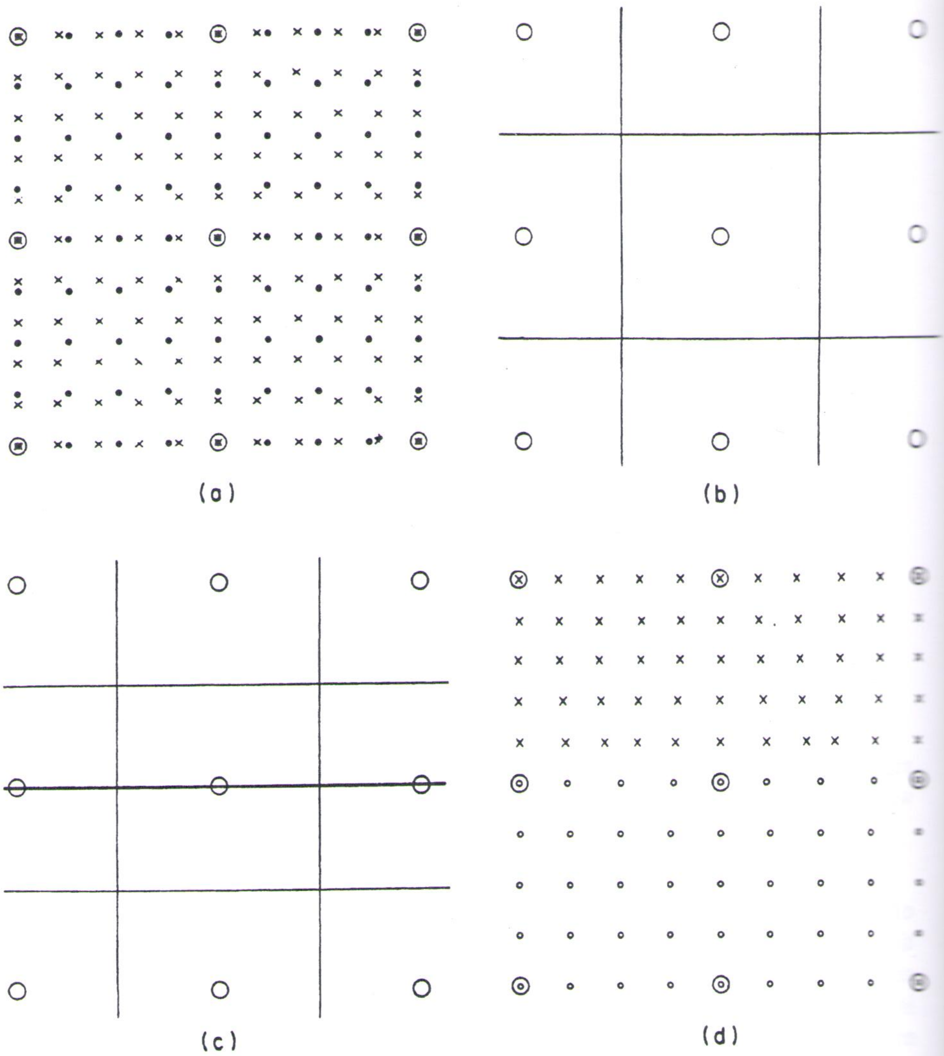

Figure 13.18. Illustration of the O-lattice construction for a dilatation between two simple cubic lattices: (a) (001) projection of the O-lattice, (b) cells walls drawn midway between the O-points, (c) interface path through highest density of O-points, and (d) section showing dislocations at the interface. From [42].

has limitations in that it cannot predict certain aspects of interfacial structure that are commonly found at interfaces, such as ledges and partial dislocation structures. In addition, as with the Read and Shockley analysis, its meaning becomes unclear in the case of high-angle grain boundaries. An alternate technique for quantifying the interfacial structure of grain and interphase boundaries for any angle of tilt or orientation is provided by the coincident site lattice (CSL) and displacement shift com-

---

plete (DSC) lattice co
actually developed be
this chapter because c
tent of a grain bounda
construction for grain
tion, and then show
clude heterophase int

Coincident Site L
that when two identic
around a lattice point
other than the origin
Figure 13.19a, in wh
the other by open cir
The two lattices have
the figure, as in Figu
dichromatic pattern.
coincident with the [3
the lattice points of t
and b.c.c. lattices as w
coincident site lattice
ure 13.19b. The lattic

The CSL is ch
natively expressed as
original lattice. For t
every ten atoms (i.e.,
cident. Any rational <
shown [46] that all p
tion

where x and y are non
lattice point joined to
for a rotation of 180°
mined from Eq. (13.2
sults. For example, a
generate the same Σ

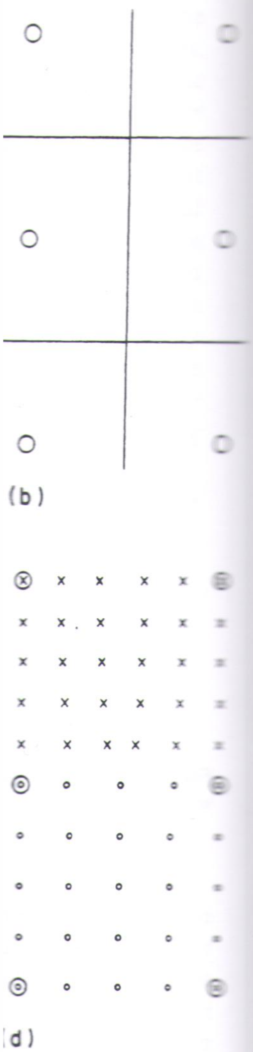

etween two simple cu-
idway between the O-
ction showing disloca-

facial structure that
slocation structures.
becomes unclear in
for quantifying the
ngle of tilt or orien-
acement shift com-

---

plete (DSC) lattice constructions provided in this section. The CSL/DSC theory was actually developed before O-lattice theory, but the O-lattice was introduced first in this chapter because of its close relation to Frank's equation for the dislocation content of a grain boundary in Section 13.2.1. In this section, we develop the CSL/DSC construction for grain boundaries using a pure tilt boundary for purposes of illustration, and then show that the CSL/DSC framework can be readily extended to include heterophase interfaces as well.

Coincident Site Lattice We have seen previously in Figures 13.5 and 13.11 that when two identical interpenetrating lattices are rotated from initial coincidence around a lattice point, there are certain discrete rotation angles where lattice points other than the origin coincide. An example often found in the literature is shown in Figure 13.19a, in which two simple cubic lattices, one indicated by solid dots and the other by open circles, are outlined by a dashed and solid square, respectively. The two lattices have been rotated 36.9° about an axis perpendicular to the plane of the figure, as in Figure 13.11, and the pattern that results is often referred to as the dichromatic pattern. In this case $\cot(\theta/2) = 3$ and the [310] vector in one lattice is coincident with the $[3\bar{1}0]$ vector in the other lattice. This rotation causes one-fifth of the lattice points of the simple cubic crystal to coincide, and this is true for f.c.c. and b.c.c. lattices as well. The coincident points themselves form a lattice, called the coincident site lattice (CSL), which is indicated by filled circles and outlined in Figure 13.19b. The lattice vectors of the CSL are given as

$$1/2[310]_1 \| 1/2[3\bar{1}0]_2,$$

$$1/2[\bar{1}30]_1 \| 1/2[130]_2 \text{ and}$$

$$1/2[12\bar{1}]_1 \| 1/2[21\bar{1}]_2.$$

The CSL is characterized by Σ, the inverse density of coincident sites, alternatively expressed as the ratio of the area of the coincident lattice cell to that of the original lattice. For the example shown in Figure 13.19, $\Sigma = 5$, because two out of every ten atoms (i.e., the corner atoms) in each unit cell of the CSL lattice are coincident. Any rational <*uvw*> lattice vector can be used to generate a CSL; it has been shown [46] that all possible CSLs in the cubic system can be described by the function

$$\Sigma = x^2 + Ny^2, \tag{13.25}$$

where x and y are nonnegative integers representing the Cartesian coordinates of the lattice point joined to the origin, and $N = u^2 + v^2 + w^2$. A CSL is always generated for a rotation of 180° about a rational direction <*uvw*>. When the value of Σ determined from Eq. (13.25) is even, it must be divided by two until an odd number results. For example, a <310> vector where $\Sigma = 10$ and a <210> vector where $\Sigma = 5$ generate the same $\Sigma = 5$ CSL, shown in Figure 13.19b. Thus the $\Sigma = 10$ CSL must

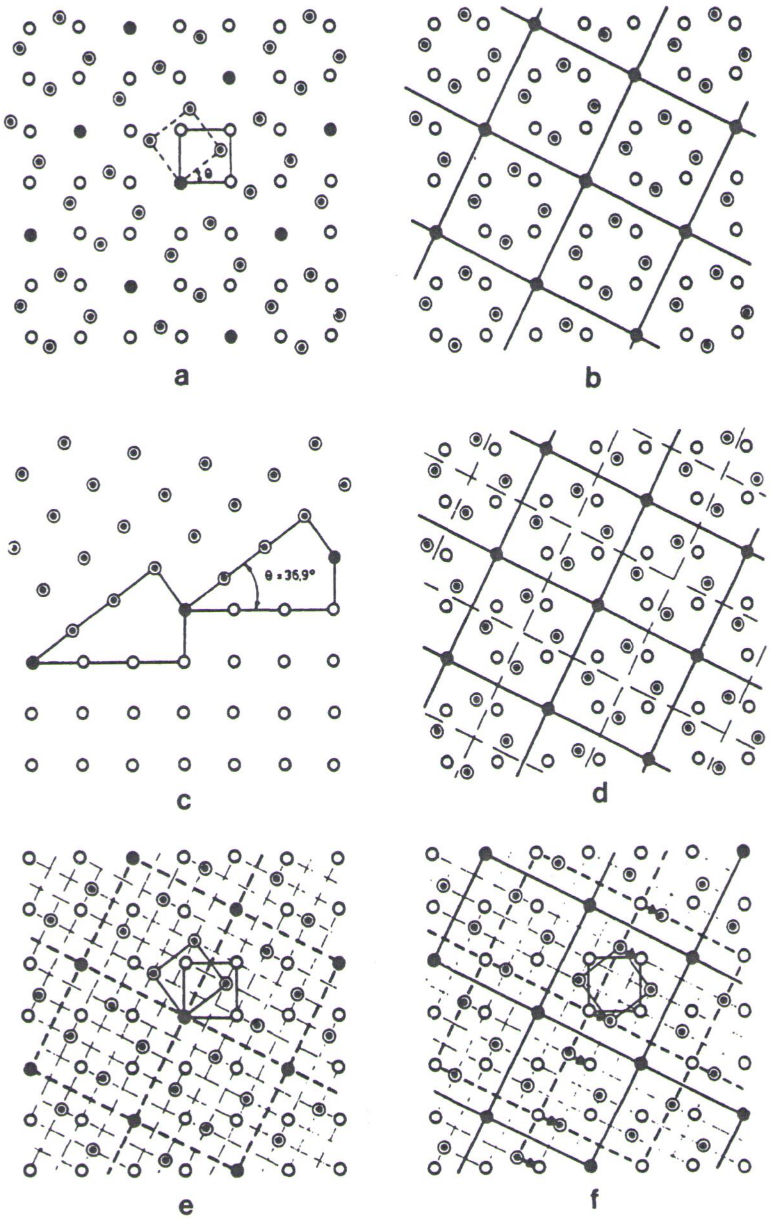

Figure 13.19. (a) Dichromatic pattern produced by rotating two cubic crystals 36.9° about [001]. (b) $\Sigma = 5$ CSL outlined in the dichromatic pattern. (c) A possible $(130)_1$, $(130)_2$ grain boundary generated from the CSL. (d) The O-lattice (= CSL plus the dashed lines). (e) The DSC lattice of the $\Sigma = 5$ dichromatic pattern. (f) The dichromatic pattern after translation by a DSC vector; dashed lines indicate old CSL and solid lines indicate new CSL. From [45].

be divided by
tion correspo

where θ = 18
in a cubic sys
even.

Becaus
sets of x, y an
beling them
boundaries in
Eq. (13.25) a
specified in
inclination of
plane in both
13.6b). For th
tion is $\Sigma =$
boundary is
dence bounda

In Figu
types were d
composed of
ty of coincide
tals, the dens
boundary pla
of coincident
the energy of
some special
between the t
this lack of c
occur at grain
cannot be pre

Figure
rical tilt grain
dark spots in
evident as pr
there is a lack
present in the
tion of the bo
in Section 13
from accurate
stand the cor
aries, it has b
in Section 13

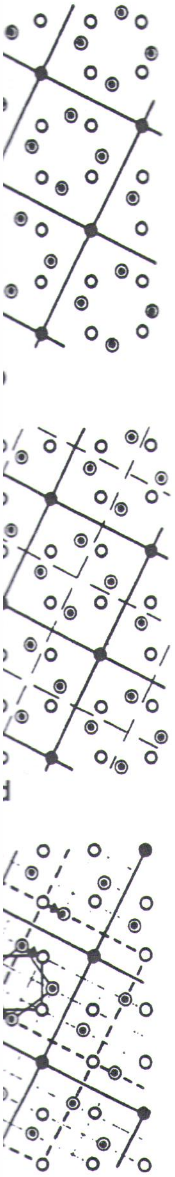

c crystals 36.9° about
ble $(130)_1$, $(130)_2$ grain
dashed lines). (e) The
n after translation by a
CSL. From [45].

be divided by two to yield the $\Sigma = 5$ CSL in Figure 13.19b. The angle of misorientation corresponding to a particular CSL is given by

$$\theta = 2\tan^{-1}(y/x)N^{1/2}, \tag{13.26}$$

where $\theta = 180°$ corresponds to $x = 0, y = 1$. Thus, the rotation of 180° around <*uvw*> in a cubic system gives rise to a CSL of $\Sigma = u^2 + v^2 + w^2$ if N is odd or $N/2$ if N is even.

Because the same values of Σ may be generated by Eq. (13.25) from different sets of x, y and N, different CSLs that yield the same values are distinguished by labeling them a, b, c, and so on. The corresponding axis–angle pairs for coincidence boundaries in the cubic system for Σ values ranging from 1 to 19 calculated from Eq. (13.25) are shown in Table 13.2. Usually, both Σ and the axis–angle pair are specified in CSL nomenclature, that is, $\Sigma = 5$, 36.9°/[001] for Figure 13.19b. The inclination of the boundary is then specified by the Miller indices of the boundary plane in both lattices, that is, $(hkl)_1(hkl)_2$, similar to the DOF specified in Eq. 13.6b). For the symmetric tilt boundary in Figure 13.19c, the complete CSL notation is $\Sigma = 5$ (310) 36.9°/[001], where only one (*hkl*) is necessary, because the boundary is symmetric. The values of θ in Table 13.2 correspond to ideal coincidence boundaries. A more extended tabulation is given by Mykura [47].

In Figure 13.19c a (310) boundary plane was chosen, and opposite lattice types were discarded from either side of the boundary, leaving a grain boundary composed of typical structural units, as indicated in the figure. Although the density of coincident sites depends only on the orientation relationship between two crystals, the density of coincident sites at a boundary depends on the choice of the boundary plane intersecting the CSL. Special grain boundaries have a high density of coincident sites and therefore a low value of Σ. It seems reasonable to expect that the energy of a grain boundary should be proportional to Σ, but except in the case of some special grain boundaries, it has been shown that there is no simple correlation between the two. This is a disappointment of the CSL theory, but we now know that this lack of correlation is from volume expansions and translations that frequently occur at grain boundaries to minimize the energy of the boundary. Such relaxations cannot be predicted from simple geometric theories.

Figure 13.20 shows an HRTEM image of a $\Sigma = 5$ (310) 36.9°/[001] symmetrical tilt grain boundary in cubic nickel oxide [48]. The atomic columns appear as dark spots in this image and a regular pattern of structural units at the boundary is evident as predicted by the CSL construction in Figure 13.19c. However, note that there is a lack of mirror symmetry across the boundary in the HRTEM image that is present in the unrelaxed CSL model in Figure 13.19c. This is due to a slight translation of the boundary involving the three microscopic degrees of freedom discussed in Section 13.2.1, and it is such translations that limit the hard-sphere CSL model from accurately describing the energies of grain boundaries. Thus, to fully understand the correlation between the structure and energy of high-angle grain boundaries, it has been necessary to employ extensive atomistic calculation, as described in Section 13.2.4. The CSL theory does provide a simple and useful geometric mod-

Table 13.2. Some axis-angle pairs for CSL boundaries in the cubic lattice system

Θ^0	Σ
<100> Axis	
22.62	13a
28.07	17a
36.87	5
53.13	5
61.93	17a
67.38	13a
112.62	13a
118.07	17a
126.87	5
143.13	5
151.93	17a
157.38	13a
<110> Axis	
26.53	19a
38.94	9
50.48	11
70.53	3
86.63	17b
93.37	17b
109.47	3
129.52	11
141.06	9
153.47	19a
<111> Axis	
27.80	13b
38.21	7
46.83	19b
60.00	3
73.17	19b
81.79	7
92.20	13b
147.80	13b
158.21	7
166.83	19b
180.00	3
<210> Axis	
48.19	15
73.40	7
96.38	9
131.81	3
180.00	5
<211> Axis	
62.96	11
78.46	15
101.54	5
135.58	7
180.00	3
<221> Axis	
61.93	17b
90.00	9
112.62	13b
143.13	5
180.00	9
<310> Axis	
76.66	13b
93.02	19a
115.38	7
144.90	11
180.00	5
<311> Axis	
50.70	15
67-11	9
95.74	5
117.82	15
146.44	3
180.00	11
<320> Axis	
71.59	19b
100.48	11
121.97	17b
149.00	7
180.00	13a
<321> Axis	
86.18	15
123.75	9
150.07	15
180.00	7
<322> Axis	
107.92	13a
152.73	9
180.00	17b
<331> Axis	
63.82	17b
82.16	11
110.92	7
154.16	5
180.00	19a
<332> Axis	
99.08	19a
133.81	13a
180.00	11
<410> Axis	
107.92	13b
152.73	9
180.00	17a
<411> Axis	
93.37	17a
129.52	11
153.47	19b
180.00	9
<421 > Axis	
113.58	15
155.38	11
<430> Axis	
118.07	17b
157.38	13b
<431> Axis	
137.17	15
180.00	13b
<432> Axis	
121.76	19a
158.96	15
<433> Axis	
142.14	19a
180.00	17b
<441> Axis	
160.25	17a
<510> Axis	
137.17	15
180.00	13a
<511> Axis	
73.17	19a
92.20	13a
120.00	9
158.21	7
<520> Axis	
121.76	19b
158.96	15
<521> Axis	
139.88	17b
180.00	15
<522> Axis	
160.25	17b
<530> Axis	
142.14	19b
180.00	17a
<531> Axis	
99.59	15
126.22	11
160.81	9
<532> Axis	
180.00	19b
<533> Axis	
105.35	17a
130.83	13b
162.66	11
<551> Axis	
110.01	19b
134.43	15
164.06	13a
<553> Axis	
137.33	17a
165.16	15
<610> Axis	
161.33	19a
161.33	19a
<611> Axis	
180.00	19a
<711> Axis	
110.01	19a
134.43	15
164.06	13b
<731> Axis	
137.33	17b
165.16	15
<733> Axis	
139.74	19b
<751> Axis	
166.83	19a

Source: Data from [24] and [47].

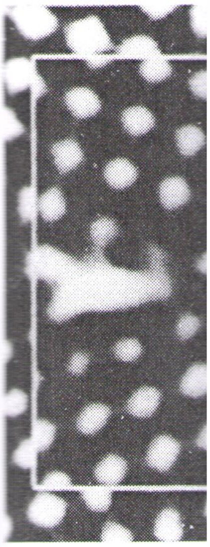

Figure 13.20. HR
<001> tilt-axis. A
the boundary, wh
from Argonne Nat

el for understan
ing between two
has been used e
terfaces with co
Any lattic
13.22) because
two lattices am
$\mathbf{x}^{(O)}$ are CSL vec
boundary shown
not exactly equ
center of rotatio
vectors $\mathbf{x}^{(O)}$, wh
Thus, the O-latti

Displacement
boundaries can
similar to low-a
gle crystal (i.e.,
tion from a CSL
between regions
dislocations are

attice system

Θ^0	Σ
<522>	Axis
160.25	17b
<530>	Axis
142.14	19b
180.00	17a
<531>	Axis
99.59	15
126.22	11
160.81	9
<532>	Axis
180.00	19b
<533>	Axis
105.35	17a
130.83	13b
162.66	11
<551>	Axis
110.01	19b
134.43	15
164.06	13a
<553>	Axis
137.33	17a
165.16	15
<610>	Axis
161.33	19a
161.33	19a
<611>	Axis
180.00	19a
<711>	Axis
110.01	19a
134.43	15
164.06	13b
<731>	Axis
137.33	17b
165.16	15
<733>	Axis
139.74	19b
<751>	Axis
166.83	19a

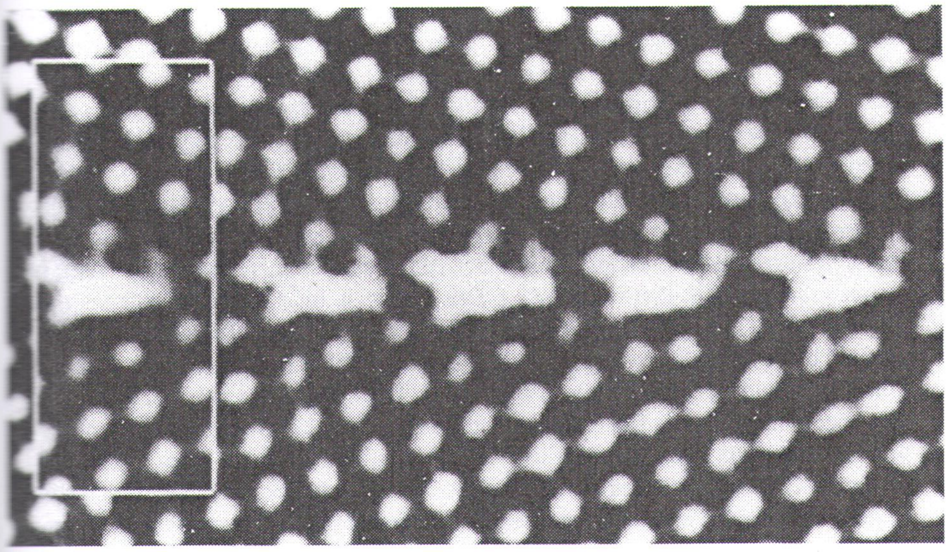

Figure 13.20. HRTEM image of a $\Sigma = 5$ grain boundary in nickel oxide viewed parallel to the <001> tilt-axis. A digitally averaged image in the inset shows a representative structural unit of the boundary, which is slightly asymmetrical. Reprinted from [48] with additional permission from Argonne National Laboratory.

el for understanding interfacial structure in terms of atom matching and mismatching between two crystals across the interface for any degree of misorientation, and it has been used extensively in describing the dislocation structure of solid–solid interfaces with considerable success.

Any lattice vectors of the CSL are solutions $\mathbf{x}^{(O)}$ of the O-lattice equation (Eq. 13.22) because at each independent site the rotational displacements between the two lattices amount to a lattice translation $\mathbf{b}^{(L)}$. However, not all O-lattice vectors $\mathbf{x}^{(O)}$ are CSL vectors. This point is illustrated by the complete O-lattice for the $\Sigma = 5$ boundary shown in Figure 13.19d. When the orientation between the two lattices is not exactly equal to that necessary for a CSL, all the coincident sites (except the center of rotation) are lost. In contrast, the O-lattice is still maintained with lattice vectors $\mathbf{x}^{(O)}$, which are now irrational although close to the rational CSL vectors. Thus, the O-lattice changes continuously between the discrete CSLs.

Displacement Shift Complete Lattice Geometrically, high-angle grain boundaries can be treated as small deviations from the nearest CSL. They are then similar to low-angle grain boundaries, where small deviations from the perfect single crystal (i.e., $\Sigma = 1$ CSL) are accommodated by lattice dislocations. Any deviation from a CSL is accommodated by lines of high local distortion or dislocations in between regions of undistorted CSL. In the case of low-angle grain boundaries, the dislocations are usually called primary dislocations and the boundary between them is perfect crystal ($\Sigma = 1$). In the case of high-angle grain boundaries, the dislocations are called secondary dislocations and the boundary between them is perfect CSL.

The displacement shift complete (DSC) lattice defines the possible Burgers vectors of secondary dislocations [49]. These are perfect grain boundary dislocations that conserve the structure of the optimal coincidence orientation boundary. The DSC lattice acquired its name because it is a lattice of pattern-conserving displacements (i.e., a displacement of one crystal with respect to the other by a DSC vector restores the dichromatic pattern but with shifted coincidence sites). Thus, it causes a pattern shift that is complete. This feature is illustrated with reference to the $\Sigma = 5$ CSL in Figures 13.19e and f. In Figure 13.19e, the DSC lattice was constructed by defining the coarsest lattice that contains all of the sites of crystals 1 and 2 in the coincidence orientation as sublattices. The DSC lattice is indicated by the fine square mesh in this figure. Note that the DSC lattice points are not all translationally equivalent in the surroundings of crystals 1 and 2. When lattice 1 is shifted by the DSC vector indicated by an arrow in Figure 13.19f, the dichromatic pattern of the lattices is restored, but the resulting CSL (solid line) is shifted from its original position (dashed line).

The utility of the DSC construction is that any misorientation from the perfect $\Sigma = 5$ CSL orientation can be accommodated by these secondary dislocations with areas of perfect $\Sigma = 5$ boundary in between. The secondary dislocations thus occur when the primary dislocations are so close that they are not physically separate. The DSC dislocations then accommodate the irregularity in the periodicity of the primary dislocations, similar to the situation previously illustrated in Figure 13.6 using only primary dislocations. The secondary grain boundary dislocations required to accommodate the small misorientation from the exact CSL can be described by an equation equivalent to Eq. (13.12a) for low-angle boundaries, or

$$\mathbf{B}_s = (\mathbf{x} \times \mathbf{q})\, 2 \sin(\theta_{CSL}/2), \tag{13.27}$$

where $\mathbf{B}_s$ is the net Burgers vector content of the secondary grain boundary dislocations intercepted by any vector $\mathbf{x}$ lying in the plane of the boundary, and θ_{CSL} is the angular departure from the exact CSL orientation about an axis $\mathbf{q}$ common to one of the grains and the CSL. An important property of Eq. (13.27) is that it does not suffer from the ambiguity in the uniqueness of the Burgers vectors discussed for Eq. (13.12a). Equation (13.27) gives a unique value for the net Burgers vector $\mathbf{B}_s$ of the secondary grain boundary dislocation network because it is a property of the intersection of the translational symmetry elements of the two crystals and this is unique.

Formally, the DSC lattice can be defined as the lattice of difference vectors (i.e., vectors linking the lattice sites of crystal 1 to crystal 2), between lattices 1 and 2 in the exact coincidence orientation. Analytically, this can be expressed as

$$\mathbf{d}^{(DSC)} = \mathbf{x}^{(2)} - \mathbf{x}^{(1)} = (\mathbf{I} - \mathbf{A}^{-1})\mathbf{x}^{(2)}, \tag{13.28}$$

---

where $\mathbf{d}^{(DSC)}$ is a DS
as in Eqs. (13.21) an
the DSC lattice for t
formed by the recipr
[50]. The reciprocal r
creases the primitive
solved graphically if
orientation and posit
13.19e. In this case, t

Otherwise, the DSC

Schober and B
imental evidence for
that secondary grain
orientations. Their or
tained in subsequent
shows the variation i
secondary grain bou
boundary dislocation
each of the exact CSI
mary dislocations in

where $\mathbf{b}_{si}$ is the Burg
Burgers vectors that
that were compatible
near Σ = 5, Σ = 13 a
ondary grain bounda
1/34<530>, respectiv
Burgers vectors were
the interfaces, as illus
tions due to their sma

It is important t
coincidence orientati
across any grain (or i
on which Burgers cir
ous defects, such as l
method to quantify th

where $\mathbf{d}^{(DSC)}$ is a DSC lattice vector and the other symbols have the same meaning as in Eqs. (13.21) and (13.22). Another way of finding DSC vectors is to note that the DSC lattice for two direct lattices 1 and 2 is the reciprocal lattice of the CSL formed by the reciprocal lattices of 1 and 2 for the same axis and angle of rotation [50]. The reciprocal relation between the CSL and DSC lattices means that as Σ increases the primitive DSC vectors decrease in magnitude. Equation (13.28) can be solved graphically if Σ is not too high by drawing the two lattices in the coincidence orientation and position and finding the DSC vectors by inspection, as in Figure 13.19e. In this case, the lattice vectors of the DSC lattice are given as

$$1/10[310]_1,$$

$$1/10[\bar{1}30]_1 \text{ and}$$

$$1/10[21\bar{5}]_1.$$

Otherwise, the DSC vectors must be found analytically.

Schober and Balluffi [34] were the first investigators to provide strong experimental evidence for the CSL model of grain boundary structure by demonstrating that secondary grain boundary dislocations accommodated departures from CSL orientations. Their original results on twist boundaries in gold as well as those obtained in subsequent investigations are summarized in Figure 13.21. This figure shows the variation in dislocation spacing with twist angle θ for both primary and secondary grain boundary dislocations. The spacing D_{si} of the secondary grain boundary dislocations in the crossed grids varied with angular departure θ_{CSL} from each of the exact CSL orientations according to the same relationship given for primary dislocations in Eq. (13.2b), or

$$D_{si} = |\mathbf{b}_{si}|/\theta_{CSL}, \tag{13.29}$$

where $\mathbf{b}_{si}$ is the Burgers vector of the ith secondary grain boundary dislocation. The Burgers vectors that were found to satisfy Eq. (13.29) were the basis DSC vectors that were compatible with the line directions of the screw dislocations. Thus, for the near $\Sigma = 5$, $\Sigma = 13$ and $\Sigma = 17$ boundaries, the Burgers vectors found for the secondary grain boundary dislocations were of the type 1/10<310>, 1/26<510> and 1/34<530>, respectively. In addition, for the case of the near $\Sigma = 5$ boundaries, the Burgers vectors were found to agree with the contrast observed in TEM images of the interfaces, as illustrated in Figure 13.22. Note the weak contrast of the dislocations due to their small Burgers vectors as compared to Figure 13.12a.

It is important to note that the DSC lattice contains both lattices 1 and 2 in the coincidence orientation and position as sublattices. Therefore, it is continuous across any grain (or interphase) boundary and provides a suitable reference lattice on which Burgers circuits may be drawn [52]. This is an important point since various defects, such as ledges, occur at grain and interphase boundaries, and we need a method to quantify the nature of these defects. Thus, we now examine the character

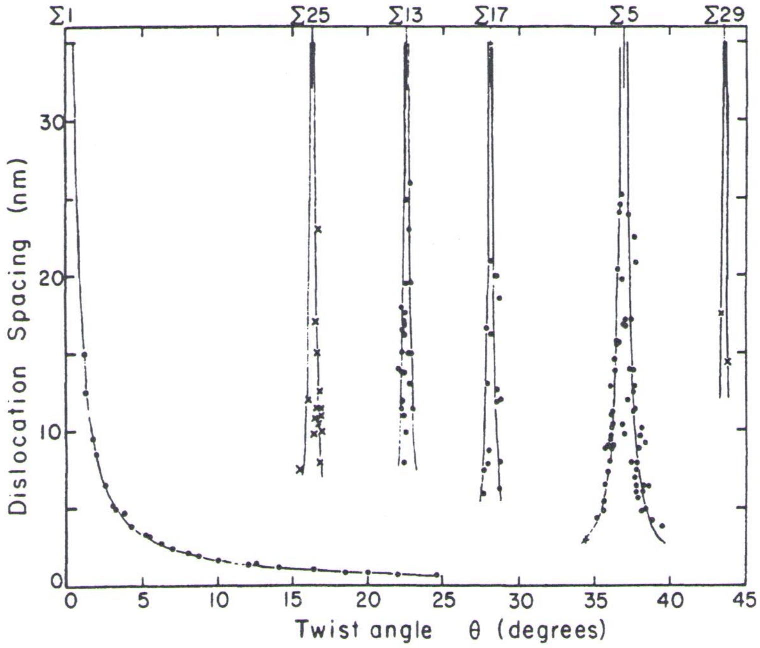

Figure 13.21. Variation of dislocation spacing with twist angle for primary and secondary grain boundary dislocations in gold. From [33] and [34,51] copyright Taylor & Francis Ltd.

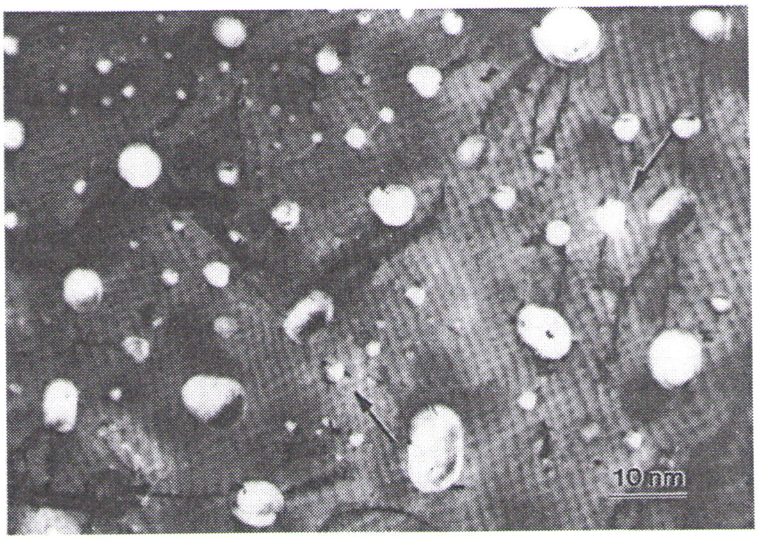

Figure 13.22. TEM image showing a cross-grid of secondary grain boundary dislocations in a near $\Sigma = 5$ (001) twist boundary in gold. From [34] copyright Taylor & Francis Ltd.

---

of ledges in gra
followed by exte

Structure anc
fects The top
als is readily est
general type of l
be defined by th
"step" is often u
indicate its simi
fects therefore i
ones which are
may be classifie
boundary struct
the equilibrium
If the disl
dislocation, ther
composed of al
conserve the at
shift in space of
spect to lattice 1
crystal lattices
these line defec
ing the example
In Figure
the DSC lattice
Burgers vector
Burgers circuit
and Balluffi [52

The heights of
given by $\mathbf{s}_1 \cdot \mathbf{n}$
normal to the b
13.23, $\mathbf{s}_1 \cdot \mathbf{n} = \mathbf{s}$
relaxed boundar
tive ledge heigh
A line de
the special cas
Figure 13.23, w
is a pure grain l
cial case when
cation lying in
Figure 13.23, p

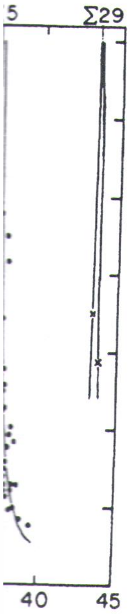

ary and secondary
r & Francis Ltd.

y dislocations in a
s Ltd.

of ledges in grain boundaries using the DSC lattice as our reference lattice. This is followed by extension of the CSL/DSC construction to interphase boundaries.

Structure and Properties of Grain and Interphase Boundary Line Defects The topology of line defects that exist in grain boundaries in cubic materials is readily established within the framework of the DSC model [52,53]. The most general type of line defects possess both dislocation and ledge character, which can be defined by the Burgers vector **b** and the ledge vector **s**, respectively. (The term "step" is often used instead of "ledge" in the literature, but we use the term ledge to indicate its similarity with the ledges discussed in Parts II and III.) Possible line defects therefore include those with both dislocation and ledge character and special ones which are either pure dislocations or pure ledges. In addition, the line defects may be classified as intrinsic when they represent an integral part of the equilibrium boundary structure and extrinsic when they represent extra defects superimposed on the equilibrium structure. We mainly consider intrinsic defects.

If the dislocation character of a line defect is that of a perfect grain boundary dislocation, then the Burgers vector must be that of the DSC lattice, because this is composed of all lattice translation vectors of lattice 2 with respect to lattice 1 that conserve the atomic (dichromatic) pattern. The ledge vector then corresponds to a shift in space of the above pattern, which occurs when lattice 2 is translated with respect to lattice 1 by the Burgers vector. These ledge vectors are always vectors of the crystal lattices and therefore also of the DSC lattice. The topological properties of these line defects in grain boundaries can be revealed with the DSC framework using the examples shown in Figure 13.23.

In Figure 13.23, the Burgers vector of the dislocation is seen to be a vector of the DSC lattice as are ledge vectors $\mathbf{s}_1$ and $\mathbf{s}_2$ in lattices 1 and 2, respectively. The Burgers vector of the defect on the left can be readily obtained by constructing a Burgers circuit using the DSC lattice as the reference lattice as described by Hirth and Balluffi [52]. The Burgers vector and ledge vectors are related by

$$\mathbf{b} = \mathbf{s}_1 - \mathbf{s}_2. \qquad (13.30)$$

The heights of the ledges in the boundary plane (with their appropriate signs) are given by $\mathbf{s}_1 \cdot \mathbf{n}$ and $\mathbf{s}_2 \cdot \mathbf{n}$ for lattices 1 and 2, respectively, where **n** is a unit vector normal to the boundary plane and pointing from crystal 1 into crystal 2. In Figure 13.23, $\mathbf{s}_1 \cdot \mathbf{n} = \mathbf{s}_2 \cdot \mathbf{n}$ and the effective ledge height produced by the line defect in the relaxed boundary structure is given by $\mathbf{s}_1 \cdot \mathbf{n} = \mathbf{s}_2 \cdot \mathbf{n}$. When $\mathbf{s}_1 \cdot \mathbf{n} \neq \mathbf{s}_2 \cdot \mathbf{n}$, the effective ledge height may be taken as $1/2(\mathbf{s}_1 + \mathbf{s}_2) \cdot \mathbf{n}$.

A line defect that is a pure ledge without dislocation character is obtained in the special case when $\mathbf{s}_1 - \mathbf{s}_2 = \mathbf{b} = 0$. An example is the pure ledge at *AB* in Figure 13.23, where $\mathbf{s}_1 = \mathbf{s}_2$ is a vector of the CSL. Conversely, a line defect that is a pure grain boundary dislocation without ledge character is obtained in the special case when $\mathbf{s}_1 \cdot \mathbf{n} = \mathbf{s}_2 \cdot \mathbf{n} = 0$. An example would be a grain boundary dislocation lying in a boundary plane parallel to the VWUT plane of the CSL shown in Figure 13.23, possessing the same Burgers vector **b** as the dislocation shown at *C*.

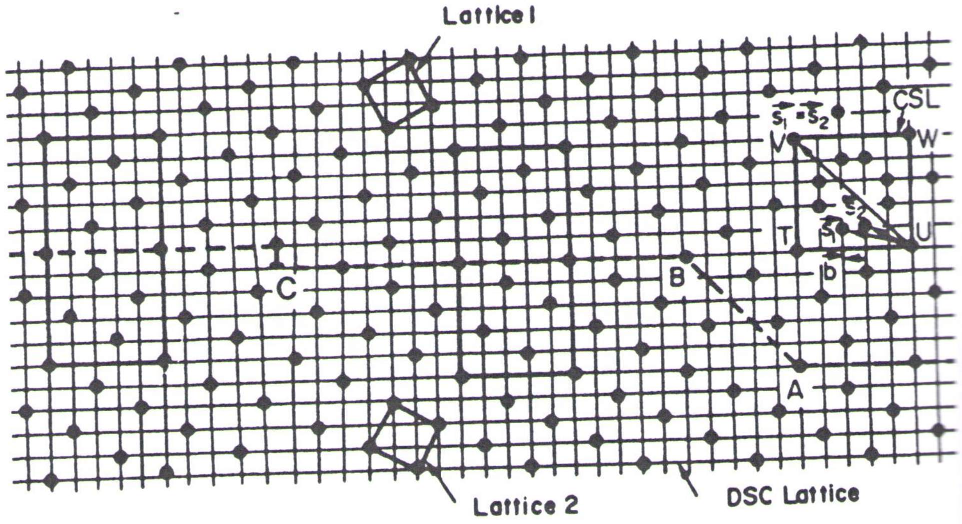

Figure 13.23. Line defects in a Σ = 5 symmetrical-tilt boundary produced by 36.9° rotation around [001]. A line defect possessing both dislocation and ledge character is shown on the left at *C* and a pure ledge is shown at *AB*. The Burgers vector and ledge vectors of the two line defects are shown in the diagram in the upper right. Reprinted with permission from [53] by Elsevier Science Ltd., Oxford, England.

These line defects possess a number of important topological properties summarized below.

1. Movement in the plane of the boundary of a line defect that possesses a dislocation character (which may require glide and climb) causes lattice 2 to translate with respect to lattice 1.
2. Movement of a line defect that possesses a ledge character causes the interface to translate with respect to lattices 1 and 2.
3. Climb of line defects possessing a dislocation character allow the boundary to act as a source or sink for point defects.
4. Lattice dislocations $\mathbf{b}^{(L)}$ that impinge on the boundary may dissociate into an integral number of grain boundary line defects $\mathbf{b}_i$ because the Burgers vectors of the lattice dislocations and the interfacial dislocations are all vectors of the DSC lattice and must obey the conservation relation $\mathbf{b}^{(L)} = n_i \mathbf{b}_i$, where n_i is the number of grain boundary dislocations of type *i*.
5. Lattice dislocations that cut through a boundary leave behind a line defect with dislocation character possessing a Burgers vector given by the DSC lattice.

The description of line defects in a grain boundary (homophase interface) by the DSC lattice can be readily extended to general heterophase interfaces. The de-

---

tails of this cons
the end results t
aries can be anal
aries above. This
of line defects at
Burgers vectors

Figures 1
interfaces betwe
be related by the
these figures ha
and M_2 in the fig
2, which almost
not always, subl
indicate the DSC
13.19e and 13.2

The line d
and ledge featur
cubic materials
and for the defe
These line defec
and a Burgers ve

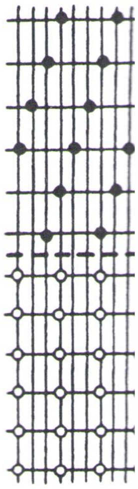

Figure 13.24. Th
which form a plan
O-lattice theory.
shown in the diag
Reprinted with pe

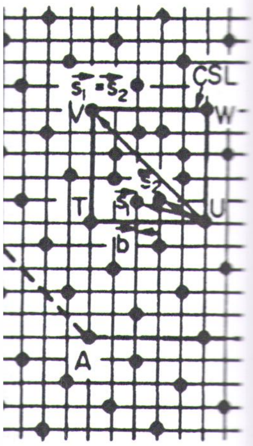

ced by 36.9° rotation
acter is shown on the
ge vectors of the two
permission from [53]

properties summa-

t possesses a dislo-
s lattice 2 to trans-

r causes the inter-

w the boundary to

dissociate into an
he Burgers vectors
e all vectors of the
= $n_i\mathbf{b}_i$, where n_i is

hind a line defect
n by the DSC lat-

hase interface) by
nterfaces. The de-

---

tails of this construction have been thoroughly discussed [53,54]. We examine only the end results to show that dislocations and ledges in general heterophase boundaries can be analyzed within the same DSC framework developed for grain boundaries above. This construction provides a convenient way to quantify the character of line defects at heterophase interfaces in much the same way that we quantify the Burgers vectors of lattice dislocations [39].

Figures 13.24 and 13.25 show semicoherent planar and inclined interphase interfaces between two lattices (phases), respectively. The lattices can be assumed to be related by the transformation matrix **A** in Eq. (13.18). The vectors **b**, $\mathbf{s}_1$ and $\mathbf{s}_2$ in these figures have the same meanings as in Figure 13.23. The cells indicated as M_1 and M_2 in the figures identify a pair of cells in the strain free lattices (phases) 1 and 2, which almost match each other in both size and shape. These cells are usually, but not always, sublattices of the respective crystal lattices. The fine lines in the figures indicate the DSC lattice formed from lattices 1 and 2 in the same way as in Figures 13.19e and 13.23.

The line defects in the general interfaces have basically the same dislocation and ledge features as their counterparts in the special case of grain boundaries in cubic materials discussed previously. The ledge vector **s** is defined in the same way and for the defects in the boundary illustrated in Figure 13.24, $\mathbf{s}_1 \cdot \mathbf{n} = \mathbf{s}_2 \cdot \mathbf{n} = 0$. These line defects are therefore interfacial dislocations without any ledge character and a Burgers vector **b** defined by the DSC lattice between M_1 and M_2. They are of-

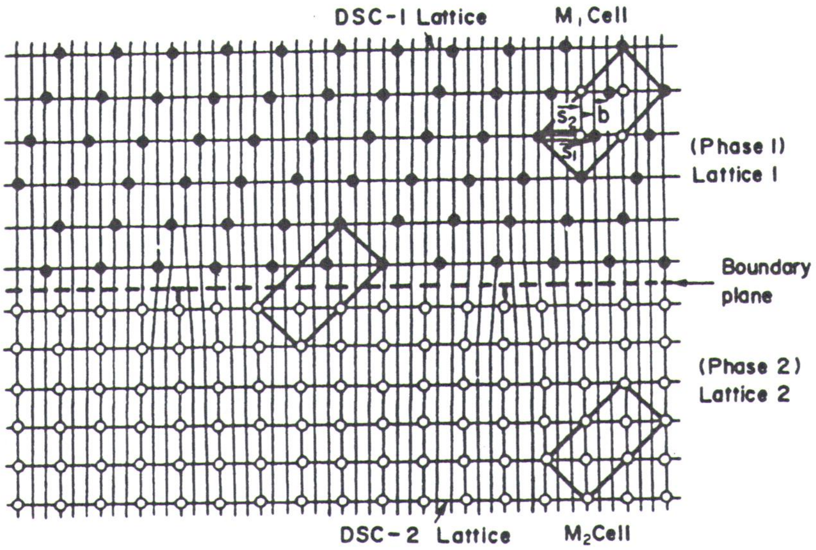

Figure 13.24. The interphase boundary between two different lattices (phases) M_1 and M_2, which form a planar interface containing interfacial dislocations with a spacing determined by O-lattice theory. The Burgers vector and ledge vectors of the interfacial dislocations are shown in the diagram in the upper right. The DSC lattice is indicated by fine lines in the figure. Reprinted with permission from [53] by Elsevier Science Ltd., Oxford, England.

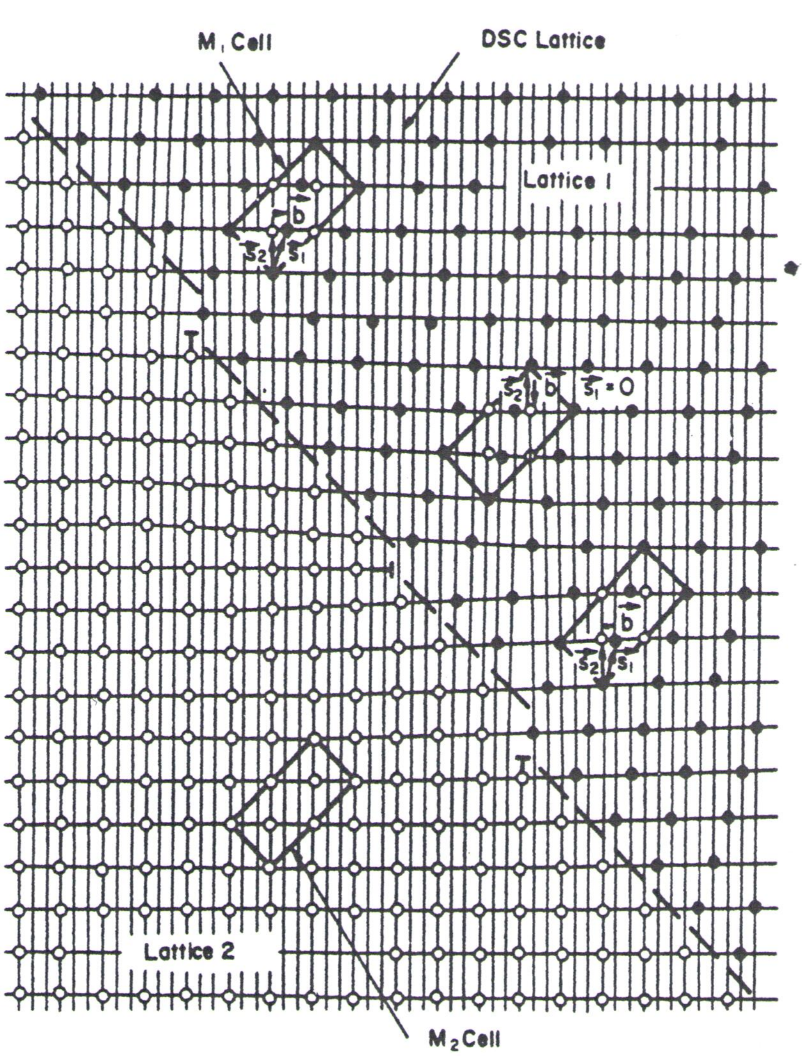

Figure 13.25. An interphase boundary between lattices 1 and 2 in Figure 13.24, but with the boundary plane at a different inclination. Two types of line defects are present possessing both dislocation and ledge character. The Burgers vectors and ledge vectors are illustrated in each case. Reprinted with permission from [53] by Elsevier Science Ltd., Oxford, England.

ten referred to as misfit dislocations, and this is a typical semicoherent interface [1] as illustrated previously in Figure 7.7 and Figure 12.5. In the general case, the line defects will have both dislocation and ledge character as seen in Figure 13.25, where a boundary is shown that differs from the boundary in Figure 13.24 only by a rotation of the interface plane. In this case, $\mathbf{s}_1 \cdot \mathbf{n} \neq \mathbf{s}_2 \cdot \mathbf{n} \neq 0$ for one type of line defect (indicated by ⊤) and $\mathbf{s}_1 = 0$ and $\mathbf{s}_1 \cdot \mathbf{n} \neq 0$ for the other (indicated by ⊣). A ledge is therefore evident at each defect. Note that unlike the atom positions around

---

the two dislocation
planes are complet
$\neq 0$. Such defects
[6] and diffusional
transformation disl
the interface. The l

It is also pos
tice dislocation cha
serted in the bound
$= \mathbf{s}_1 - \mathbf{s}_2 = 0$, althou
ed weak, long-rang
ation by other DSC
[53]. Because the l
same dislocation an
bic crystals, we exp
marized previously

In summary,
quantifying the vari
aries in materials. In
cal construction bas
shown here. The Bu
then be obtained dir
tion is difficult, the
tations of the DSC

Figure 13.26. Pure led
The ledge vectors are s
Science Ltd., Oxford, E

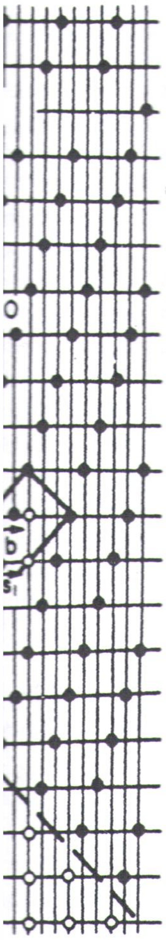

re 13.24, but with the
e present possessing
ctors are illustrated in
, Oxford, England.

herent interface [1]
neral case, the line
n in Figure 13.25,
ure 13.24 only by a
for one type of line
(indicated by ⊣). A
m positions around

---

the two dislocations in Figure 13.24 where a terminating plane is evident, the atom planes are completely coherent around the ledges (indicated by ⊤) for which $\mathbf{s}_1 \cdot \mathbf{n} \neq 0$. Such defects are commonly found at high-index interfaces in both martensitic [6] and diffusional [16] solid–solid transformations and are often referred to as transformation dislocations or structural ledges [1,55,56] depending on their role in the interface. The ledges in Figure 12.7 possess this type of defect character.

It is also possible to have pure interphase boundary ledges without DSC lattice dislocation character, as shown in Figure 13.26, where a pure ledge has been inserted in the boundary shown previously in Figure 13.24. In this case, $\mathbf{s}_1 = \mathbf{s}_2$ and $\mathbf{b} = \mathbf{s}_1 - \mathbf{s}_2 = 0$, although in the DSC lattice framework the ledge may have an associated weak, long-range stress field if isolated in the boundary without complete relaxation by other DSC lattice dislocations in the interface, as apparent in the figure [53]. Because the line defects in general interphase boundaries have basically the same dislocation and ledge features as their counterparts in grain boundaries in cubic crystals, we expect them to possess the same basic topological properties summarized previously for grain boundaries.

In summary, the DSC lattice framework is general and it provides a means of quantifying the various types of line defects found in grain and interphase boundaries in materials. In many cases, the DSC lattice can be obtained by simple graphical construction based on the atomic positions in the structures, as in the examples shown here. The Burgers vectors and ledge vectors of interfacial line defects can then be obtained directly from the construction. In cases where graphical construction is difficult, the problem can be solved by computer techniques. The main limitations of the DSC method are that (a) it is a geometric hard-sphere construction

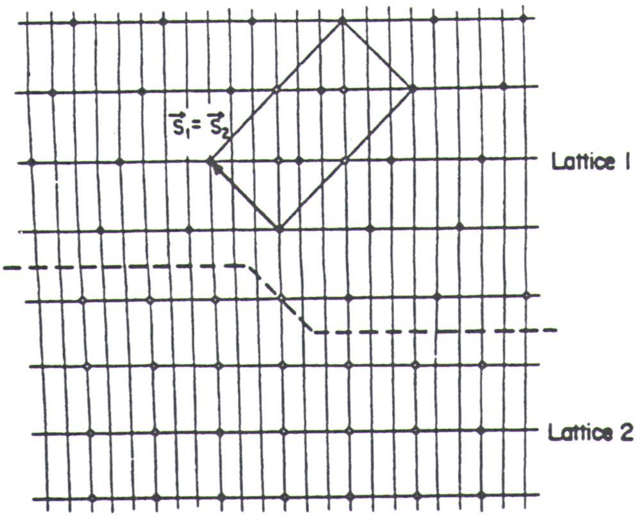

Figure 13.26. Pure ledge in the interphase boundary illustrated previously in Figure 13.24. The ledge vectors are shown above the ledge. Reprinted with permission from [53] by Elsevier Science Ltd., Oxford, England.

and thus unable to account for local atomic relaxations that can occur at interfaces, and (b) it represents an approximation in near-coincidence situations when there are two different types of lattices, as in Figure 13.24, for example. In spite of these limitations, it is easy to apply and useful for analyzing many different types of interfaces.

Before ending this section, it is worth noting that Pond [57,58] has developed a method for quantifying the nature of line defects in interfaces based on the space group symmetries of the adjacent crystals. This method is completely general and does not suffer from the limitations of the hard-sphere models above in its capability to quantify the character of interfacial defects. Because a thorough knowledge of space group crystallography is required to utilize this technique, it is not discussed in this book. However, it is highly recommended as additional reading for those familiar with space group notation. Several other approaches to the determination of grain boundary structure that have been developed are not mentioned here, because they are not critical to our discussion and they are summarized elsewhere [24,33,42,59].

13.2.4. Atomistic Modeling of Grain Boundary Structure and Energy

The main purpose of atomistic investigations of grain boundary structure is to relate the structure and grain boundary energy γ_{gb} to the grain misorientation and boundary plane. The calculations are usually performed by establishing an initial relationship between two grains using the five macroscopic degrees of freedom discussed in Section 13.2.1. An atomic potential is chosen and the bicrystal is then allowed to relax into a minimum energy configuration through a suitable algorithm, as discussed in Section 1.3 [7,60]. Relative translations of the two lattices through the three microscopic degrees of freedom and/or local atomic rearrangements are all allowed as part of the minimization process. Initially, there was some question as to the validity of the interatomic potentials used in the calculations, the approximations used to reach equilibrium and whether calculated energy minima corresponded to real energy minima, but these uncertainties have been largely relieved by extensive comparison between calculated and observed grain boundary structures [2,7].

Two important fundamental insights have arisen from calculations of the structure and energies of grain boundaries in metals. Firstly, it has been shown that the structure of grain boundaries can be described as composed of several structural (or polyhedral) units, which are repeated in a particular sequence along the boundary, depending on the type of boundary and angle of misorientation. This result is appealing because of its conceptual simplicity and because it relates to certain properties of boundaries such as nearest-neighbor bonding, segregation and diffusion. Secondly, it has been shown that the grain boundary energy is directly correlated with the volume expansion of the boundary per unit area and that this feature relates to the nearest-neighbor hard-sphere character of the atoms. These studies have also elucidated the reason why the CSL model does not accurately predict the energies of grain boundaries except in special orientations. Each of these subjects is exam-

---

ined in greate
the structure
dency, which

Structural (
is shown in Fi
tures calculate
boundaries are
labeled B and
ly of a single
amination of
sponds to the
the boundary
of the $\Sigma = 5$
boundary can
every two B u
additional mis
displayed in t
tions of grain
undisturbed la
and the crysta
nent among th
mination of tw
each crystal.

The pic
range of all p
into sectors, e
$\Sigma = 1$ (A unit
structural unit
quence and in
d). The stress
agree with the
equivalent to t
It is important
aries in Figure
ary structure s

Another
structural units
polyhedra that
in Figure 8.3,
[67,68]. An ex
Archimedian a
boundary in f.c
bor environme
fore, that we m

occur at interfaces, ons when there are spite of these lim- ent types of inter-

,58] has developed based on the space pletely general and ove in its capabili- ough knowledge of it is not discussed ading for those fa- e determination of oned here, because marized elsewhere

e and Energy

tructure is to relate ntation and bound- an initial relation- freedom discussed is then allowed to algorithm, as dis- ttices through the gements are all al- me question as to s, the approxima- inima correspond- ely relieved by ex- undary structures

alculations of the s been shown that f several structural along the bound- tion. This result is es to certain prop- ion and diffusion. directly correlated this feature relates studies have also edict the energies subjects is exam-

---

ined in greater detail below, because they provide an atomistic picture that relates the structure of grain boundaries to their energy and also to their segregation tendency, which is discussed in the next section.

Structural (Polyhedral) Unit Model An example of the structural unit model is shown in Figure 13.27 for a series of symmetrical [001] tilt grain boundary structures calculated using a pair potential appropriate for f.c.c. copper [61]. These tilt boundaries are seen to be composed of various mixtures of the basic structural units labeled B and A in Figures 13.27b and e, respectively. Boundaries composed entirely of a single structural unit (such as Figs. 13.27b and e) are special boundaries. Examination of Figure 13.27c shows that each A unit in the $\Sigma = 17$ boundary corresponds to the termination of two symmetrical (120) planes. Hence, each A unit in the boundary represents a dislocation with $\mathbf{b} = 1/5[120]$. This is a DSC lattice vector of the $\Sigma = 5$ coincidence lattice shown in Figure 13.27b. Thus, the $\Sigma = 17$ grain boundary can be considered as a $\Sigma = 5$ boundary with A units interspersed between every two B units. This agrees with the picture of DSC dislocations accommodating additional misfit between CSL orientations developed in Section 13.2.3, but now displayed in terms of the A and B structural units derived from atomistic calculations of grain boundary structure. The A units are elements of a 90° boundary in the undisturbed lattice in Figure 13.27e, for which $\Sigma = 1$ and the unit cells of the DSC and the crystal lattice are identical. When the B units occur as a minority component among the A units in the $\Sigma = 37$ boundary in Figure 13.27d, they mark the termination of two (110) planes, or an ordinary lattice dislocation with $\mathbf{b} = 1/2[110]$ in each crystal.

The picture that emerges from the structural unit model [61–63] is that the range of all possible misorientations between two grains can be viewed as divided into sectors, each delimited by two special boundaries, such as $\Sigma = 5$ (B units) and $\Sigma = 1$ (A units) above. Within each sector, the intermediate boundaries consist of structural units taken from the delimiting special ones, arranged in an ordered sequence and in proportions given by a linear rule of mixtures (as in Figs. 13.27c and d). The stress fields surrounding the relaxed boundaries in Figures 13.27c and d agree with the presence of primary and secondary dislocations and, therefore, are equivalent to the previous dislocation description of grain boundary structure [64]. It is important to note that the structural units formed in the relaxed grain boundaries in Figure 13.27b can be identified in a distorted shape in the unrelaxed boundary structure shown in Figure 13.27a.

Another interesting feature of the structural unit model is that the various structural units formed in relaxed grain boundaries correspond to the same type of polyhedra that are the basic units of the liquid structure [65,66], shown previously in Figure 8.3, and also found in hard-sphere models of grain boundary structure [67,68]. An example of this is shown in Figure 13.28, where an octahedron and Archimedian antiprism are outlined in the structure of a $\Sigma = 13$ (001) twist grain boundary in f.c.c. silver. Such data indicate that the nearest- and next-nearest-neighbor environment at grain boundaries in solids is similar to that of liquids and, therefore, that we might think of segregation to such boundaries in terms of the equilibri-

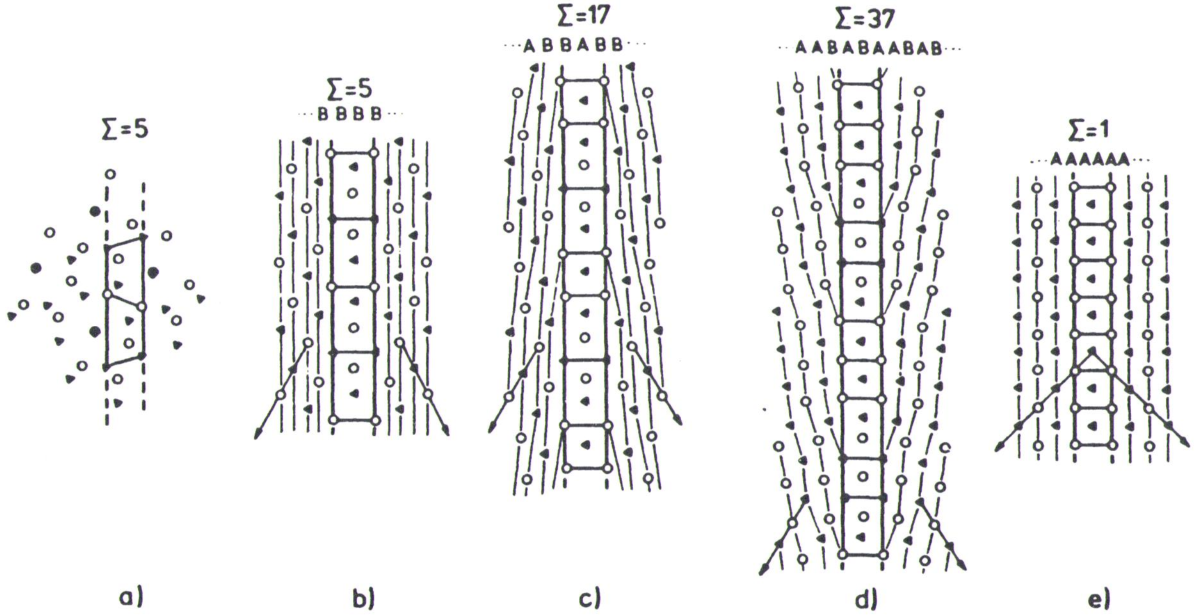

Figure 13.27. (a) Unrelaxed, and (b–e) relaxed core structures of symmetrical [001] tilt boundaries in copper in terms of *A* and *B* structural units. The open circles indicate atoms at $z = 0$ and the filled triangles at $z = 1/2$. From [30,45].

Figure 13.27. (a) Unrelaxed, and (b–e) relaxed core structures of symmetrical [001] tilt boundaries in copper in terms of A and B structural units. The open circles indicate atoms at $z = 0$ and the filled triangles at $z = 1/2$. From [30,45].

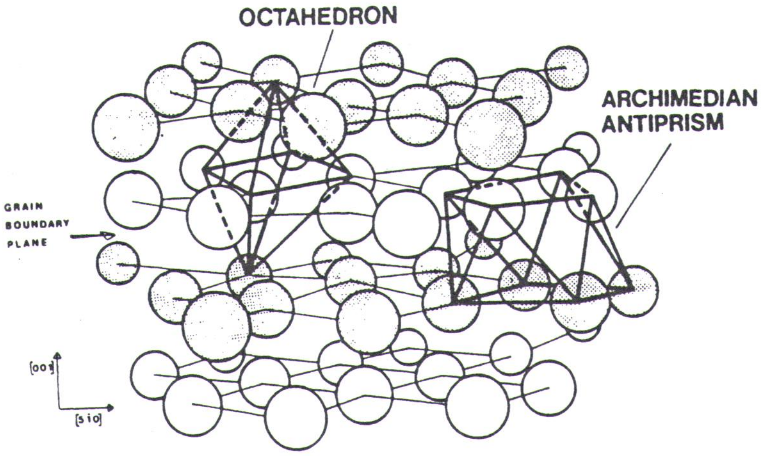

Figure 13.28. Structure of a $\Sigma = 13$ (001) twist boundary in silver determined from diffraction experiments and atomistic modeling. From [69].

um partition ratio k_e, discussed previously with reference to Figure 6.11. In addition, the polyhedra formed in liquids tend to maximize nearest-neighbor coordination, and, as we will see in the following section, this has an important effect on the grain boundary energy.

Structure–Energy Correlation The results presented in this section are based on a recent review by Wolf and Merkle [7], who have performed an extensive comparison between atomistic modeling and HRTEM observation of grain boundary structure. In this section, we emphasize only those aspects of their results that help to provide a nearest-neighbor broken-bond picture of grain boundaries, similar to our previous analyses of solid–vapor and solid–liquid interfaces, and also to establish a relationship with the dislocation and structural unit models of grain boundary structure discussed previously. Many of the data compare results obtained from atomistic calculations using both many-body embedded-atom-method (EAM) potentials for gold and the familiar Lennard–Jones (LJ) pair potential for copper. We show only the results for these f.c.c. metals, but Wolf and Merkle [7] show a similar series of data for b.c.c. metals.

Figure 13.29 shows the grain boundary energy γ_{gb} as a function of angle of misorientation ψ (using the notation of Eq. 13.7) for <110> symmetrical tilt grain boundaries (STGBs) in f.c.c. gold and copper. Note that both metals give qualitatively similar results and that the energies of copper are generally higher than those of gold, which we expect based on the relative strengths of the atomic bonds in the two metals (compare with the average surface energies in Table 3.3 for example). Also note that these data are similar to those shown previously for aluminum in Figures 13.8c and d. All of these metals display deep cusps when the low-index (111), (100) and (110) planes are parallel across the boundary, as indicated by the symmet-

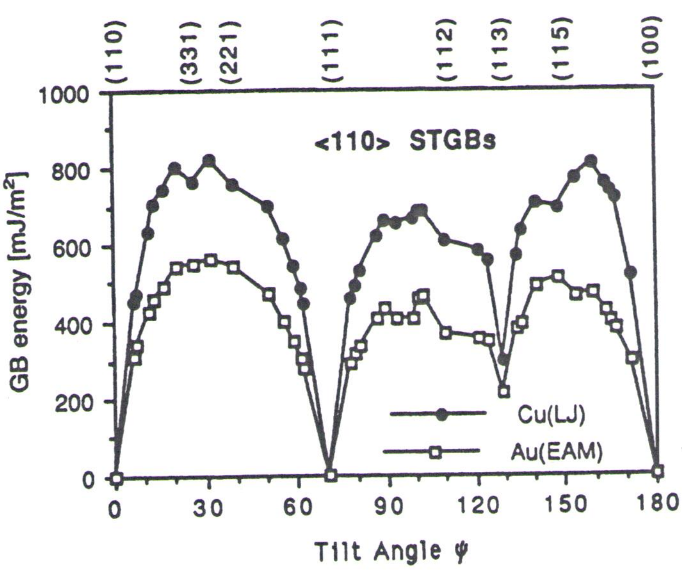

Figure 13.29. The energies of symmetric <110> tilt grain boundaries in copper and gold as a function of angle of misorientation. From [7].

rical tilt grain boundary planes (*hkl*) at the top of the figure. Hence, these data indicate that there is a correlation between the atomic density of the planes comprising the grain boundary and the energy of the boundary. This correlation has the same trend as the solid–vapor interfaces in Figure 3.16, although there are clearly additional cusps present in the grain boundary data [e.g., at (113)] which are absent in the case of solid–vapor interfaces. An alternate way of expressing this correlation is to note that there is an inverse relationship between the interplanar spacing of the planes parallel to the grain boundary and the grain boundary energy, with widely

Table 13.3. Intrinsic stacking fault and twin boundary energies in various f.c.c. metals

Metal	γ_{isf} (mJ/m²)	γ_{isf}/dT (mJ/m²·°C)	γ_t (mJ/m²)
Al	166	−0.04	75
Ni	128	−0.04	43
Cu	78	−0.04	24
Ag	22	−0.006	8
Au	45	−0.02	15
Pt	322	−0.08	161

Source: From [24] and [39].

---

spaced low-index pla
boundary energies.

This relationsh
surfaces is further ill
grain boundaries and
face energy (express
into two surfaces as i
relation between the
of other cusps in the
aries has some simil
experiments, an RGB
are assumed to be r
atoms are assumed t
larity of the RGB m
tion between the inte
ary energy, particula
reduction in energy t
grain boundary, due

Figure 13.31 s
twist angle θ for LJ

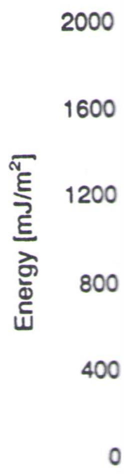

Figure 13.30. Compa
ces for <110> gold.
corresponds to the RG

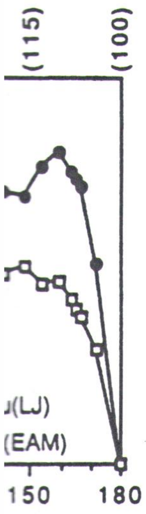

ries in copper and gold as a

:. Hence, these data indi-
of the planes comprising
correlation has the same
h there are clearly addi-
13)] which are absent in
essing this correlation is
nterplanar spacing of the
lary energy, with widely

ıergies in various

γ_t (mJ/m^2)
75
43
24
8
15
161

spaced low-index planes such as (111) and (100) generally displaying lower grain boundary energies.

This relationship between the energy of symmetrical tilt grain boundaries and surfaces is further illustrated in Figure 13.30, where the results for symmetrical tilt grain boundaries and random grain boundaries (RGBs) are compared with the surface energy (expressed as $2\gamma^{SV}$, the energy necessary to separate a grain boundary into two surfaces as in an ideal cleavage experiment) of gold. Again we note a correlation between the deep cusps associated with low-index planes, but the absence of other cusps in the case of surfaces, suggesting that the behavior of grain boundaries has some similarities but is more complicated than that of surfaces. In these experiments, an RGB is defined such that all interactions across the grain boundary are assumed to be random with the constraint that, as in actual boundaries, the atoms are assumed to lie in well-defined planes parallel to the boundary. The similarity of the RGB model with the symmetrical tilt model again indicates a correlation between the interplanar spacing parallel to the boundary and the grain boundary energy, particularly for the three most densely packed planes. Note the large reduction in energy that occurs when the two surfaces are joined to form a random grain boundary, due to the elimination of broken bonds at the interface.

Figure 13.31 shows the energies γ_{gb} of symmetrical twist boundaries versus twist angle θ for LJ copper for the (111), (001), (011) and (113) grain boundary

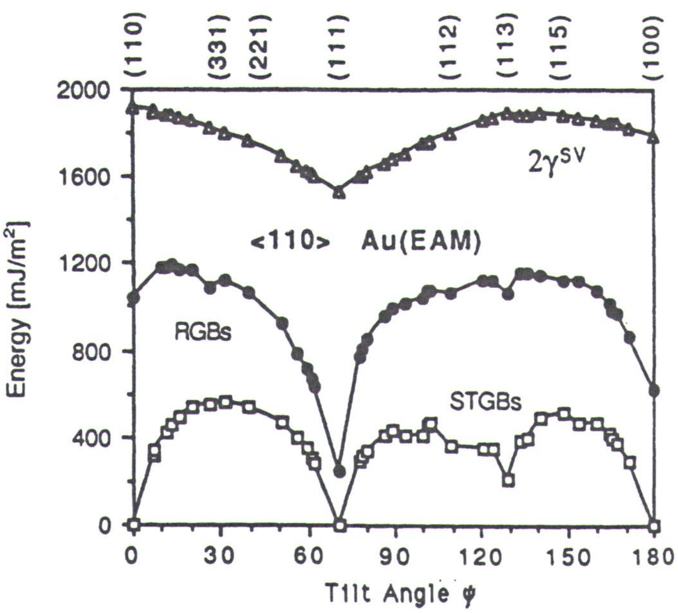

Figure 13.30. Comparison of the energies of RGBs and STGBs with those of the free surfaces for <110> gold. Note that the energy of two free surfaces $2\gamma^{SV}$ is plotted and that this corresponds to the RGB limit for a grain boundary expansion (Eq. 13.9) of $\Delta V_I \rightarrow \infty$ From [7].

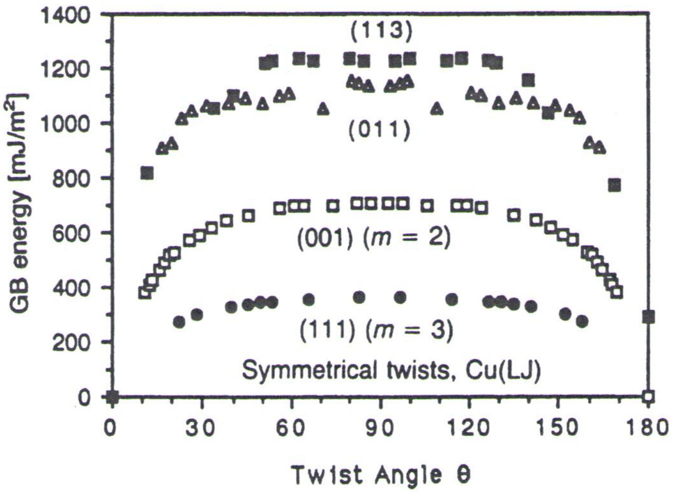

Figure 13.31. Energies of symmetrical twist boundaries versus twist angle for the four densest planes of f.c.c. copper obtained with an LJ potential. The only significant cusps occur at the beginning and endpoints of the misorientation range where there are small planar unit cells in the boundary. From [7].

planes indicated in the figure. In these figures, $\theta = 180°/n$, where n indicates a possible rotation symmetry for the planar unit cell of the grain boundary. These data clearly show that the lowest grain boundary energies are associated with the most densely packed planes of the crystal and that the curves are rather featureless over a large range of twist angle, in comparison to the tilt boundaries in Figure 13.29. The only significant cusps at the beginning and endpoints of the twist misorientation range indicate that, in the case of twist boundaries, small planar unit-cell areas in the boundary correspond to low energies. The lack of variation in energy with twist angle except at the endpoints and the strong dependence on the interplanar spacing indicates that it is the short-range repulsion of the atoms and the volume expansion at the interface that dominate the grain boundary energy. Thus, the formation of twist grain boundaries on planes that are widely spaced and contain a high density of atoms with small planar unit-cells leads to lower-energy grain boundary structures.

Wolf and Merkle [7,70] also examined the correlation between the grain boundary energy and the volume expansion per unit area at the grain boundary $\Delta V_i/\alpha$ for symmetrical and asymmetrical tilt and twist grain boundaries in copper and gold, and their results are compiled in Figure 13.32. These data indicate a nearly linear relationship between the volume expansion per unit area of grain boundary and the grain boundary energy. This general relationship appears to exist for all types of grain boundaries. Figure 13.33 shows a second important correlation obtained from this study. This figure shows that there is an approximately linear relationship between the grain boundary energy γ_{gb} and the number of nearest-neighbor

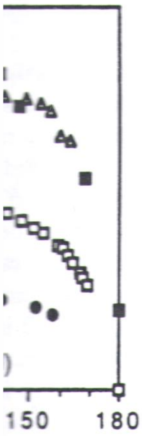

st angle for the four dens-
significant cusps occur at
e are small planar unit cells

where n indicates a pos-
n boundary. These data
ssociated with the most
rather featureless over a
ies in Figure 13.29. The
he twist misorientation
lanar unit-cell areas in
ion in energy with twist
the interplanar spacing
d the volume expansion
Thus, the formation of
l contain a high density
grain boundary struc-

ion between the grain
at the grain boundary
n boundaries in copper
se data indicate a near-
area of grain boundary
appears to exist for all
portant correlation ob-
proximately linear rela-
ber of nearest-neighbor

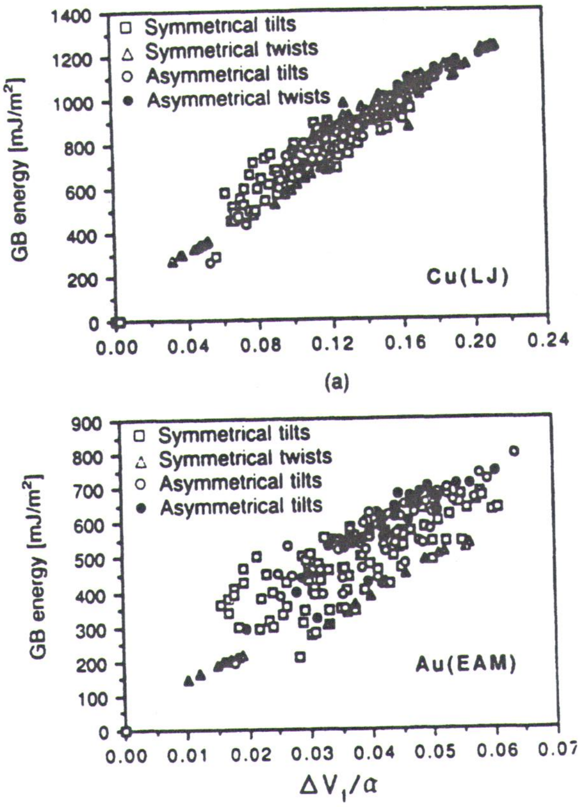

(a)

(b)

Figure 13.32. Correlation between the grain boundary energy and volume expansion per unit area (normalized by the lattice parameter) for symmetrical and asymmetrical tilt and twist grain boundaries in f.c.c. metals using an (a) LJ copper potential and (b) EAM gold potential. From [7].

broken bonds per unit grain boundary area $n_b N_{s\{hkl\}}$. These data were again obtained from the atomistic calculations and the effects of second-nearest- and higher-neighbor contributions were estimated to be typically less than 10% to 20% of the nearest-neighbor contribution for the LJ potential and even smaller for the EAM potential. Although the details of the interfacial structure are not accounted for in this correlation, the relationship between the number of nearest-neighbor broken bonds and the grain boundary energy is clearly evident, and it establishes a direct link with all of our previous treatments of interfacial structure based on broken-bond models. Further comparison between Figures 13.32 and 13.33 shows that there is a correlation between the volume expansion at the grain boundary and the number of nearest-neighbor broken bonds per unit area for the two f.c.c. potentials. The physical basis for this correlation is that, as the number of broken bonds (or roughness of the

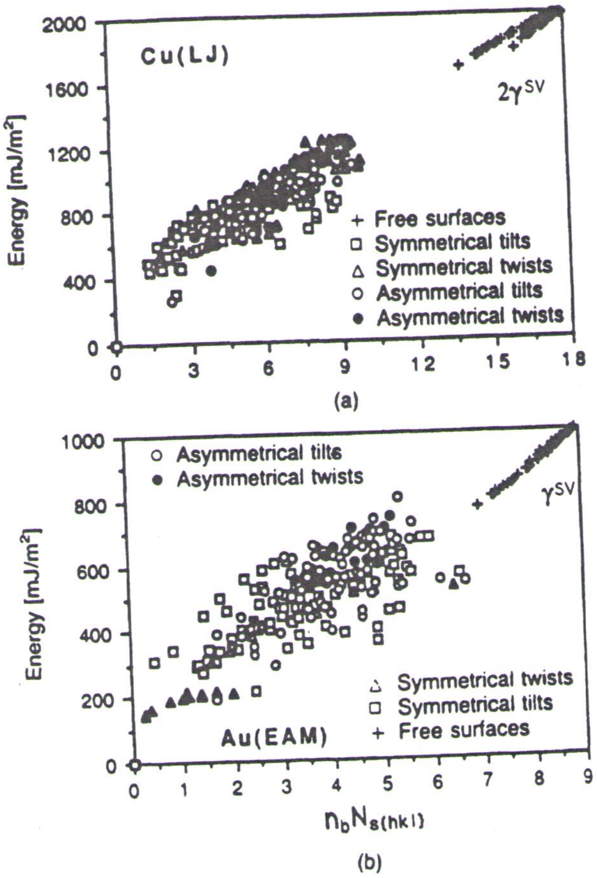

Figure 13.33. Grain boundary energy versus number of nearest-neighbor broken bonds per unit area for f.c.c. metals. The related surface energies are also shown for comparison. From [7].

interface) increases, the ability of the two surfaces comprising the grain boundary to obtain good matching decreases, leading to a volume expansion at the grain boundary (Eq. 13.9) with a corresponding increase in the grain boundary energy. The increase in grain boundary energy from the volume expansion is equivalent to the surface stress described in Part II (Eq. 3.11).

We have examined the structure and properties of grain boundaries from a number of different viewpoints in Section 13.2, and it is worth summarizing some of the more important conclusions and relationships that arise from these treatments. First, it is important to remember that regardless of whether the Read-Shockley, CSL/DSC or structural unit model is used to interpret the structure of grain boundaries, they all model the boundary as being composed of areas of good and poor matching, with the poor matching comprised of dislocations. Areas of good

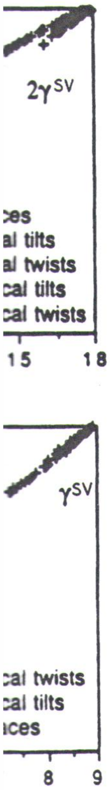

ıeighbor broken bonds per
ıown for comparison. From

ng the grain boundary to
ısion at the grain bound-
oundary energy. The in-
ı is equivalent to the sur-

ɡrain boundaries from a
orth summarizing some
arise from these treat-
vhether the Read-Shock-
t the structure of grain
ed of areas of good and
ocations. Areas of good

matching are generally associated with low energy, whereas those with poorer matching generally have higher energy. This relationship is not always simple, but it is quantifiable in terms of the dislocation models and atomistic calculations presented. The atomistic models lead back to the idea of arrangements of structural units in a grain boundary, which possess certain numbers of nearest-neighbor broken bonds. These correlate with the energy, so that ultimately, all of these approaches have a similar physical origin associated with the stretching and breaking of atomic bonds, as presented in Section 1.2.

The dislocation cores represent groups of atoms with different atomic arrangements than in the bulk. When the dislocations are far apart, both the core structure and the associated elastic strain fields contribute to the total energy of the boundary. The core energy may be a small part of the total energy when the dislocations are far apart, and then the Read–Shockley model, which accounts for the logarithmic behavior of the elastic strain fields, is able to accurately characterize the boundary structure and energy. When the dislocation cores overlap, the elastic strain fields become a negligible part of the energy, and the local bonding arrangements at the cores constitute most of the structure and energy. In this case, the other models of high-angle grain boundary structure such as the CSL/DSC, structural unit or atomistic models become more appropriate. Any of these models still has regions of good and poor matching and involves various arrangements of atoms with nearest-neighbor broken bonds, which then determine the boundary energy, so they are conceptually similar. A major insight into all these models is that it is possible to consider quantifying the structure, defects and energies of homophase interfaces, in this case grain boundaries, in terms of nearest-neighbor atomic bonding, although the situation is clearly more complex when the interface is composed of two crystalline solids instead of only one.

13.2.5. Stacking Faults and Twin Boundaries

The atomic structure of stacking faults and twin boundaries can be readily envisioned in f.c.c. crystals, which consist of an ABCABC . . . stacking of close-packed $\{111\}$ crystal planes. Figure 13.34 shows schematically the distinction between intrinsic (i) and extrinsic (e) stacking faults and shows for comparison the relationship with twins in f.c.c. metals and alloys. If a single $(\bar{1}11)$ plane is removed from the usual stacking of $(\bar{1}11)$ planes in an f.c.c. crystal in Figure 13.34a, an intrinsic stacking fault with an ABCBC . . . stacking sequence occurs, as illustrated in Figure 13.34b. Conversely, if an extra $(\bar{1}11)$ plane of atoms is inserted into the crystal, an extrinsic stacking fault with an ABCBABC . . . stacking sequence results, which is also shown in Figure 13.34b. An alternate description of the extrinsic fault is that it arises from the superposition of two intrinsic faults, as illustrated in Figure 13.34c. If intrinsic faults occur on every $(\bar{1}11)$ plane, then thin twins form within the crystal, as illustrated in Figures 13.34d and e. On this basis, an extrinsic fault is simply a one-layer twin. As we have seen throughout this book, the interfacial energy is largely governed by the nearest-neighbor bonding between atoms. Based on this, the energies of intrinsic and extrinsic stacking faults are expected to be similar

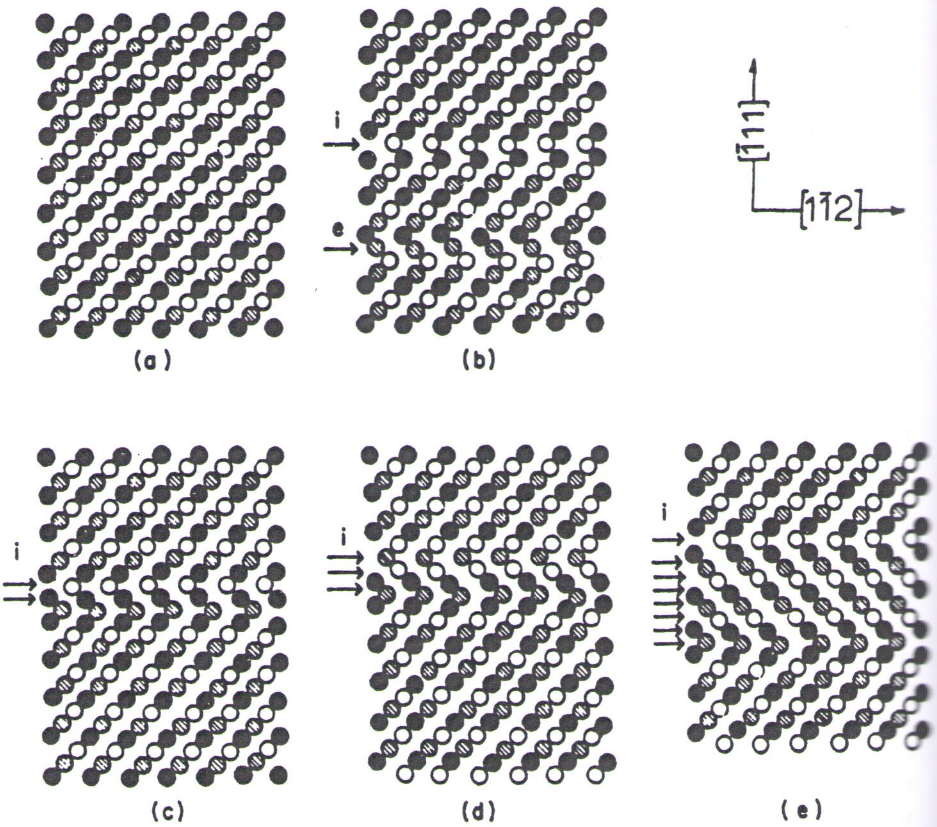

Figure 13.34. Idealized view of stacking faults and their development from perfect crystal in (a) to an *n*-layer twin in (e) in the close-packed f.c.c. structure. The viewing direction is along [110]. From [24].

and the twin boundary energy is expected to be only about half of the intrinsic stacking-fault energy based on the number of nearest-neighbor bonds that are in the wrong stacking sequence. In the case of two twinned crystals, if a $(\bar{1}11)$ interface plane is defined and the top half of the crystal is rotated 180° about the interface normal, a coherent twin boundary with an ABCACBA . . . stacking like that in Figure 13.34e results. This is a special type of $\Sigma = 3$ grain boundary, and an example of this was shown in Figure 12.1.

The stacking fault energies γ_{sf} of metals and alloys can be determined directly from measurements on extended dislocation nodes or from the separation of partial dislocations in the TEM [39,71,72] as well as by several other methods [24]. Values for the intrinsic stacking fault energies (γ_{isf}) of several f.c.c. metals are given in Table 13.3. Values for the temperature coefficients of the stacking fault energies are also given in Table 13.3. These are seen to be negative in accordance with Eq.

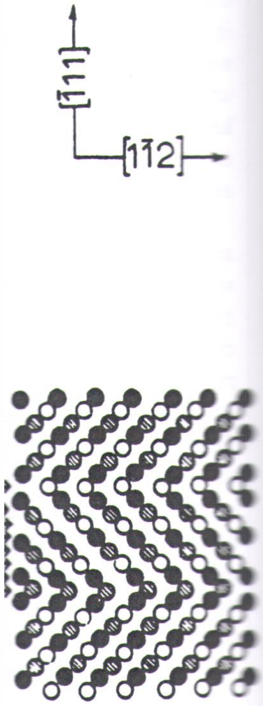

(e)

nt from perfect crystal in
iewing direction is along

t half of the intrinsic
r bonds that are in the
ls, if a $(\bar{1}11)$ interface
0° about the interface
acking like that in Fig-
ary, and an example of

be determined direct-
the separation of par-
al other methods [24].
f.c.c. metals are given
stacking fault energies
n accordance with Eq.

(3.14) and have relatively small values, which is reasonable physically given the low entropy associated with stacking faults.

Unlike stacking fault energies, measurement of twin boundary energies (γ_t) are indirect and depend on a knowledge of the average surface or grain boundary energies and substitution into ratios with these quantities. Hence, there is much greater uncertainty in these measurements. Values for the twin boundary energies in f.c.c. metals are also shown in Table 13.3, and these are observed to be approximately one-third to one-half of the corresponding stacking fault energies. Only a few estimates of $d\gamma_t/dT$ are available, and they are similar to the values for γ_{isf}/dT listed in Table 13.3.

Hirth and Lothe [39] have proposed on geometrical grounds that the stacking fault and coherent twin-boundary energies at 0 K can be represented by the number of pairs of atom planes of separation n that are not in the proper f.c.c. stacking sequence, multiplied by the distortional energy ϕ_n per pair. As indicated when considering the planar stacking sequences of the f.c.c. faults and twin boundaries above, there should be a relationship between the intrinsic and extrinsic stacking fault energies and the twin-boundary energy, such that $\gamma_{isf} \cong 2\gamma_t$. The coherent twin boundary has one pair of second-nearest-neighbor planes ($n = 2$) out of sequence, two third-nearest-neighbor planes ($n = 3$), one fourth-nearest-neighbor plane ($n = 4$), and so on. Based on this nearest-neighbor plane consideration and the relationships of the various fault boundaries, the twin boundary and the intrinsic and extrinsic stacking fault energies can be expressed as

$$\begin{aligned}\gamma_t &= \Sigma\,[2n\phi_{3n} + n(\phi_{3n-1} + \phi_{3n+1})]\\ &= \phi_2 + 2\phi_3 + \phi_4 + \ldots,\end{aligned} \tag{13.31}$$

$$\begin{aligned}\gamma_{esf} &= \Sigma\,[2\phi_{3n-1} + (3n+1)\phi_{3n} + 3n\phi_{3n+1}]\\ &= 2\phi_2 + 4\phi_3 + 3\phi_4 + \ldots,\end{aligned} \tag{13.32}$$

$$\begin{aligned}\gamma_{isf} &= \Sigma\,[(3n-1)\phi_{3n-1} + 3n\phi_{3n}]\\ &= 2\phi_2 + 3\phi_3 + 0\phi_4 + \ldots,\end{aligned} \tag{13.33}$$

$$\begin{aligned}\gamma_{hcp} &= \Sigma\,[\Psi_{6n-2} + \Psi_{6n-3} + \Psi_{6n-4})]\\ &= \phi_2 + \phi_3 + \phi_4 + \ldots.\end{aligned} \tag{13.34}$$

Also listed is γ_{hcp}, the fault energy per close-packed plane of an h.c.p. crystal, which is regarded as a completely faulted f.c.c. crystal due to an intrinsic stacking fault on every other f.c.c. plane. Thus, this value represents the f.c.c. to h.c.p. transformation energy per layer and corresponds to calculation of the interphase boundary energy of the f.c.c.–h.c.p. interface shown in Figure 13.4.

The energy ϵ_j of a jth nearest-neighbor atom pair in an f.c.c. crystal is associated with its atomic separation r_j. Hirth and Lothe [39] have shown that the associated shear displacements for the faults above can be represented by $r_j \rightarrow r_j'$ and $r_j \rightarrow r_j''$, where the sheared vector separations r_j' and r_j'' are given by the original separations r_j plus the shear displacement vectors of the type 1/6<112>. The pair energies ϕ_j can be expressed in terms of the bond energies ϵ_j (ϵ_b in Eq. 1.4) so that, including bonds out to the eleventh nearest neighbors, pair energies can be given in terms of the bond energies as follows:

$$\phi_2 = \epsilon_3' - 3\epsilon_3 + 6\epsilon_3'' - 3\epsilon_4 - 6\epsilon_5 + 6\epsilon_4' - 6\epsilon_5',$$

$$\phi_3 = -\epsilon_6 + 3\epsilon_6',$$

$$\phi_n = 0 \quad (n > 3).$$

Substituting these into Eqs. (13.31) through (13.34), then yields

$$\gamma_t = \epsilon_3' - 3\epsilon_3 + 6\epsilon_3'' - 3\epsilon_4 - 6\epsilon_5 + 6\epsilon_4' - 2\epsilon_6 + 6\epsilon_6' + 6\epsilon_5, \tag{13.35}$$

$$\gamma_{esf} = 2\epsilon_3' - 6\epsilon_3 + 12\epsilon_3'' - 6\epsilon_4 - 12\epsilon_5 + 12\epsilon_4' - 4\epsilon_6 + 12\epsilon_6' + 12\epsilon_5', \tag{13.36}$$

$$\gamma_{isf} = 2\epsilon_3' - 6\epsilon_3 + 12\epsilon_3'' - 6\epsilon_4 - 12\epsilon_5 + 12\epsilon_4' - 3\epsilon_6 + 9\epsilon_6' + 12\epsilon_5', \tag{13.37}$$

$$\gamma_{hcp} = \epsilon_3' - 3\epsilon_3 + 6\epsilon_3'' - 3\epsilon_4 - 6\epsilon_5 + 6\epsilon_4' - \epsilon_6 + 3\epsilon_6' + 6\epsilon_5', \tag{13.38}$$

where the fault energies are expressed as the energy per atomic area in the fault. From these relations, it is observed that

$$\gamma_{isf} \cong \gamma_{esf} = 2\gamma_t \tag{13.39}$$

and the f.c.c.–h.c.p. interphase boundary energy is found to be the same as the coherent twin boundary energy. These results agree reasonably well with recent density-functional theory calculations of γ_{isf}, γ_{esf}, and γ_t in aluminum [73] and the values shown in Table 13.3.

13.2.6. Roughening, Phase Transformations and Melting

Grain boundaries display phenomena such as roughening (and faceting) and phase transformations as a function of temperature and alloying just like solid–vapor interfaces. Unfortunately, because of the additional complexities of grain boundaries, relatively simple analytical or atomistic treatments of these phenomena are not available. However, we can rationalize these phenomena using the same sort of nearest-neighbor bonding arguments as for solid–vapor interfaces. In this section, we mainly present data that demonstrate these phenomena for the case of homophase interfaces and rationalize them using qualitative, intuitive arguments.

Cahn [74] has presented a comprehensive analysis of the thermodynamics of grain boundary phases and the possible types of transformations that may occur between them. One possible type of phase transformation is a faceting transformation

---

in which an initiall
structure consisting
of intersection. Fi
faceting phase tran
TEM [75]. The bo
with initial $\{112\}_1$

Figure 13.35. Rever
asymmetric <111> ti
step-wise heating (a
Reprinted with permi

in which an initially flat (single phase) grain boundary may transform to a faceted structure consisting of two or more facet types (phases) that coexist along their lines of intersection. Figure 13.35 shows an example of this type of roughening or faceting phase transformation in a sample of pure aluminum heated *in situ* in the TEM [75]. The boundary under observation is an asymmetric <111> tilt boundary with initial $\{112\}_1/\{112\}_2$ facets as illustrated in Figure 13.36a. Upon heating the

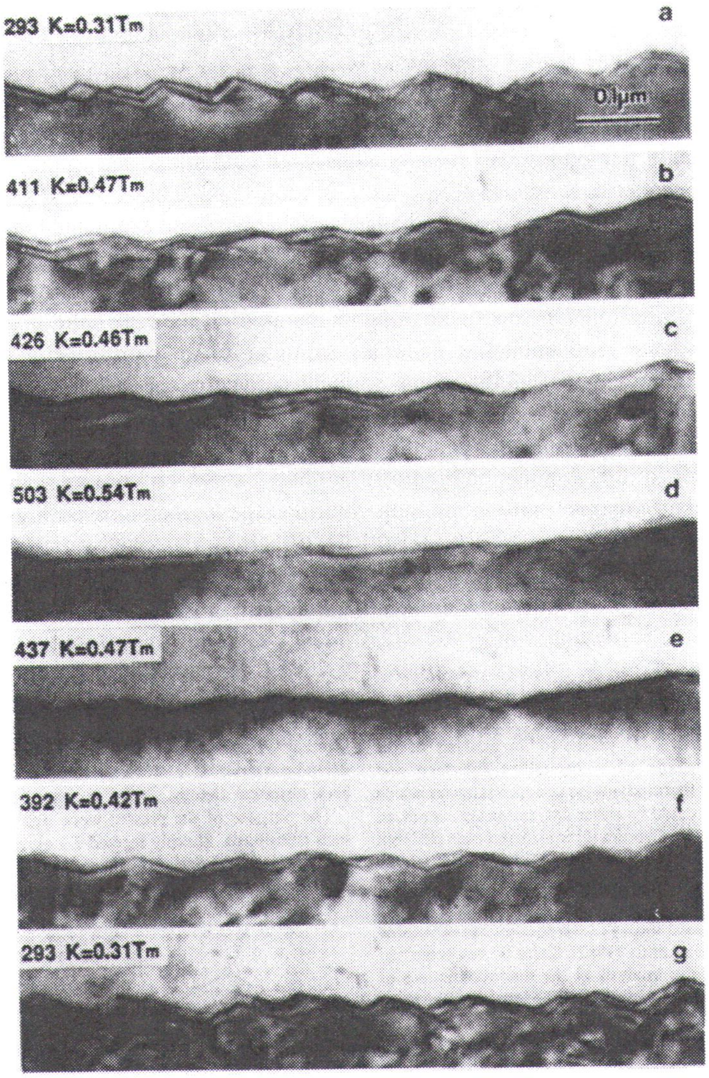

Figure 13.35. Reversible roughening–faceting transformation of an initially faceted $\Sigma = 3$ asymmetric <111> tilt boundary containing $\{112\}_1/\{112\}_2$ facets in aluminum as a function of step-wise heating (a-d) and subsequent cooling (d-g). Time at each temperature ≅ 30 min. Reprinted with permission from [75] by Elsevier Science Ltd., Oxford, England.

initially faceted sample to $0.54T_m$ in Figure 13.35d, the facets become almost flat and parallel to $\{110\}$. Upon cooling, the process reversed itself and a sharply faceted structure was regained at room temperature in Figure 13.35g. At each temperature, the boundary was observed to rapidly adjust to the temperature change and then maintain this configuration during the isothermal hold. This is illustrated in Figure 13.36b, which shows the amplitude of the $\{112\}_1/\{112\}_2$ facets on the $\Sigma = 3$ grain boundary as a function of time and temperature. These data clearly demonstrate that grain boundary roughening occurs with increasing temperature, just as for the solid surfaces shown in Figures 4.11 and 4.12 for example. The roughening temperature is slightly more than half of the melting temperature in Figure 13.36, which is similar to that of solid surfaces. Although the mechanism of roughening was not determined in Figure 13.36, it is likely that it is due to the formation of atomic ledges and kinks in the grain boundary. Another interesting example of a phase transformation in [001] twist boundaries in gold due to segregation of iron to the interface has been reported [76], but it is not discussed here.

The phenomenon of grain boundary melting has been examined both theoretically and experimentally by several groups [77–81]. Interpretations of the data vary, but it appears that there is not strong evidence for grain boundary premelting at temperatures much below the melting temperature of the bulk solid in any of the metals, ionic or semiconducting materials examined. What is observed in the atomistic simulations is that melting tends to nucleate heterogeneously at grain boundaries in crystals at temperatures approaching the melting point ($0.98T_m$ for example) and then spread into the remaining solid as the temperature is raised slightly. An example of this is shown in Figure 13.37 for a $\Sigma = 5$ (310) tilt grain boundary in a molecular dynamics study of sodium chloride. The temperatures in Figure 13.37 correspond to $0.96T_m$ for 1029 K, $0.98T_m$ for 1054 K and $0.993T_m$ for 1065 K. The whole system was liquid at 1072 K ($1.003T_m$). There was no superheating in the simulation and the grain boundary was found to melt at temperatures only slightly below the bulk melting temperature and move continuously and rapidly into the bulk crystal. Thus, it appears that melting is able to initiate at grain boundaries because they are defects, but the onset of melting is very near the equilibrium melting temperature. This contrasts with surfaces, where atoms do not feel any restoring forces on one side and are thus able to melt at temperatures well below T_m. This makes grain boundaries considerably more resistant to melting according to the simple Lindemann criterion for melting discussed in Section 4.5.2. It has been shown that grain boundary melting is orientation dependent and therefore that some boundaries may melt at temperatures lower than those shown in Figure 13.37, but the results shown in Figure 13.37 are typical of most of the investigations to date.

13.2.7. TLK Model of Grain Boundary Motion

A model for the migration rate of grain boundaries based on a TLK mechanism has been proposed [82,83]. This model has many features in common with the TLK models for solid–vapor and solid–liquid interfaces discussed in Parts II and III, and with a model for heterophase interfaces presented subsequently in Section 14.7. Un-

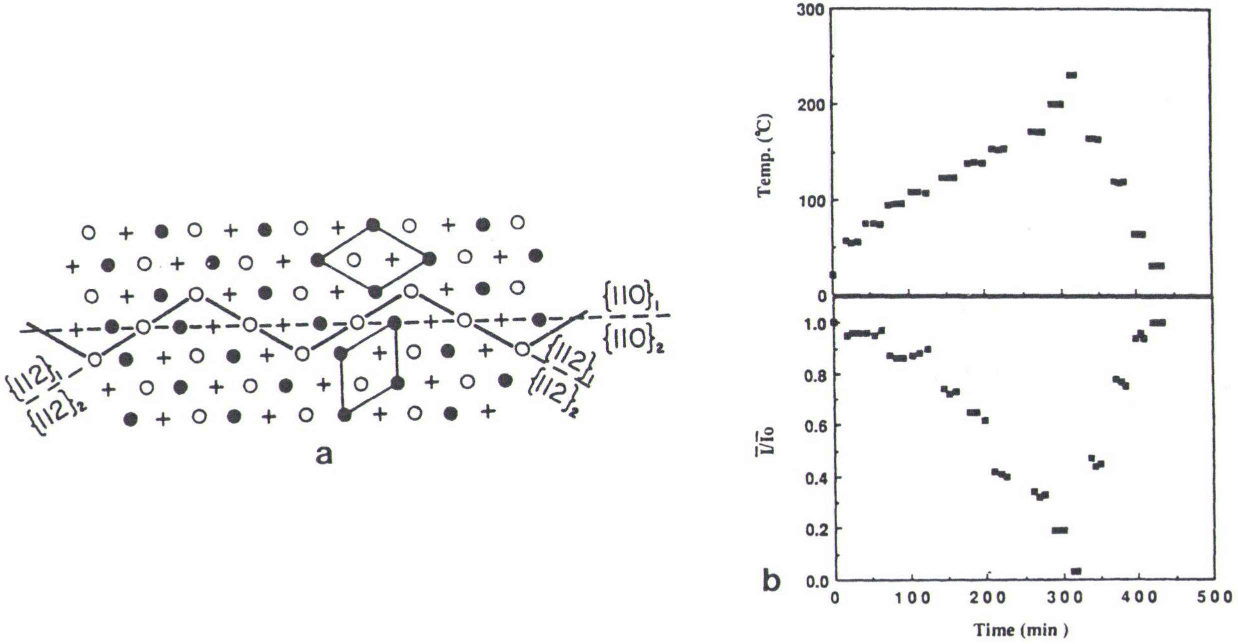

Figure 13.36. (a) Unrelaxed structure of faceted $\Sigma = 3$ asymmetrical-tilt boundary in an f.c.c. structure viewed along <111>. Different symbols indicate different planes in the ABC . . . stacking sequence. (b) Temperature and the corresponding normalized average amplitude of facets on the $\Sigma = 3$ grain boundary versus time, where $\bar{I}_o$ = initial average amplitude. Reprinted with permission from [75] by Elsevier Science Ltd., Oxford, England.

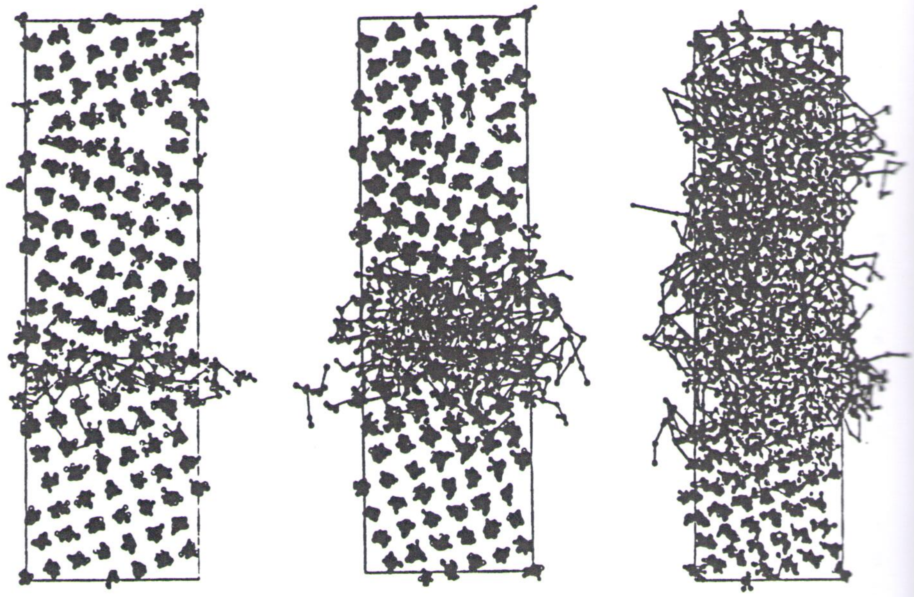

1029 K (*a*) 1054 K (*b*) 1065 K (*c*)

Figure 13.37. (a–c) Trajectory plots of instantaneous ion positions at three different temperatures for a $\Sigma = 5$ (310) tilt grain boundary in sodium chloride. From [78] copyright Taylor & Francis Ltd.

fortunately, there are few direct experimental data other than the original work of Gleiter [82,83] available for comparison with the model. Because there is a significant amount of experimental data on the atomistics and kinetics of motion of heterophase interfaces by a TLK mechanism, we provide only a brief description of the grain boundary model here. This model represents only one approach to the subject of grain boundary migration and a number of others are available [84–86]. As we have seen in the previous sections, the structure of grain boundaries is quite complicated and so is their migration behavior.

Gleiter's TLK model is based on the observation of motion of grain boundary ledges during *in situ* heating in the TEM. These ledges are evident from the displacement of the thickness fringes in the grain boundary where they cross a ledge, as shown in the bright-field TEM image in Figure 13.38. It is possible to calculate the heights of the ledges from the displacements [83], and they were found to vary from approximate 0.3 to 2.5 nm with most near the bottom of the range. These ledges were found to be generated primarily by spiral sources, similar to screw dislocations on solid surfaces, and at grain boundary intersections.

Based on the orientation relationships between the grains and the geometry of the grain boundaries in the TEM observations, a model of a migrating grain bound-

---

Figure 13.38. A g
as evident from th
by Elsevier Scienc

ary was constru
opposite sides o
{111} planes th
between the led
close-packed {1
por interface in
gested that migra

1. Dissociati
2. Diffusion
3. Dissociati
4. Diffusion
5. Condensat
6. The revers

The concept of d
vapor phase bet
structure of grain
quite reasonable
plete set of kinet

e different tempera-
] copyright Taylor &

original work of
there is a signifi-
of motion of het-
description of the
ach to the subject
le [84–86]. As we
es is quite compli-

of grain boundary
lent from the dis-
hey cross a ledge,
ssible to calculate
ere found to vary
the range. These
ilar to screw dis-

d the geometry of
ting grain bound-

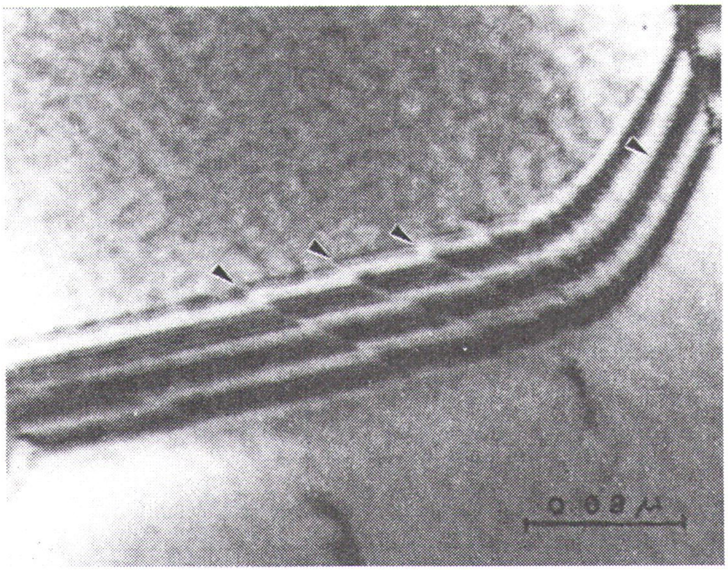

Figure 13.38. A grain boundary in aluminum–copper alloy containing several ledges (arrows), as evident from the displacement of the thickness fringes. Reprinted with permission from [83] by Elsevier Science Ltd., Oxford, England.

ary was constructed and is shown in Figure 13.39a. In this model, the terraces on opposite sides of the grain boundary were assumed to consist of the close-packed {111} planes that had the smallest inclination to the grain boundary. The spacing between the ledges in these planes was assumed to vary with the angle θ from the close-packed {111} planes as illustrated in Figure 13.39b, just as for the solid–vapor interface in Figure 4.2. By analogy with the case of solid surfaces, it was suggested that migration of the boundary occurred as follows:

1. Dissociation of atoms from kinks onto ledges
2. Diffusion of the atoms along the ledges
3. Dissociation from the ledges onto the {111} terraces
4. Diffusion on the terraces and desorption into the grain boundary
5. Condensation from the grain boundary onto the terrace of the opposite grain
6. The reverse process on the surface of the growing grain.

The concept of desorption into the grain boundary, as though it were a thin layer of vapor phase between the two grains, is not physically realistic given the atomic structure of grain boundaries. However, the TLK aspect of the model is probably quite reasonable on an atomic level. Based on this picture, Gleiter derived a complete set of kinetic equations for grain boundary motion [82]. His results predict a

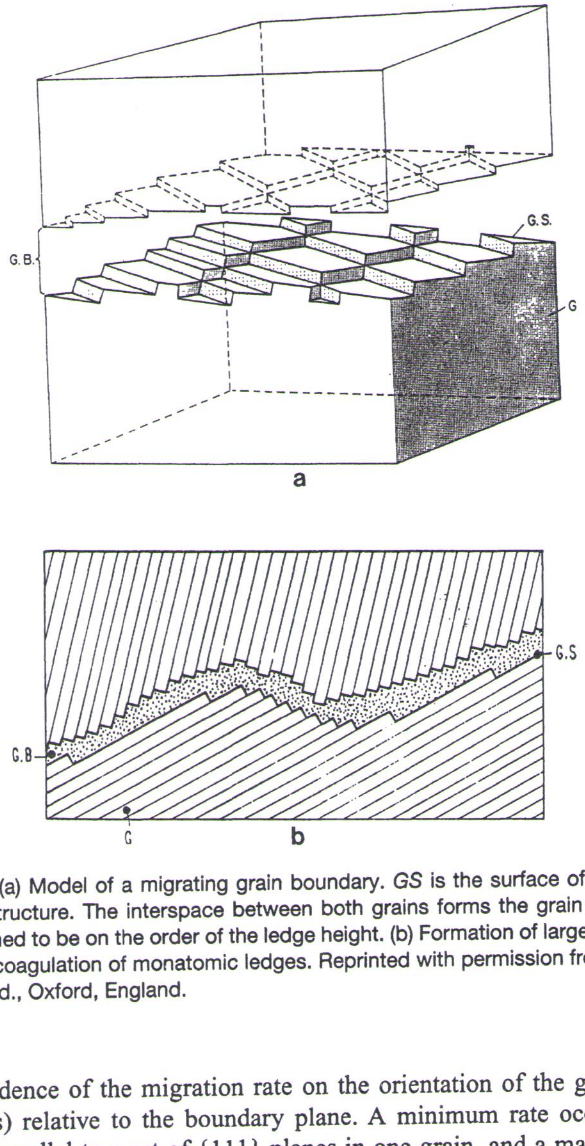

Figure 13.39. (a) Model of a migrating grain boundary. *GS* is the surface of both grains (*G*) with a ledge structure. The interspace between both grains forms the grain boundary (*GB*), which is assumed to be on the order of the ledge height. (b) Formation of large grain boundary ledges by the coagulation of monatomic ledges. Reprinted with permission from [83] by Elsevier Science Ltd., Oxford, England.

strong dependence of the migration rate on the orientation of the grains (i.e., the {111} planes) relative to the boundary plane. A minimum rate occurs when the boundary is parallel to a set of {111} planes in one grain, and a maximum occurs when the boundary is steeply inclined to {111} planes in both grains. The model also predicts an increase in migration rate with temperature from both a higher diffusivity and a higher kink density on the ledges. A number of experimental data showing that the grain boundary migration rate is orientation dependent are available [84,86–88], but so far none of these data have been correlated with the grain boundary structure and TLK model just described. Another possible mechanism of grain boundary motion is by the transformation of structural units at the boundary, but this mechanism has not been thoroughly developed.

13.2.8. Segr

The thermodyn
very similar to
grain boundari
(6.24) [89]. For
obeyed for the
denum over a
boundary segre
solute content i
Seah and
theory to write

where X_{gb} is th
X_B is the bulk n

Figure 13.40. Lar
measured by Aug

G

S

f both grains (G)
n boundary (GB),
e grain boundary
from [83] by Else-

grains (i.e., the
ccurs when the
aximum occurs
ins. The model
th a higher dif-
perimental data
ndent are avail-
 with the grain
 mechanism of
t the boundary,

13.2.8. Segregation to Grain Boundaries

The thermodynamics of equilibrium grain boundary segregation in binary alloys are very similar to those of surfaces discussed in Chapter 6. Prediction of segregation to grain boundaries can be described using the Langmuir–McLean relation in Eq. (6.24) [89]. For example, Figure 13.40 shows that the Langmuir–McLean relation is obeyed for the segregation of 8 to 12 ppm of oxygen to grain boundaries in molybdenum over a wide temperature range. The basic features of equilibrium grain boundary segregation are evident in this plot (i.e., segregation increases as the bulk solute content increases and as the temperature decreases).

Seah and Hondros [90] have used a solid-state analogue of gas adsorption theory to write a predictive equation for segregation to grain boundaries,

$$\frac{X_{gb}}{1-X_{gb}} = \frac{X_B}{X_B^{\text{sat}}} \exp \frac{-\Delta G'}{RT}, \tag{13.40}$$

where X_{gb} is the fraction of the grain boundary monolayer covered with segregant, X_B is the bulk mole fraction of solute B, $X_B{}^{\text{sat}}$ is the bulk solid solubility and

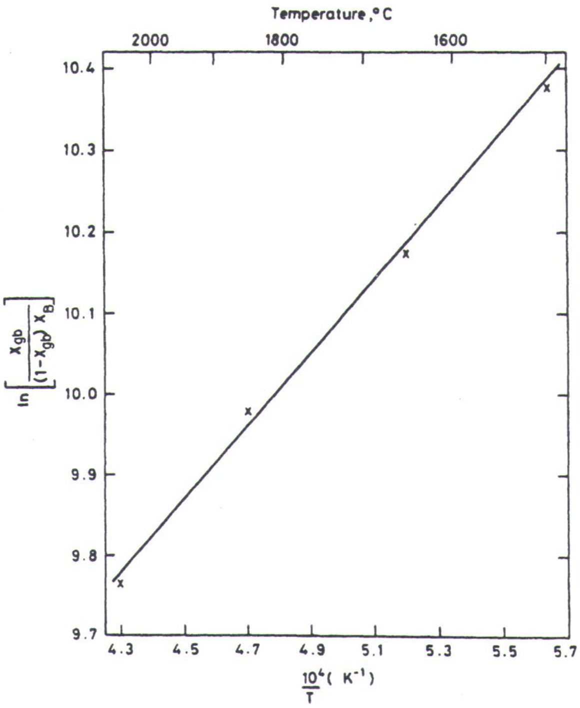

Figure 13.40. Langmuir-McLean plot for oxygen grain boundary segregation in molybdenum measured by Auger electron spectroscopy. From [89].

$$\Delta G' = \Delta G_{\text{gb}} - \Delta G_B, \tag{13.41}$$

where ΔG_{gb} is the free energy for grain boundary segregation and ΔG_B is the free energy of solution of the alloying element in the bulk. Thus, $\Delta G'$ represents the free energy difference between solute that is in solution in the alloy versus solute that is segregated to the grain boundary. There is a tendency for segregation when $\Delta G_{\text{gb}} > \Delta G_B$, so that $\Delta G'$ is negative. As with surfaces, it is useful to define a parameter called the grain boundary enrichment ratio β_{gb}, which represents the ratio X_{gb}/X_B in the dilute limit. For grain boundaries, this quantity is given as

$$\beta_{\text{gb}} = \frac{1}{X_B^{\text{sat}}} \exp \frac{-\Delta G'}{RT}. \tag{13.42}$$

A plot of β_{gb} versus the atomic solid solubility X_B^{sat} is shown in Figure 13.41 for a number of experimental data at various temperatures. As for the case of surfaces

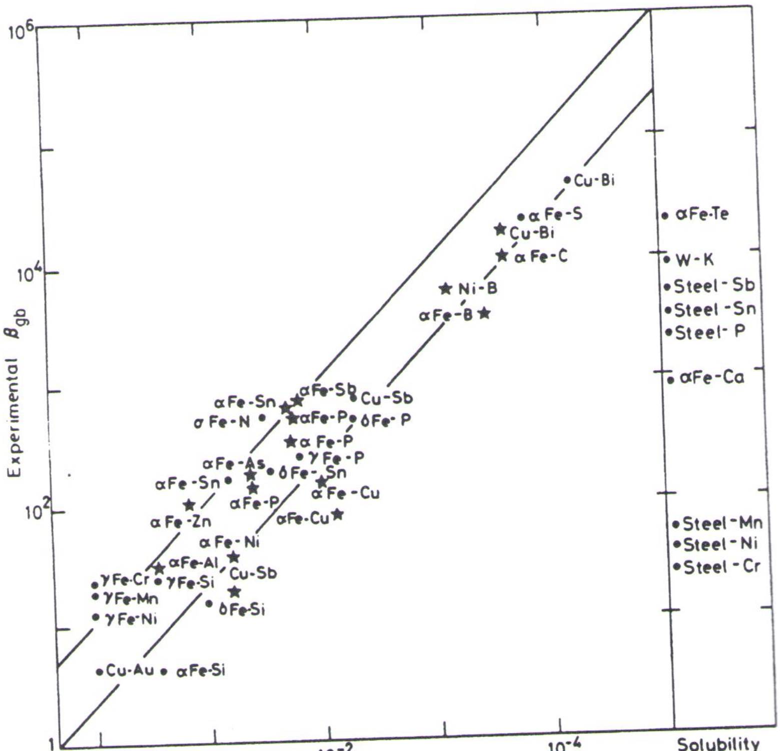

Figure 13.41. Correlation of measured grain-boundary enrichment ratios with the atomic solid solubility. From [89,90].

(13.41)

ınd ΔG_B is the free
represents the free
ersus solute that is
ation when $\Delta G_{gb} >$
define a parameter
the ratio X_{gb}/X_B in

(13.42)

Figure 13.41 for a
ıe case of surfaces

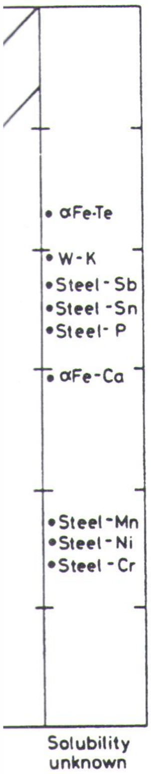

s with the atomic sol-

---

shown in Figure 6.10, there is good overall agreement between the grain boundary enrichment ratio and the solid solubility, so that the grain boundary enrichment for systems in which experimental data are not available can be estimated from the solvus line in the corresponding binary phase diagram and Figure 13.41.

Based on the data in Figure 13.41, it was determined that, although ΔG_B values typically range from zero to –80 kJ/mol, $\Delta G'$ has a mean value of -10 ± 6 kJ/mol, so that

$$\Delta G_{gb} = \Delta G_B - (10 \pm 6)\ \text{kJ/mol}. \tag{13.43}$$

This treatment is valid only when the bulk molar solute fraction is less than the solid solubility. If excess solute content is also present so that a second phase appears, the solute content is limited to the solid solubility. The situation becomes more complicated in ternary and higher order alloys; these are discussed elsewhere [89, 91].

Although the same physical phenomena that are included in the derivations of Eqs. (6.25) and (6.26) for surfaces could be used to develop expressions for the quantity ΔG_{gb} in grain boundary segregation, the problem is much more complicated because of the variety of grain boundary structures that are possible as a function of the five macroscopic and three microscopic degrees of freedom of a boundary (Eqs. 13.6 and 13.9). There are a number of experimental data which demonstrate that segregation to grain boundaries is orientation dependent (Fig. 13.42, for example) and indicate that high-angle boundaries may exhibit more segregation than low-angle or special grain boundaries, but these relationships are only qualitative and not fully understood [92,93]. As a result, there is no quantitative model for grain boundary segregation that can account for the role of boundary structure and solute properties on segregation. Recent atomistic simulations have been quite useful in elucidating some of the factors involved in grain boundary segregation; these are discussed further.

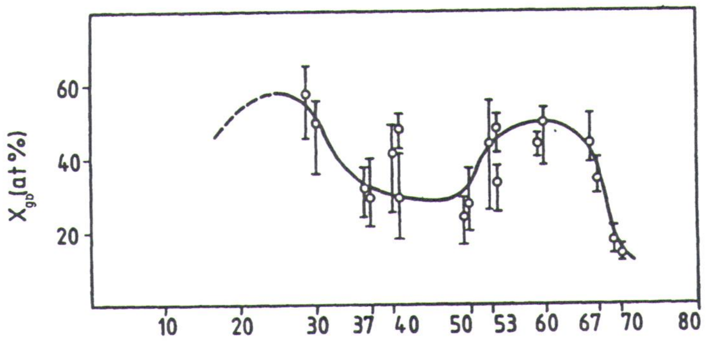

Figure 13.42. Grain boundary segregation of bismuth in copper as a function of tilt angle for copper <100> tilt bicrystals determined by Auger electron spectroscopy. From [92,93].

In general, alloys that display surface segregation also display grain boundary segregation, but often to a lesser extent. This is illustrated for the case of tin in iron in Figure 13.43. This behavior can be rationalized by remembering that a grain boundary generally contains more free volume and some number of broken bonds (refer to Figs. 13.32 and 13.33) just like a free surface, although to a lesser extent than a surface. By analogy with surfaces, it seems reasonable to expect that the equilibrium partition ratio k_e (Eq. 6.27) might be a good indicator of grain boundary segregation, particularly given the similarity of the bonding environments in grain boundary structural units and the polyhedral units in a DRP liquid, but this relationship has not been tested.

Qualitatively, it has been argued that once a segregating atom reaches a grain boundary, it remains there because of the favorable bonding environment provided by the boundary [95]. In many systems, the segregating element is a nonmetal,

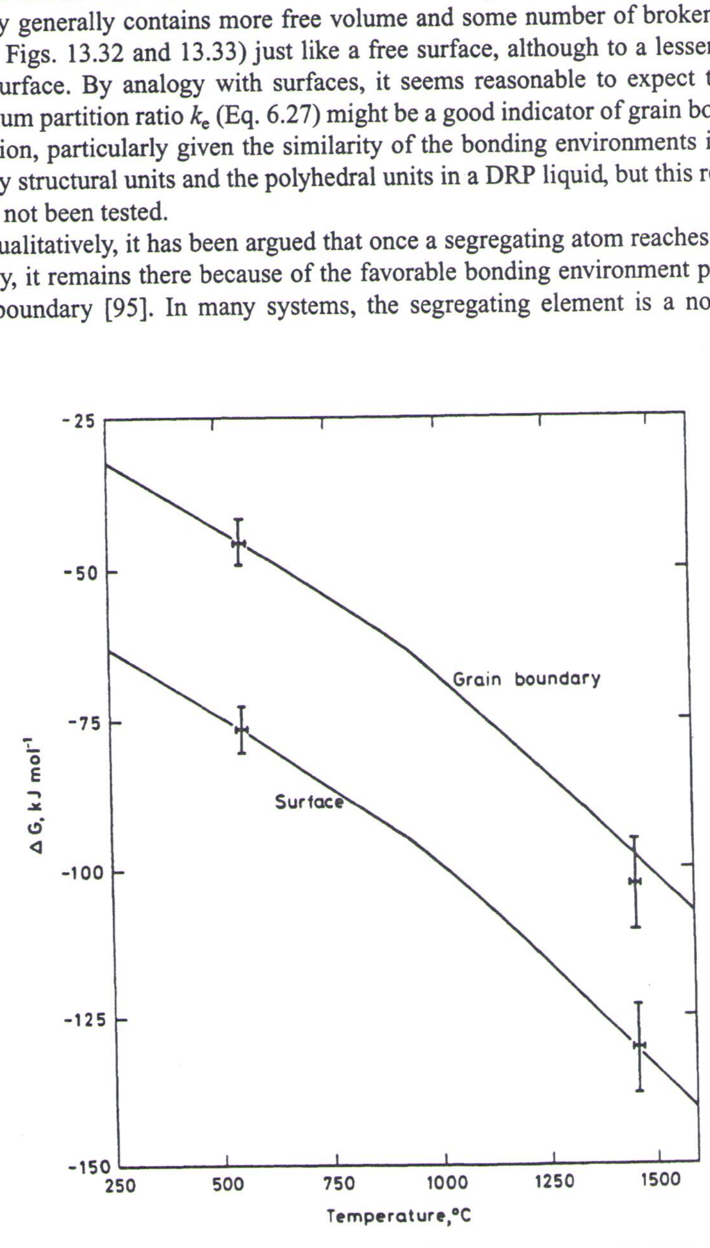

Figure 13.43. Predicted temperature dependence of the free energies of surface and grain boundary segregation of tin in iron as a function of temperature, with experimental data at 550°C and 1420°C. From [89,94] copyright Taylor & Francis Ltd.

y grain boundary
:ase of tin in iron
ring that a grain
of broken bonds
to a lesser extent
› expect that the
f grain boundary
›nments in grain
but this relation-

ı reaches a grain
›nment provided
t is a nonmetal,

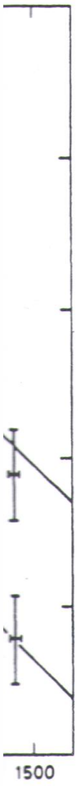

surface and grain
›erimental data at

which tends to form stoichiometric compounds with the metal. The structural units that make up such compounds often bear a close resemblance to the structural units that are commonly found in grain boundaries (Figs. 13.27 and 13.28). Hence, a segregating species may find an atomic geometry at the grain boundary that is much more compatible with the type of bonding environment that it would prefer to form with the metal and this causes it to stay in the boundary. The boundary would then be decorated with such segregated units. Some evidence for this explanation comes from atomistic calculations of grain boundary segregation, which clearly indicate site selectivity of the segregating species. For example, Sutton and Vitek [95] studied the segregation behavior of bismuth (a strong segregant and embrittler) and of silver (a weak segregant) in copper and gold to symmetric $\Sigma = 5$ (210) and $\Sigma = 17$ (530)/[001] tilt boundaries (refer to Fig. 13.27) by atomistic calculation. The energies of segregation of the elements to various sites in the boundary were found to vary widely, as illustrated in Figure 13.44. For a given structural unit, the segregation energy also varied considerably with its surroundings in the boundary (i.e., the boundary type). The large bismuth atoms generally went into those sites that were surrounded by a tensile stress field in the unsegregated boundary. In terms of a hard-sphere model, it segregated to the most spacious site. Segregation of bismuth to copper was also accompanied by an expansion perpendicular to the boundary, which can be interpreted as a weakening of the boundary cohesion.

Several recent Monte Carlo calculations of segregation to pure <100> twist boundaries in nickel–copper and platinum–gold alloys using EAM potentials have revealed a detailed picture of segregation in these alloys [96–98]. Pure twist grain boundaries are particularly convenient to study because the grain boundary contains an array of identical screw dislocations as a function of tilt angle up to ap-

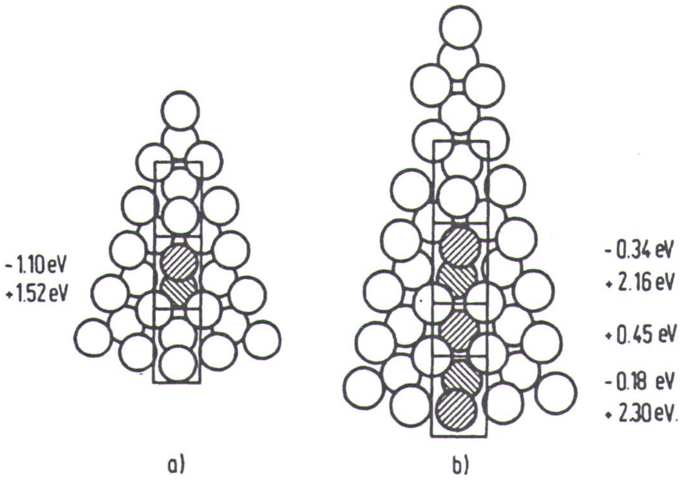

Figure 13.44. Segregation enthalpies (in eV/atom) for bismuth atoms in copper tilt boundaries when (a) $\Sigma = 5$ and (b) $\Sigma = 17$. From [45,95].

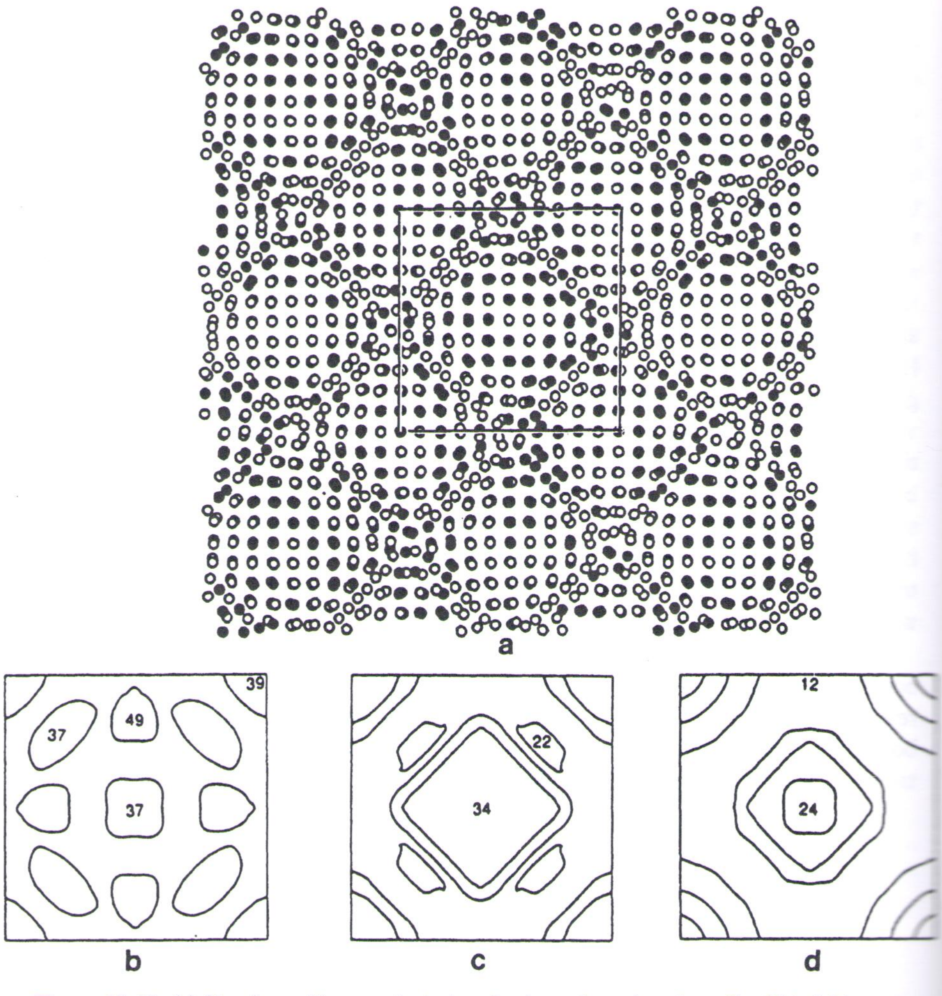

Figure 13.45. (a) Atomic positions projected on the boundary plane for a $\Sigma = 61$ twist boundary in a nickel-10 at.% copper alloy. The first two atomic layers on either side of the boundary are shown. The open circles are nickel atoms and the filled circles are copper. The screw dislocation network is located in the regions of poor matching between the crystals (compare with Figure 13.10). (b-d) Contour plots of the copper concentration as a function of position in the plane of the first (b), second (c) and third (d) atomic layers of the boundary. The plots correspond to the central unit cell outlined in (a). The numbers indicate the compositions at extremums in at.% copper and the contour spacing is 4.4 at.%. From [98].

---

proximately 35°
centrations of the
angle until satura
This behavior wa
aries rather than t
provides a simple
addition, the segr
either side of the
cations, as illustra
segregant also inc
increasing temper
tional interesting f
solute was highest
reverse trend was
(Table 2.1) indicat
to the boundary. I
the dislocation co
and shear stresses
per alloy, a volum
matching in tensio
er copper atoms to
lustrated in Figure
planes away from t
the corners, betwee
tance of the elastic
boundary structure
behavior of the ele
gation behavior of
there may be a dir
broken bonds at twi
tionship has not bee
the segregation beh
surface segregation

PROBLEMS

13.1. Suppose the g
grain boundar
(13.1) be used
not?

13.2. Thin sheets of
form thermal g

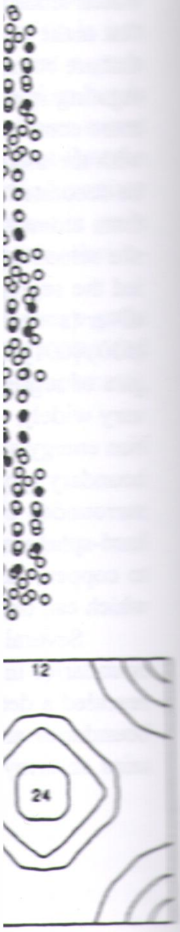

d

31 twist bound-
of the boundary
The screw dis-
stals (compare
on of position in
. The plots cor-
positions at ex-

proximately 35° (e.g., refer to Figs. 13.10 and 13.12). In these studies, the concentrations of the segregating species were found to increase linearly with twist angle until saturation occurred at the boundaries at relatively high angles (~ 35°). This behavior was related directly to the dislocation density in the twist boundaries rather than to the particular value of Σ. It is a significant finding because it provides a simple explanation for the segregation behavior of twist boundaries. In addition, the segregating species were found to lie within two or three planes on either side of the interfaces and to depend on the strain fields of the screw dislocations, as illustrated for the nickel–copper system in Figure 13.45. The amount of segregant also increased in proportion to $\Delta G'$ in Eq. (13.41) and decreased with increasing temperature in the studies, as expected from thermodynamics. An additional interesting feature in these studies, was that, in the platinum–gold alloy, the solute was highest in the dislocation cores, whereas in the nickel–copper alloy, the reverse trend was found. In both alloy systems, the positive heats of solution (Table 2.1) indicate a tendency for the elements to separate and thus, to segregate to the boundary. In the platinum–gold alloy, it was found that gold segregated to the dislocation cores, where the atoms could relieve the high hydrostatic tensile and shear stresses associated with the dislocations. In contrast, in the nickel–copper alloy, a volume expansion at the boundary (ΔV_i) left the regions of good matching in tension, which could be relieved by segregation of the elastically softer copper atoms to these regions in between the dislocation cores. This effect is illustrated in Figure 13.45, where the copper concentration in the second and third planes away from the boundary (Figs. 13.45c and d) is highest in the center and at the corners, between the screw dislocation cores. These results point to the importance of the elastic properties of the solute and its interaction with the local grain boundary structure in determining segregation behavior, as well as to the mixing behavior of the elements. Comparison of Figures 13.32 and 13.33 with the segregation behavior of the platinum–gold and nickel–copper alloys also indicates that there may be a direct correlation between the volume expansion and number of broken bonds at twist grain boundaries and the amount of segregant, but this relationship has not been examined. Clearly, more work needs to be done to quantify the segregation behavior of grain boundaries, although the same basic trends as in surface segregation are evident.

PROBLEMS

13.1. Suppose the grains shown in Figure 13.1 were two different phases and the grain boundary was thus an interphase boundary. Could an equation like Eq. (13.1) be used to determine the interphase boundary energy? Why or why not?

13.2. Thin sheets of pure copper and gold are heated separately in a vacuum to form thermal grooves where the grain boundaries intersect the surface. Calculate the average groove angle formed at 1000°C. Describe how you could experimentally determine whether your calculated value would be valid based on the equilibrium of the grain boundaries.

13.3. The figure below (from [99]) shows a series of grain boundaries intersecting the surface of a thin wire of silver–40 at.% aluminum alloy, similar to the geometry shown in Figure 13.1.

(a) Measure the dihedral angles for the three boundaries indicated by arrows.

(b) What is the ratio γ_{gb}/γ^{SV} for this alloy?

(c) Determine γ_{gb} when $\gamma^{SV} = 2190$ mJ/m^2 at 748 K.

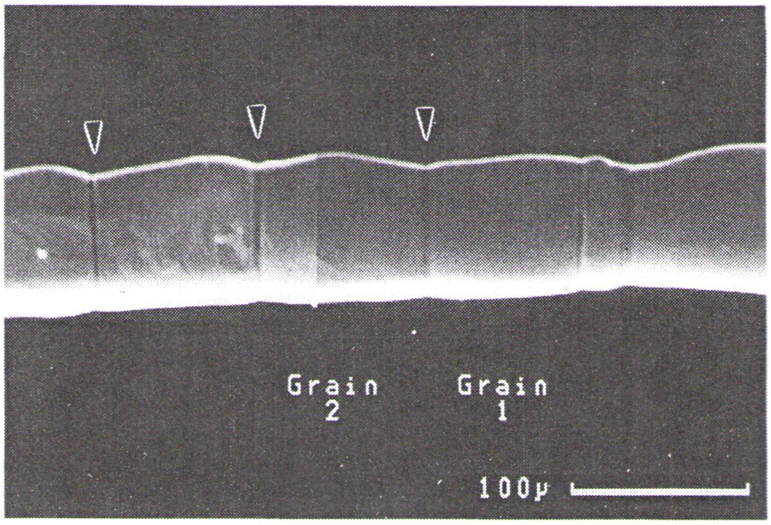

13.4. For a given value of θ, which has a lower energy: a grain boundary having many dislocations with small Burgers vectors or one having fewer dislocations with larger Burgers vectors?

13.5. Consider two parallel grain boundaries similar to Figure 13.3, where one grain has $\theta = \theta_1$ and the other has $\theta = \theta_2$. Show that the two boundaries can reduce their energy by combining to form a single boundary with $\theta = \theta_1 + \theta_2$.

13.6. Consider a grain boundary in an f.c.c. crystal where the plane of the boundary is (110) and the two grains have a small relative rotation θ about the $[1\bar{1}2]$ axis, which is common to the two grains. Show that the grain boundary is a vertical row of extended edge dislocations.

13.7. Two f.c.c. crystals with a lattice parameter $a = 0.4$ nm are rotated 0.5° about $[11\bar{2}]$. If the boundary is a symmetrical tilt boundary made up of edge dislocations:

(a) What is the boundary plane?

how you could
l be valid based

ies intersecting
similar to the

ated by arrows.

ndary having
wer disloca-

, where one
aries can re-
$= \theta_1 + \theta_2$.

he boundary
ut the $[1\bar{1}2]$
oundary is a

l 0.5° about
edge dislo-

(b) What is the length of dislocation line per unit area of the boundary?

(c) Calculate the angle at which the individual dislocations making up the boundary become indistinguishable.

(d) Show that these dislocations are stable with respect to displacement of any one of them on its slip plane.

13.8. A simple cubic crystal contains a cube-shaped volume of material that has a small difference in orientation from the surrounding crystal. The disoriented cube has faces parallel to {100} planes and is rotated (relative to the rest of the crystal) about the (001) axis. Draw the distribution of dislocations on the faces of the cube.

13.9. Figure 13.10 shows a relaxed pure twist boundary in a simple cubic crystal.

(a) What is the angle of misorientation θ?

(b) Sketch the O-lattice vectors $\mathbf{x}_1^{(O)}$ and $\mathbf{x}_2^{(O)}$ on the figure.

(c) Find the components of the two O-lattice vectors $\mathbf{x}_1^{(O)}$ and $\mathbf{x}_2^{(O)}$ if $\mathbf{b}_1 = [1,0,0]$, $\mathbf{b}_2 = [0,1,0]$ and the rotation axis is [001]. Use the rotation angle calculated in part (a).

13.10. We can write Frank's formula for a rotation θ about [001] as

$$
\begin{aligned}
b_1 &= -\theta x_2 \\
b_2 &= \theta x_1 \\
b_3 &= 0,
\end{aligned}
$$

where $\mathbf{b}$ (b_1, b_2, b_3) represents the discrete points of the dislocation network. Show that this equation is identical to Eq. (13.22) for small θ.

13.11. Derive $\mathbf{N}_1$ for a simple tilt boundary consisting of one set of edge dislocations.

13.12. Determine $\mathbf{N}_1$ and $\mathbf{N}_2$ for a simple twist boundary consisting of two sets of orthogonal screw dislocations.

13.13. (a) On the same graph plot (i) the grain boundary energy γ_{gb} for a pure tilt {100} boundary (Eq. 13.3) and (ii) twice the surface energy $\gamma^{SV}_{\{100\}}$ (Eq. 3.18), as a function of θ from 0° to 10° for pure gold.

(b) Explain any differences in the shapes and magnitudes of the two curves in terms of atomic bonding at the interfaces.

13.14. Specify the grain boundary in Figure 12.2 using the five DOF as in Eq. (13.5) and according to the interface-plane scheme in Eq. (13.6).

13.15. The drawing below shows a $[1\bar{1}0]$ projection of a coherent twin boundary in a face-centered cubic crystal.

(a) Draw in the coincident site lattice (CSL).

(b) What is the value of Σ for this boundary?

(c) Draw in the DSC lattice.

(d) What are the two shortest DSC lattice vectors?

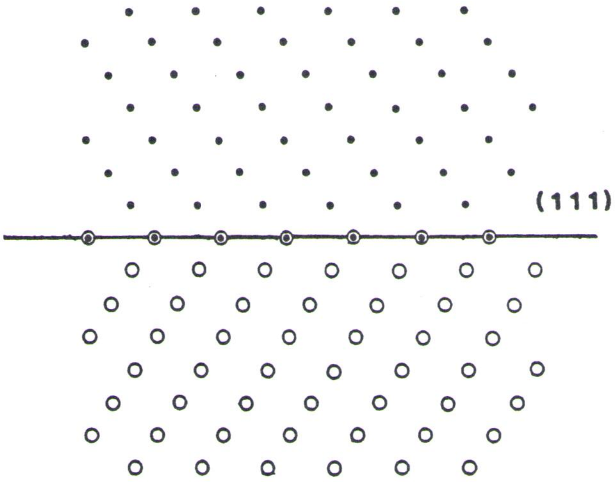

13.16. A twin boundary in the f.c.c. structure is shown in the four illustrations on the next page (from [52]). Figure (a) shows a planar boundary, whereas linear defects are present at the boundaries in (b) through (d). The CSL/DSC lattices are indicated in each figure and refer to Frank circuits, which can be used to determine the ledge and dislocation character of the linear defects at the interface, as shown in the figures. The start and finish points of the circuits are indicated by S and F, respectively. Use these diagrams to determine whether the ledges in (b) through (d) have pure ledge or Burgers vector character. Specify the associated ledge or Burgers vectors in each case.

13.17. (a) Make a sketch similar to Figure 13.34 showing an extrinsic stacking fault in a metal or alloy.

(b) If this alloy forms an ordered $L1_2$ structure like Cu_3Au, make a sketch of the f.c.c. unit cell and show a schematic of the extrinsic stacking fault in this alloy. How does it compare with that in part (a)?

(c) Suppose instead the alloy forms an $L1_0$ ordered structure like CuAu–I. Make a sketch of the f.c.c. unit cell and show a schematic of the extrinsic stacking fault in this alloy. How does it compare with those in parts (a) and (b)?

13.18. (a) Calculate the stacking fault energy of pure gold at room temperature (20°C) from measured values of the twin boundary energy.

(b) Plot schematically the stacking fault energy of gold as a function of copper concentration in a dilute gold–copper alloy and explain the basis of your plot.

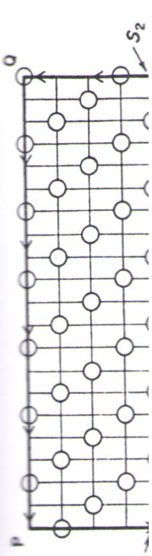

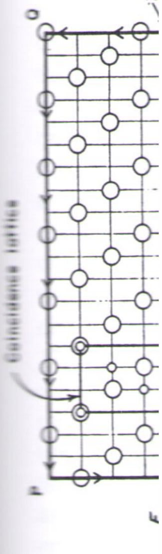

: illustrations on
ary, whereas lin-
. The CSL/DSC
ts, which can be
linear defects at
points of the cir-
ms to determine
Burgers vector
each case.

trinsic stacking

, make a sketch
ic stacking fault

re like CuAu–I.
ic of the extrin-
h those in parts

om temperature
gy.
function of cop-
ain the basis of

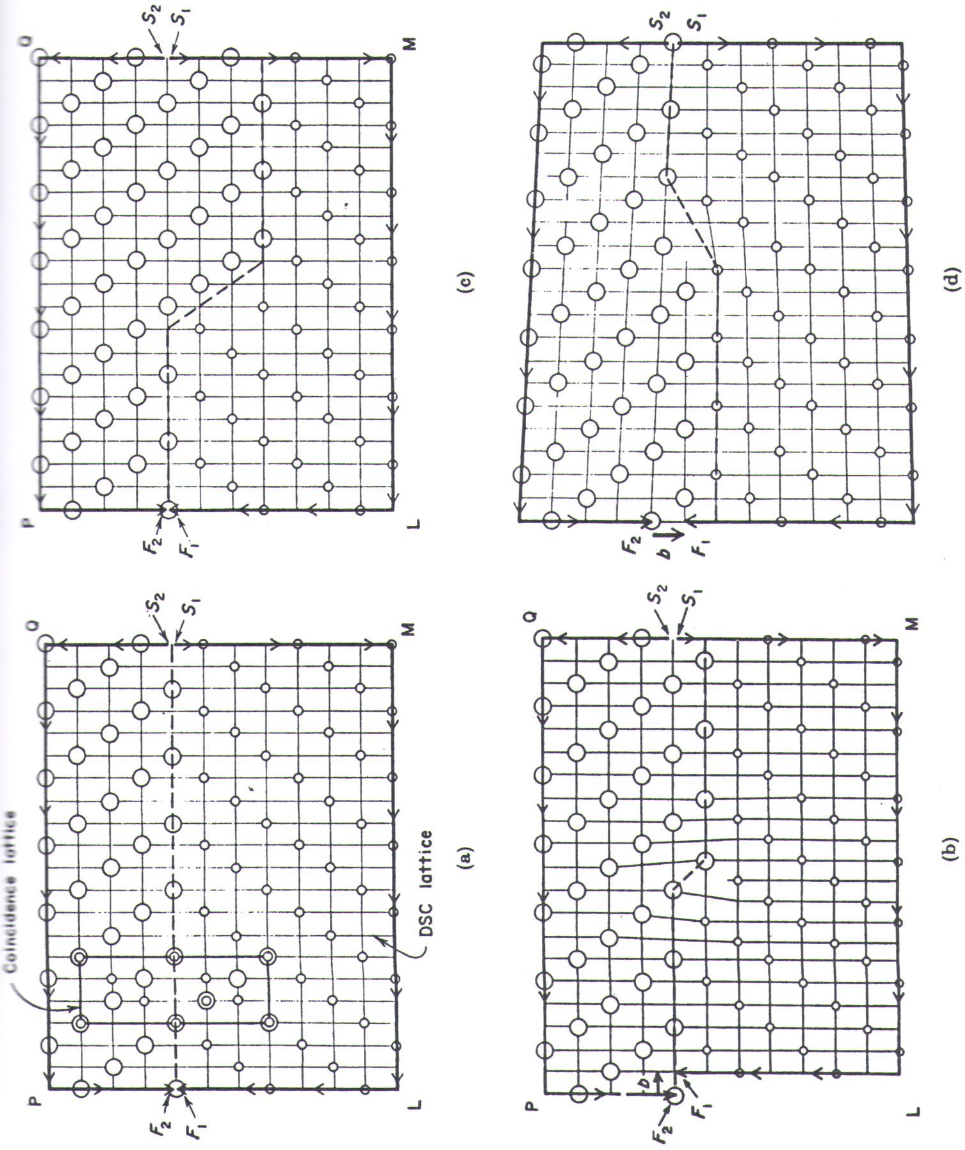

13.19. Calculate the fault energies in Eqs. (13.35)–(13.38) for copper and silver assuming that $\phi_2 = 0.25\phi_1$, $\phi_3 = 0.05\phi_1$, $\phi_4 = 0.01\phi_1$ and $\phi_5 = 0.002\phi_1$. Compare your results with the values for γ_{isf} in Table 13.3.

13.20. The grain boundary enrichment ratio $\beta_{gb} = X_{gb}/X_B$ for sulfur in α-iron has been measured as 7,170 at 700°C and 15,700 at 550°C. Use these data to estimate the binding energy between a sulfur atom and an α-iron grain boundary. Express your answer in both kJ/mol and eV/atom.

13.21. Suppose the $\Sigma = 37$ grain boundary in Figure 13.27 is copper and that a small amount of bismuth is segregated to the boundary. What positions will the bismuth atoms occupy? Why?

13.22. Based on the data below (from [91]) for the amount of phosphorus segregation to grain boundaries in iron versus temperature and composition, calculate ΔG_{gb} using Eq. (13.43).